NONDESTRUCTIVE TESTING AND MATERIAL CHARACTERIZATION BY TERAHERTZ PULSED IMAGING AND TIME-DOMAIN SPECTROSCOPY

A dissertation
To be presented to
The Academic Faculty

By

Min Zhai

In Partial Fulfillment
of the Requirements for the Degree
Doctor of Philosophy in
Electrical and Computer Engineering

Georgia Institute of Technology

May 2022

NONDESTRUCTIVE TESTING AND MATERIAL CHARACTERIZATION BY TERAHERTZ PULSED IMAGING AND TIME-DOMAIN SPECTROSCOPY

Approved by:

Dr. David S. Citrin, Advisor
School of Electrical and Computer Engineering
Georgia Institute of Technology

Dr. Alexandre Locquet
School of Electrical and Computer Engineering
Georgia Institute of Technology

Dr. Nico F. Declercq
Woodruff School of Mechanical Engineering
Georgia Institute of Technology

Dr. Paul L. Voss
School of Electrical and Computer Engineering
Georgia Institute of Technology

Dr. Waymond R Scott
School of Electrical and Computer Engineering
Georgia Institute of Technology

ACKNOWLEDGEMENTS

I appreciated all people who helped me during my Ph.D. I cannot acknowledge them allowing for the limited space here.

First of all, I would like to express my most sincere gratitude to my Ph.D. supervisor Prof. David. S. Citrin and Prof. Alexandre Locquet. I appreciate your wisdom and guidance during this work. As excellent advisors, you not only taught me a lot about terahertz science and technology but also left an indelible and influential mark on my scientific career. Studying at the Georgia Institute of Technology has been an invaluable treasure in my whole life. Without your encouragement and support, it would have been impossible for me to complete my Ph.D. smoothly.

I want to express my deep gratitude to Prof. Nico F. Declercq for his guidance associated with ultrasonic imaging. Due to the absence of ultrasonic background, it was hard for me to compare terahertz and ultrasonic imaging comprehensively. His responsibility and patience helped me go through that tough time.

I want to express my gratitude to my dissertation reading committee members: Prof. Paul L. Voss, for organizing my proposal, even during that difficult period, and Prof. Waymond R Scott for providing valuable and insightful comments on my written dissertation.

I want to thank Cyrielle Roquelet, Patrice Alexandre, and Laurence Daheron from ArcelorMittal Maizières Research for providing financial assistance to explore practical applications of terahertz technology in steel industries. I thank Prof. Mi Jung from Konkuk university's glocal campus and Prof. Deokha Woo from the Korea institute of science and technology for fabricating nanoporous Al_2O_3 films and conducting structural characterization using Field Emission Scanning Electron Microscopy (FE-SEM). I thank Dr. Esam T. Ahmed Mohamed for performing acoustic scanning experiments on injection-molded thermoplastics for achieving comparative studies with terahertz results. I thank G. Schneider, R. Kalmar, and M. Fendler from CEA tech for sharing the material properties of injection

molded thermoplastics, which provided me with a better understanding of the formation mechanism of weld lines.

I would also like to thank all my dearest friends at Georgia Tech, such as Dr. Junliang Dong, Dr. Xiaolong Wu, Dr. Georges Chahine, Dr. Jaume Calvo-de la Rosa, and Mr. Md Shariful Islam, for offering various support. Last but not least, I would also like to thank my parents for their unconditional support and encouragement during my Ph.D.

TABLE OF CONTENTS

LIST OF TABLES

LIST OF FIGURES

LIST OF FIGURES

SUMMARY

The terahertz (THz) portion of the electromagnetic spectrum—by convention ranging over the frequency range $\nu \in$ [100 GHz, 10 THz]—has attracted considerable interest among academic and industrial fields owing to the nature of THz waves. Compared to x-rays, infrared, and visible light, THz radiations can penetrate deep and allow for non-ionizing in deep three-dimensional (3D) imaging. The goal of this thesis aims at exploring the potential of THz imaging and time-domain spectroscopy (TDS) in the in-line monitoring of the quality of steel products within steel industries in a non-destructive and contactless manner, stratigraphic characterization of materials including both micron-scale and millimeter-scale layers, and material characterization that is opaque to near-infrared light.

The thesis is outlined as follows.

Chapter 1 introduces the background of this thesis. The basic knowledge of THz electromagnetic waves and the motivation of this thesis are included. Moreover, recent advances in applying THz-based technology in industries and academia are also summarized.

Chapter 2 presents a detailed description of the THz TDS system utilized in this work.

Chapter 3 focuses on discussing the potential of THz-based technology in the thickness measurement and uniformity characterization of optically thin layers in the steel industry. Owing to the optically thin thickness of mill scale films on steel coupons, three advanced signal processing algorithms, frequency-wavelet domain deconvolution (FWDD), sparse deconvolution (SD), and autoregressive spectral extrapolation (AR), are employed to beat the limitation of THz wavelengths and enhance the resolution in depth. The performance of all deconvolution algorithms is compared systematically. Moreover, an AR algorithm based on the modified covariance method is proposed for uniformity characterization of the individual layers in a multilayer coating on steel. Numerical simulations are made to highlight the merit of the proposed algorithms over conventional AR algorithms based on Burg's method. Comparative studies with Eddy-current measurements are also involved in

the study to validate the accuracy of THz results.

Chapter 4 addresses the stratigraphic characterization of materials with complex layered structures. Three case studies are discussed in this chapter. In the first case study, THz reflection and transmission experiments characterize polycarbonate (PC) and poly-methyl methacrylate (PMMA) sheets with thicknesses ranging from 2 mm to 12 mm. One dispersion model is utilized to simulate the phenomenon of pulse spreading resulting from the frequency-dependent refractive index observed in transmission results. Two signal processing techniques, FWDD and cross-correlation (CC), are employed for structural characterization and estimate the corresponding maximum resolvable thickness. The second case study presented here is the nondestructive stratigraphic analysis of structures containing both micron-scale *and* millimeter-scale layers, which is a conflicting demand. One second-order SD technique, incorporating a propagation model accounting for dispersion, is demonstrated for sparse structure representation. In the third case study, we explored the potential of THz techniques for various paper-handling tasks, especially on obtaining page count and locating foreign objects (*e.g.*, staples) in multipage legacy documents, which are prerequisites for subsequent paper-handling tasks, such as scanning. After obtaining the dielectric properties of paper stacks for $\nu \in$ [0.2 THz, 2 THz] in transmission measurements, the internal structure of paper stacks is presented based on TOFT. The page count and staple location within paper stacks are determined from THz reflection data. Finally, the exact position of stapled sheets buried in a paper stack is located by THz TOFT.

Chapter 5 studies the material properties using THz TDS. Three case studies are presented in this chapter. In the first case study, polarization-resolved THz TDS is utilized to nondestructively characterize the THz birefringence of nanoporous Al_2O_3 films on an Al substrate after a two-step electrochemical anodization process. THz scattering imaging is also employed to investigate the homogeneity of formed nanoporous Al_2O_3 films. In the second case study, the quality of one Acrylonitrile Butadiene Styrene (ABS) thermoplastic electrical receptacle is investigated through THz reflective imaging and scanning acous-

tic microscopy (SAM) in a nondestructive and noncontact manner. The associated THz electromagnetic, acousto-mechanical, and morphological features of weld lines, one common defect introduced during the injection molding process, are also studied. The third case study systematically characterized the optical and dielectric properties of three common thermoplastics over a broad frequency ν ranging from 0.5 to 2 THz. The frequency-dependent refractive index $n(\nu)$, attenuation coefficient $\alpha(\nu)$, complex permittivity $\delta(\nu)$, and loss tangent $\tan(\nu)$ of studied plastics are calculated and compared based on the corresponding transmitted signals. All investigated materials present a relatively low refractive index (compared with glass and many crystalline materials) and low dielectric loss.

Chapter 6 is divided into three sections. Firstly, the main conclusion and contribution are summarized based on the abovementioned results. Secondly, future perspectives and research directions are proposed. Thirdly, peer-reviewed publications and conferences attended during the Ph.D. study are listed.

CHAPTER 1

INTRODUCTION AND BACKGROUND

1.1 Motivation

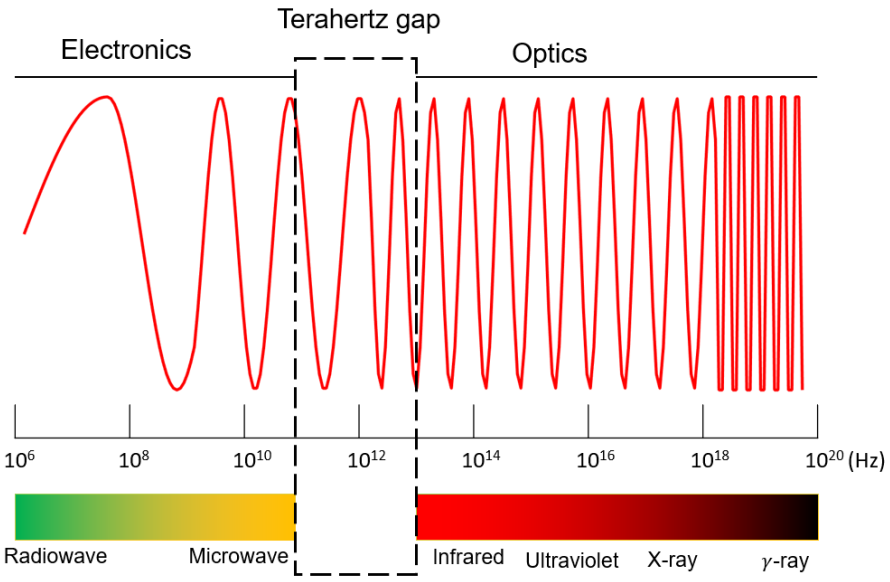

Figure 1.1: Artistic representation of the electromagnetic spectrum of THz waves.

The frequency range of terahertz (THz) electromagnetic waves, as shown in Fig. 1.1, typically refers to 100 GHz to 10 THz (1 THz corresponds to 300 μm in wavelength, 33.3 cm^{-1} in wavenumber, and 4.2 meV in energy), which lies at the border between the photonic and electronic ranges. THz waves can penetrate numerous electrically non-conductive materials that may be opaque in the range of visible and infrared light and relatively transparent to x-rays. Moreover, as nonionizing radiation due to low THz photon energy compared to high-frequency radiations such as ultraviolet and x-rays, THz waves present almost no known health risks to biological tissues [1]. For most of the 20th century, THz radiation was mainly utilized by astronomers, and some spectroscopists [2]. Owing to the rapid development of laser-based THz time-domain spectroscopy (TDS) between 1980s and 1990s,

the field of THz science and technology has expanded dramatically and now touches many areas from fundamental science to practical applications in the real world, such as quality control [3], cultural heritage [4], security [5], pharmaceutical sciences [6], nondestructive evaluation (NDE) [7], communication [8], as well as material characterization [9].

In the modern steel industry, non-destructive diagnostics for the thickness and quality measurements of coatings on steel are significant. The conventional commercial approaches are Eddy current measurement [10], x-ray imaging [11], and ultrasonic testing [12], infrared spectroscopy [13], and microwave measurements [14]. Although all these techniques mentioned meeting the demand in most daily cases and can achieve a precise measurement, some serious disadvantages limit their broad applications. The main disadvantage of infrared and microwave technology is the limited penetration depth and not good spatial resolution because of the relatively long wavelengths. For ultrasonic inspection, in certain materials, like austenitic steel, the large grain size found in welds can cause attenuation and mask internal defects. Therefore, a relatively smooth surface to couple transducer is demanded. Moreover, to avoid spurious indications, calibration should also be carried out before implementing ultrasound examinations. Eddy-current measurements require direct contact with the surface of investigated specimens and can only cover a limited number of sample points other than the entire surface. Therefore, Eddy-current measures are unsuitable for characterizing samples with large surface areas. More seriously, Eddy-current measurement lacks the capability of resolving individual layers on steel. Consequently, it fails to identify paint defects hidden below the surface. Although x-ray imaging possesses a strong penetration ability, it is mainly a laboratory tool because of the ionizing nature of x-rays. Therefore, alternative non-destructive, noncontact, and nonionizing approaches are highly demanded in the steel industry to monitor the quality of steel products.

After fabrication, the stratigraphic characterization of materials with complex structures is crucial for quality control. The most common approaches are optical measurements, scanning electron microscopy (SEM), and ultrasonic testings. As destructive ap-

proaches, the former two methods can only provide structural information along with the cross-section profile of investigated specimens. Therefore, they are not suitable for analyzing the structure of materials in a non-destructive manner. For ultrasonic testings, even though it is capable of mapping the entire sample, the waveform changes caused by the dispersion properties of guided ultrasonic waves and not good enough spatial resolution might inevitably contribute to the structural misinterpretation of investigated specimens. Therefore, alternative approaches capable of mapping the entire surface of samples and with relatively high resolution in depth are desired.

Studying the dielectric and optical properties of materials is also of great interest. Far infrared Fourier transform spectroscopy (FTS) in transmission and reflected mode is one of the most frequently used approaches for material characterization [15, 16]. However, because of the continuous wave (CW) noncoherent sources, FTS can only provide the absorption coefficient directly. Although the refractive index can be calculated through Kramers-Krönig relations [17], it presents some unexpected errors when the signal-to-noise ratio (SNR) of the transmitted field is not sufficiently high enough [18]. Moreover, because of the relatively low magnitude of CW sources employed in FTS, this technology seems unsuitable for characterizing materials with high absorption coefficients. Besides the material characterization of nonpolar amorphous materials, anisotropic materials are also worthy of study. To date, polarization-sensitive optical coherence tomography (OCT) is one of the most classical methods of studying anisotropic materials based on near-infrared (NIR) radiation [19, 20]. When the material is opaque to visible and NIR light, the anisotropic characterization using OCT becomes challenging. X-ray diffraction (XRD) can also be carried out for measuring the anisotropy of crystals as well as calculating the birefringence of the corresponding crystalline phase [21]. The utilization of ionizing radiations restricts its practical application broadly. Therefore, alternative approaches that can obtain the refractive index and absorption coefficient at one time, and investigate the birefringence of anisotropic materials in a contactless and non-destructive manner, are still needed for ma-

terial characterization.

THz-based technology, as a relatively novel and promising non-destructive evaluation (NDE) technique, has attracted considerable attenuation as a non-destructive, contactless, and nonionizing modality for material characterization and quality control of various non-metallic materials. Due to the relatively strong penetration of THz waves, THz-based technology can serve as a complementary method to other NDE techniques within the industry and academic fields. THz-based measurements can map the thickness distribution of coatings over a large area, and the information of individual layers estimated based on THz results is more accurate than ultrasound testing. Unlike the FTS, THz TDS typically uses coherent pulsed sources, and the optical properties of the investigated materials can be calculated directly based on the amplitude and phase of transmission signals. Moreover, THz TDS possesses a relatively high SNR compared to FTS. Therefore, THz TDS exhibits a better performance than existing material characterization techniques [9, 22].

The motivation of this thesis focuses on the thickness measurement and uniformity characterization of optically thin layers on steel, developing theories for stratigraphy characterization of complex structures containing both optically thin and thick layers, and studying the material properties at THz frequencies through THz TDS.

1.2 Literature survey

1.2.1 Terahertz characterization of coatings on metal

THz electromagnetic waves' unique properties have attracted vast attention and interest in real-time quality control in the automotive and steel industries. Imaging techniques using THz waves to acquire qualitative and quantitative information concerning the internal layer structure, or *stratigraphy*, of optically opaque, electrically insulating objects is the time-of-flight technique (TOFT). In principle, after generating a single-cycle THz pulse based on the nonlinear-optical or photoconductive conversion of femtosecond laser pulses, the generated THz signals subsequently interact with samples and are then detected using either

electro-optic or photo-conductive sampling. Due to the dielectric discontinuities in-depth, the reflected temporal THz echoes associated with the Fresnel coefficients between various interfaces are recorded as a function of transverse position in amplitude and time delay. The thickness of the individual layers is estimated based on the optical distance between two successive echoes and the dielectric properties of the corresponding layers within the THz range. A schematic diagram of the THz TOFT is shown in Fig. 1.2. When the thickness of each layer is optically thin in the THz regime (physical thickness divided by the refractive index less than half the minimum wavelength in the high SNR band), the temporal reflected THz echoes will overlap partially or even totally and thus be not visually distinct.

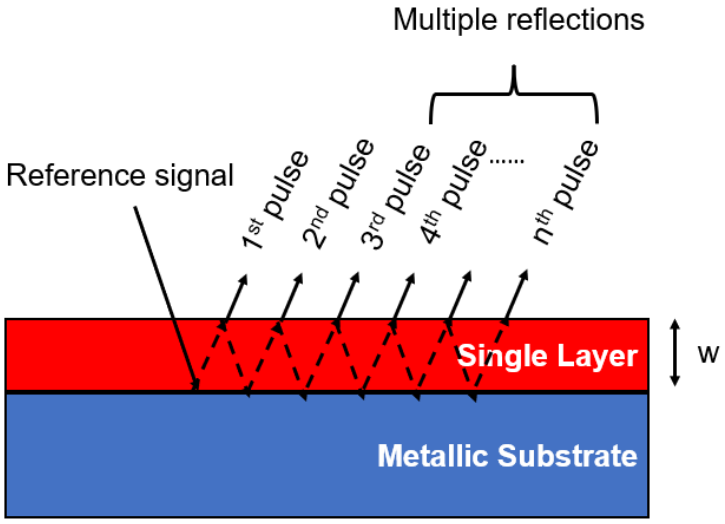

Figure 1.2: Schematic diagram representing multiple echoes used in THz TOFT.

To date, considerable efforts have been made to enhance the resolution of the minimum layer thickness. In Ref. [23], a 'paint meter' was proposed for noncontract two-dimensional mapping the painting thickness distribution of single- and multi-layered paint films; In Ref. [24], a numerical parameter fitting method based on multiple-regression analysis with the least-squares way was proposed, to enhance the axis resolution for a THz paint meter. In order to simplify the parameter fitting model, the dispersion, as well as multiple reflections, were not taken into consideration; In Ref. [25], a rigorous one-dimensional electromagnetic

model for THz propagation in a multi-layered medium combined with a numerical fitting method was demonstrated to extract the dielectric parameters and thickness information. The thickness of individual layers down to 18 μm is resolved and validated by other techniques; In Ref. [26], frequency-wavelet domain deconvolution (FWDD) by first employing frequency-domain filtering and then further improving the SNR by wavelet de-noising, was implemented to resolve the optically thin coating on steel. Based on numerical simulations, the minimum thickness of polycarbonate (PC) that FWDD can resolve is ~ 30 μm; In Ref. [27], an advanced regression procedure with a self-calibration model was proposed to measure individual automotive paint coatings in complex multi-layered structures. The actual industrial challenges, such as the effect of wet-on-wet spray in the painting process, are considered. The minimum thickness of an individual layer among a four-layer sample down to 4 μm, was resolved successfully; In Ref. [28], a sparse deconvolution based on an iterative shrinkage algorithm was proposed to characterize multi-layered structures. Sparse deconvolution with superresolution is developed further by an upsampling approach based on time interpolation to overcome the time resolution limited by the sampling period in the measurement and increase the precision of the estimation of echo arrival times; In Ref. [29], Hilbert transform (HT) along with post-transform signal spectral estimation was utilized to achieve a more accurate determination of the optical delay. Compared with simple peak-peak methods, the proposed HT-based approach seems to be easier to identify the peak position and is more robust against the waveform distortion caused by the dispersion and polarity reversal because of half-wave loss; In Ref. [30], one novel autoregressive spectral extrapolation based on the Burg method was designed to enhance the resolution in depth. Different from other mentioned approaches, it aims at recovering the missing frequency components in the low-SNR regions using the AR model based on the frequency components in the high-SNR regions. A single-layer polymer coating with a thickness of 22.5 μm on a steel substrate is resolved successfully; In Ref. [31], in order to reduce the incorrect thickness measurement due to dispersion, the propagation constants

extracted from the Helmholtz equation, other than the measured complex refractive index, was used to calculate the individual thickness of the multi-layered structure sample. Compared with the results measured with a digital micrometer, a good agreement is achieved; In Ref. [32], a hybrid principal component analysis (PCA)-particle swarm optimization (PSO)-extreme learning machine (ELM) model was proposed to measure the thickness of the oxide scales in the range of 0–15 μm. Compared with the classical back-propagation (BP) neural network model, which is time-consuming, inaccurate, and unstable, the proposed model presents an excellent oxide-scale prediction performance.

Except for thickness measurement, the THz-based technology is also available for non-destructive corrosion diagnosis of a metal surface covered with invisible insulators or painted films. In Ref. [26], the damage mechanism of steel products was investigated quantitatively and qualitatively using THz reflective imaging. Various failure modes, including corrosion, delamination, and blistering, have been identified successfully, and the delamination and blisters are related to adhesion failure. In Ref. [33], a compact THz imaging system diagnosed invisible corrosion of steel rods in concrete successfully. Moreover, the disconnection gap in insulated copper cable, optically thin epoxy resin on hot-dip galvanizing corrosion steel sheets, and ultrathin resin tape attached to forged banknotes, are also resolved successfully in THz reflection and transmission imaging.

Because the metallic surface roughness is a potential indicator of material degradation or damage, scattering effects resulting from surface non-uniformity have also been studied using THz imaging. In Ref. [34], six aluminum samples spanning a root mean square (RMS) roughness of 5-20 μm were accurately determined by analyzing THz reflectance spectra. The RMS roughness obtained by this method shows a good agreement with the RMS roughness obtained by a surface profilometer. Moreover, it also demonstrates that the proposed method can be used to resolve rough surfaces that differ in RMS roughness by approximately 1 μm. Therefore, the THz-based nondestructive evaluation system can identify and quantify material degradation in metallic surfaces and the feasibility of using

THz-based technology in industrial applications.

Due to the high sensitivity of THz waves to water content, waveform variation of THz time pulse echoes is an effective indicator to remotely monitor the wet to dry transformation process of a paint film. There has been a noticeable difference in spectroscopic characteristics in attenuation, delay, and distortion of the THz pulse echoes between dry and wet paint films. In Ref. [35], the wet-to-dry transformation of black acryl (BA) paint on an aluminum plate was monitored successfully based on the temporal change of the THz pulse-echo signal. Adequate parameters for the drying progress are extracted and serve as an indicator of the degree of drying in a thin paint film. Ref. [36] reported a method for the determination of the dry thickness of a dry coating probed in an arbitrary moment of the drying process using a practical medium approach. Therefore, THz-based technology can be applied directly in the paint shop to monitor the painting quality of vehicle bodies and other painted steel products.

1.2.2 Terahertz imaging in material characterization

Generally speaking, the studies of THz TDS fall into two distinctive categories. One category aims at identifying and classifying materials based on the unique features of their THz transmission spectra. In contrast, the other category focuses on studying the optical and dielectric properties of materials at THz frequencies.

For the former, several common explosives and related compounds (ERCs), such as 2,4,6-Trinitrotoluene (TNT), 2,4-Dinitrotoluene (DNT), Cyclotetramethylene-tetranitramine (HMX), and Nitroguanidine (NG), were investigated by THz TDS in the 0.1–2.8 THz region in Ref. [37]. The obtained absorption spectra show that most of the ERCs have THz fingerprints, which are caused by both the intramolecular and intermolecular vibrational modes of these materials; In Ref. [38], a range of natural and artificial textures were examined using THz TDS. Even though fabrics with similar appearance and texture, distinct THz transmission spectra for all investigated fabric materials indicate that THz

spectroscopy might have the potential for textile identification and fraud prevention; In Ref. [39], THz TDS was carried out for gastric cancer detection. It shows that cancer-affected regions present higher refractive indices and absorption coefficients than the adjacent healthy ones, reinforcing the feasibility of THz TDS for gastric cancer detection. It also demonstrates that the characteristic higher percentage of water in cancerous tissues is not the single factor contributing to the contrast of the observed refractive index and the absorption coefficient. In Ref. [40], microorganisms, such as moulds, yeasts, and bacteria, were identified successfully based on their intrinsic dielectric constants in the THz frequency range. The dielectric constant of the moulds was 1.24–1.85, which was lower than that of bacteria ranging from 2.75–4.11. The yeasts exhibited exceptionally high dielectric constants reaching 5.63–5.97. Cell wall composition is the leading cause of the observed differences in dielectric constants for different types of microorganisms.

Several machine learning-based algorithms have also been proposed and employed to classify the different frequency spectra accurately. In Ref. [41], a support vector machine (SVM) was used to identify THz absorption spectra of pure and impure illicit drugs (ketamine, methylephedrine, cocaine, ephedrine, pseudoephedrine, papaverine, and methamphetamine), and determine drug mixture contents. Compared with BP neural networks, SVM is appliable in many areas with fewer training samples, less training time, and quicker identification. In Ref. [42], the recognition of coals/rocks was achieved through a mathematical method of principal component analysis (PCA) and SVM. the recognition rate of coals/rocks reaches 100 %, and the recognition rate of different bituminous coals reaches 97.5 %. In Ref. [43], an SVM and deep neural networks (DNNs) were applied separately for classifying the frequency spectra of glucose and lactose. The classification accuracies achieved were 99% for the SVM method and 89.6% for the DNN method.

For the latter, the absorption spectra and the refractive index of several common glasses, lubricating oils, and polymers were measured, as presented in Ref. [9]. Relationships between the composition and the structure of the materials studied were correlated. In

Ref. [44], the absorption coefficient and refractive index of different building materials (plaster, glass, and wood) were determined using THz TDS in transmission geometry, and the reflection coefficient was calculated based on Fresnel's equations. Knowledge of these material parameters is critical to accurately model the propagation channel for future indoor THz communication systems. In Ref. [45], the dielectric constant and loss tangent of six commonly used low-loss polymers (polystyrene, perylene, polyimide, SLA resin, SU-8, and SUEX) were characterized using THz TDS in the 100 GHz to 2 THz frequency bands. These results provide valuable references and assessments for low-loss materials used in the micro-fabrication and packaging of devices for millimeter-wave (mmW) and THz applications.

As a well-known phenomenon at optical frequencies, birefringence can also be observed for various anisotropic materials in the THz frequency range. Unlike isotropic and nonpolar amorphous materials, anisotropic materials exhibit a polarization-dependent difference in optical and mechanical properties. When THz waves impinge the anisotropic material at an arbitrary angle concerning the optical axis, it will be split into two linearly polarized rays: the ordinary ray, which travels with the same velocity in every direction through the crystal, and the extraordinary ray, which travels with a velocity-dependent on the propagation direction. The birefringence Δn is determined according to

$$\Delta n = n_e - n_o \tag{1.1}$$

where n_o and n_e denote the refractive index along the extraordinary and ordinary axis of the anisotropic material, respectively. Depending on the birefringence Δn, the thickness d of the material, and the wavelength λ of THz waves, the phase shift $\Delta\phi$ between the ordinary and extraordinary THz waves can be calculated according to

$$\Delta\phi = \frac{2\pi}{\lambda} d\Delta n \tag{1.2}$$

For materials with the known optical axis orientation, the straightforward procedure to measure birefringence is from the time domain signals along the ordinary and extraordinary direction. When it comes to materials with an unknown optical axis orientation, the

situation becomes a little more complex. One frequency used approach for determining the optical axis is the measurement at different azimuthal angles by rotating the investigated sample. The extremes of the resulting time-domain curves as a function of the azimuthal angles allow identification of the orientation of the optical axis, and the difference between the maximum and minimum refractive indices corresponds to the absolute value of the birefringence. Ref. [46] presented the investigation of far-infrared properties of solid spruce wood using polarization-sensitive THz TDS. Both birefringence and diattenuation are found, which might attribute to preferential fiber orientation within the wood. Ref. [47] discussed the birefringence of Al_2O_3 and $LiNbO_3$ signal crystals with trigonal structure in the THz range of 0.25 THz to 1.4 THz. The corresponding measured birefringence of Al_2O_3 and $LiNbO_3$ at 1 THz is -0.32 and 1.78, respectively, which presents a good agreement with the results of *ab initio* calculations. In [48], the fibre direction of wood was predicted by the birefringence, which is obtained by rotating the wood sample against the THz wave polarization.

Birefringence and optical axis are significant parameters of anisotropic materials that provide information on the direction of anisotropy, such as the alignment of molecular chains or fibers or the direction of stress inside a material. Therefore, birefringence measurement by polarization-sensitive THz TDS could also serve as a promising tool for the reliability characterization of birefringent fibrous materials. In Ref. [49], THz TDS in reflection mode was used to detect the weld line defects in an injection-molded short glass fiber-reinforced composite. The correlation between the degradations of tensile strength and changes in the reflected THz waves caused by the weld lines is studied. The success of identifying and characterizing weld line defects demonstrates that THz imaging can evaluate the reliability of injection molded short glass fiber-reinforced composites.

1.2.3 Scope of the thesis

This thesis aims to discuss the potential of THz imaging and TDS for the nondestructive evaluation of material characterization in the field of steel industries and academia.

Chapter 1 introduces the background of this thesis. The basic knowledge of THz electromagnetic waves and the motivation of this thesis are included. Moreover, recent advances in applying THz-based technology in industries and academia are also summarized.

Chapter 2 presents a detailed description of the THz TDS system utilized in this work.

Chapter 3 focuses on discussing the potential of THz-based technology in the thickness measurement and uniformity characterization of optically thin layers in the steel industry. Owing to the optically thin thickness of mill scale films on steel coupons, three advanced signal processing algorithms, frequency-wavelet domain deconvolution (FWDD), sparse deconvolution (SD), and autoregressive spectral extrapolation (AR), are employed to beat the limitation of THz wavelengths and enhance the resolution in depth. The performance of all deconvolution algorithms is compared systematically. Moreover, an AR algorithm based on the modified covariance method is proposed for uniformity characterization of the individual layers in a multilayer coating on steel. Numerical simulations are made to highlight the merit of the proposed algorithms over conventional AR algorithms based on Burg's method. Comparative studies with Eddy-current measurements are also involved in the study to validate the accuracy of THz results.

Chapter 4 addresses the stratigraphic characterization of materials with complex layered structures. Three case studies are discussed in this chapter. In the first case study, THz reflection and transmission experiments characterize polycarbonate (PC) and poly-methyl methacrylate (PMMA) sheets with thicknesses ranging from 2 mm to 12 mm. One dispersion model is utilized to simulate the phenomenon of pulse spreading resulting from the frequency-dependent refractive index observed in transmission results. Two signal processing techniques, FWDD and cross-correlation (CC), are employed for structural characterization and estimate the corresponding maximum resolvable thickness. The second

case study presented here is the nondestructive stratigraphic analysis of structures containing both micron-scale *and* millimeter-scale layers, which is a conflicting demand. One second-order SD technique, incorporating a propagation model accounting for dispersion, is demonstrated for sparse structure representation. In the third case study, we explored the potential of THz techniques for various paper-handling tasks, especially on obtaining page count and locating foreign objects (*e.g.*, staples) in multipage legacy documents, which are prerequisites for subsequent paper-handling tasks, such as scanning. After obtaining the dielectric properties of paper stacks for $\nu \in$ [0.2 THz, 2 THz] in transmission measurements, the internal structure of paper stacks is presented based on TOFT. The page count and staple location within paper stacks are determined from THz reflection data. Finally, the exact position of stapled sheets buried in a paper stack is located by THz TOFT.

Chapter 5 studies the material properties using THz TDS. Three case studies are presented in this chapter. In the first case study, polarization-resolved THz TDS is utilized to nondestructively characterize the THz birefringence of nanoporous Al_2O_3 films on an Al substrate after a two-step electrochemical anodization process. THz scattering imaging is also employed to investigate the homogeneity of formed nanoporous Al_2O_3 films. In the second case study, the quality of one Acrylonitrile Butadiene Styrene (ABS) thermoplastic electrical receptacle is investigated through THz reflective imaging and scanning acoustic microscopy (SAM) in a nondestructive and noncontact manner. The associated THz electromagnetic, acousto-mechanical, and morphological features of weld lines, one common defect introduced during the injection molding process, are also studied. The third case study systematically characterized the optical and dielectric properties of three common thermoplastics over a broad frequency ν ranging from 0.5 to 2 THz. The frequency-dependent refractive index $n(\nu)$, attenuation coefficient $\alpha(\nu)$, complex permittivity $\delta(\nu)$, and loss tangent $\tan(\nu)$ of studied plastics are calculated and compared based on the corresponding transmitted signals. All investigated materials present a relatively low refractive index (compared with glass and many crystalline materials) and low dielectric loss.

Chapter 6 is divided into three sections. Firstly, the main conclusion and contribution are summarized based on the abovementioned results. Secondly, future perspectives and research directions are proposed. Thirdly, peer-reviewed publications and conferences attended during the Ph.D. study are listed.

CHAPTER 2

EXPERIMENTAL EQUIPMENT

Figure 2.1: Image of TPS Spectra 3000 system.

The commercial pulsed terahertz (THz) time-domain spectroscopy (TDS) system (TPS Spectra 3000 from TeraView, Cambridge, UK, shown in Fig. 2.1) is utilized in this thesis, and the corresponding schematic diagram is shown in Fig. 2.2. The generation of THz pulsed radiation is based on a photoconductive switch. 780 nm pulses with sub-100 femtosecond pulse duration at a repetition rate of 100 MHz and an average output power of $>$ 65 mW are divided by a beam splitter. They are directed toward the THz emitter and receiver. Few-cycle THz pulses with bandwidth ranging from 60 GHz to 3 THz are generated in a biased gallium arsenide (GaAs) antenna after excitations by femtosecond pulses. Coherent detection of the terahertz radiation is performed in a similar photoconductive antenna circuit by gating the photoconductive gap with a femtosecond pulse synchronized to the THz emission. A delay line is incorporated into the probe beam to change the differ-

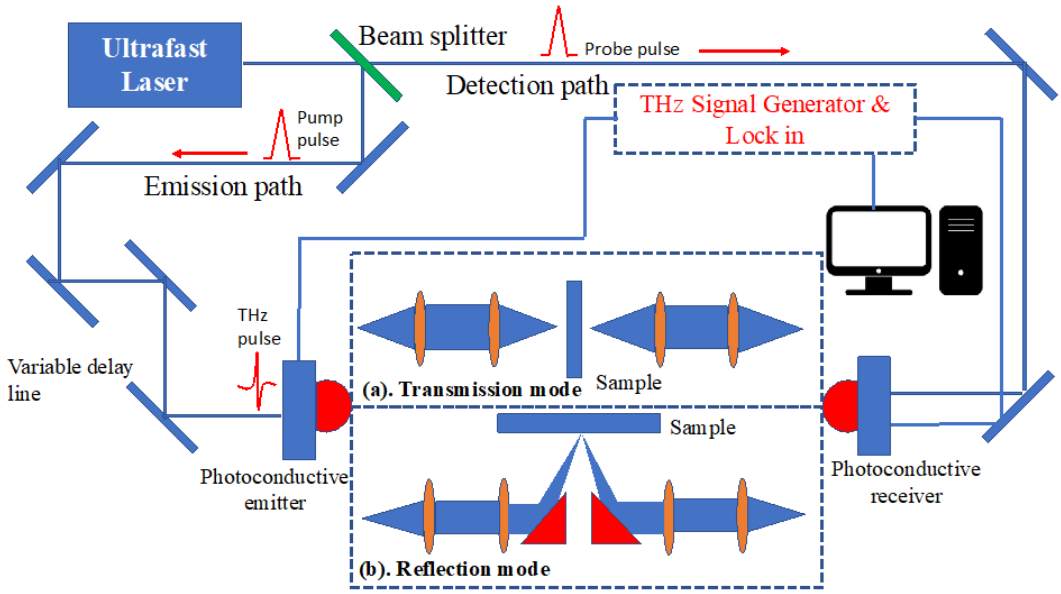

Figure 2.2: Schematic diagram of THz TDS system in both reflection and transmission mode.

ence in the optical delay between the incoming THz pulse and the probe laser pulse at the receiver. A bias is also applied across the emitter and receiver to generate a time-gated output signal. By taking the Fourier transform, the spectrum can be obtained.

Reflection raster-scanned imaging can be performed using this commercial THz system through a set of horizontal motorized stages moving in x- and y- directions, shown in Fig. 2.3, and the scan speed is controlled precisely by integrated software. The delay line can also be adjusted with integrated TPS Spectra 3000 software to peak signal and measure spectra. Figure 2.3(a) is the top-view photograph of a flat-bed gantry system that is in conjunction with the TPS spectra 3000 system and a fiber-fed emitter/receiver sensor pair. It allows non-specular reflective measurements of an area over 200 mm $\times$ 200 mm with stand-off distances. The z position can be adjusted manually to align the scan plane to the surface of investigated samples. Except for the stand-off raster-scanning module, non-specular (diffuse) reflective measurements can also be achieved by manually repositioning emitter and receiver probes, as shown in Fig. 2.3(b). The emitter and receiver angle range is [$0°$, $45°$]. Dry N_2 can be purged to emitter and receiver heads to remove water vapor

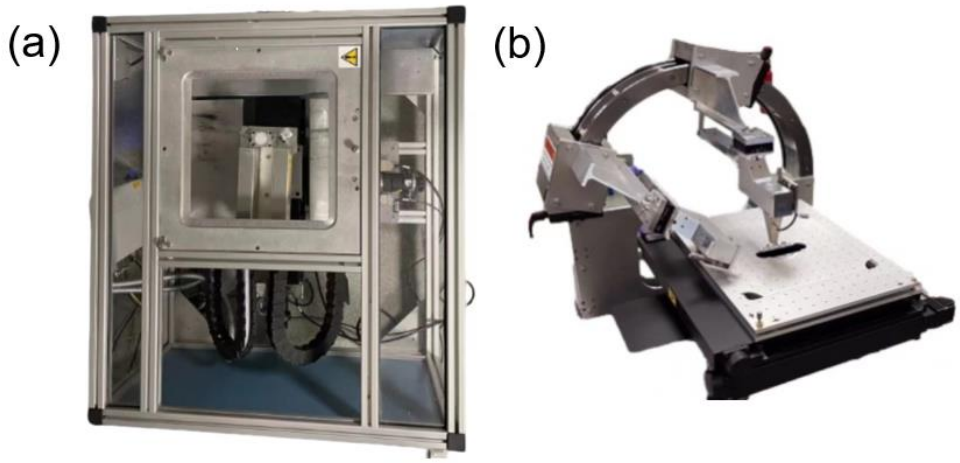

Figure 2.3: (a) Top view photograph of the flat-bed gantry system. (b) Advanced variable angle reflection scan module.

features from the reference and sample spectrum. Owing to the discontinuity of refractive index between two different adjacent layers as a function of depth, multiple reflections off the corresponding interfaces are produced. The amplitude of the reflections is determined by the available dielectric and the optical properties of the constituents ($i.e.$, the indices of refraction and the absorption coefficients). In contrast, the optical delay between two adjacent reflections is proportional to the thickness of the layers. The thickness maps and cross-sectional images can be generated from the data collected using the Teraview supplied image and data analysis software.

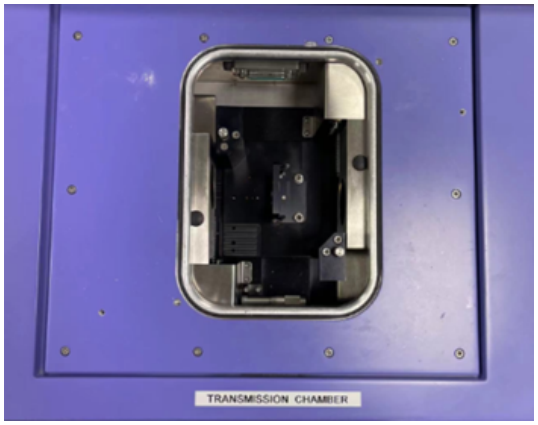

Figure 2.4: Photograph of the transmission chamber.

A transmission experiment can be performed through a transmission module embedded in the THz TDS system, as presented in Fig. 2.4. Dry N_2 is purged into the sample compartment 4-5 minutes before each transmission measurement to suppress atmospheric water vapor absorption. Spectral averaging is also available. For example, 1800 scans will spend 1 minute with 1.2 cm^{-1} spectral resolution. Based on the amplitude and the phase of the recorded transmitted field, the absorption coefficient $\alpha(\nu)$, refractive index $n(\nu)$, complex permittivity $\varepsilon(\nu)$, and loss tangent $\tan\delta(\nu)$ of the studied material can be calculated directly.

CHAPTER 3

TERAHERTZ NONDESTRUCTIVE EVALUATION OF OPTICALLY THIN LAYERS ON STEEL

Due to the ability of THz electromagnetic radiation to penetrate significantly into many electrically insulating materials, THz-based technology has attracted considerable attention to providing quantitative information in-depth in a non-destructive fashion. The echoes reflected from optically thin films might be overlapped partially or even totally in time. In the absence of *prior* structural knowledge of investigated coupons, THz deconvolution by retrieving the impulse response function of the investigated samples is essential to resolve the overlapped echoes and extract the arrival time of superimposed echoes accurately. Even though numerous efforts have been spared within decades to enhance the limitations in-depth, the comprehensive study of each algorithm is limited. Moreover, existing deconvolution techniques still could not meet the demands for some specific cases.

THz reflective imaging is utilized in this chapter for thickness measurement and uniformity characterization of steel coupons from ArcelorMittal. Two specific cases are presented in this chapter. The first case is to measure the thickness of optically thin mill scale films on the steel substrate. Owing to the optically thin thickness of mill scale films in the THz regime (less than 30 μm) echoes reflected from mill scale films will be overlapped totally in time and thus are not visually evident in the raw reflected THz signal, necessitating the utilization of deconvolution techniques to recover the structure of investigated specimens. Three different deconvolution techniques, *namely*, frequency-wavelet domain deconvolution (FWDD), sparse deconvolution (SD) based on an iterative shrinkage algorithm, and autoregressive spectral extrapolation (AR) based on Burg's method are employed to separate overlapped echoes. Compared to the deconvolution performance of FWDD and SD, the AR algorithm seems to be a more reliable thickness measurement technique for all

samples studied.

The second case is to characterize the uniformity of individual layers in a multilayer coating on steel substrates. One novel autoregressive spectral extrapolation based on the modified covariance method (AR/MCM) is proposed to significantly enhance the resolution in depth. Superior to the AR approach based on Burg's method, no obvious peak splitting (single peaks in the impulse response function appearing as double peaks) and frequency bias (spectral peaks shifted concerning their correct positions) are observed after deconvolution. Numerical simulations and experimental measurements verify that the proposed algorithm can be considered an effective tool for the non-destructive characterization of multilayered structures.

3.1 Terahertz deconvolution

Theoretically, the THz time-of-flight (TOF) experiment can be seen as a linear system. Thus, the reflected THz signal (electric field) $r(t)$ in the time domain can be treated as the convolution of the incident THz pulse $i(t)$ with the impulse-response function $h(t)$, which corresponds to the structure and properties of the sample at a given position,

$$r(t) = i(t) \otimes h(t) + e(t) \tag{3.1}$$

$e(t)$ corresponds to noise, which may originate in electrical noise, noisy laser output, and environmental fluctuations [50]. In addition, what we call noise may also be due to reproducible and undesired features in $r(t)$ arising, for example, from atmospheric water-vapor absorption. For a layered sample, $h(t)$ will be zero, except for a set of mutually time-delayed peaks arising from the various interfaces.

We might seek to retrieve the impulse response function $h(t)$ by applying the inverse

Fourier transform following the application of the convolution theorem,

$$h(t) = FT^{-1}[\frac{FT(r(t))}{FT(i(t))}] \tag{3.2}$$

where FT denotes the Fourier transform and FT^{-1} the inverse Fourier transform.

3.1.1 Terahertz frequency wavelet domain deconvolution

Due to low- and high-frequency noise in $r(t)$, direct division often leads to large spikes in the high-frequency region, resulting in severe ringings in the time domain after the inverse Fourier transform. In order to avoid the influence of high-frequency noise, a low- or band-pass filter is usually utilized to augment deconvolution, which can be expressed as,

$$h'(t) = FT^{-1}[FT(f(t)) \times \frac{FT(r(t))}{FT(i(t))}] \tag{3.3}$$

where $f(t)$ is the filter in the time domain. To date, double Gaussian [51], van Hann [26], Wiener [52, 53], and Gaussian filters [51] have been used. The filtering performance is largely determined by the selection of cutoff frequency f_c. Loss of valuable information may ensue as the noise spectrum may strongly overlap with meaningful high-frequency information excluded by the filter.

Quite often, deconvolution, *i.e.*, reconstruction, only with filters often does not provide a satisfactory reconstruction for $h(t)$. To improve the selectivity of the filter, we abandon a naïve low- or band-pass filter and consider a wavelet filter selectively designed to pass meaningful stratigraphic information while excluding noise. To begin, one must choose wavelet basis functions that resemble the typical THz signal $i(t)$, and thus the individual echoes [54]. In contrast to the Fourier transform, which uses an infinite set of sinusoids as the basis functions, the wavelet transform employs a truncated basis of functions that highly resemble the meaningful features in $r(t)$. Because the ability of a truncated wavelet transform is quite sensitive to the selection of mother wavelet function and the decomposition

level, determining the optimal solution still merits further study. It likely depends on the details on $i(t)$ in a particular experiment. Three criteria, namely the wavelet basis efficiency index (WBEI), the pulse spectral relative entropy (PSRE), and the pulse spectral cumulative error (PSCE), are proposed in Ref. [55] based on the similarity between the selected wavelet function and the typical THz signal. Three better mother wavelets, *sym4*, *bior3.3*, and *rbio5.5*, and three not-so-successful mother wavelets in the THz context, *Haar*, *dmey*, and *rbio3.3*, are studied. Of course, the optimal choice may depend on the THz system and the reference-pulse shape. Reference [56] presents subjective and objective methods to determine the optimal decomposition level. Because of the correlation between the detail components and the corresponding approximation components, the optimal deconvolution level is attained when the noise within the complex components is indistinguishable.

3.1.2 Terahertz sparse deconvolution

According to the principle of convolution, the convolution model can be transformed into matrix multiplication as

$$\mathbf{r} = \mathbf{I}\mathbf{h} + \mathbf{e} \tag{3.4}$$

where $\mathbf{I}$ is the convolution matrix whose rows are delayed versions of the reference signal $i(t)$ produced by the apparatus. $\mathbf{r}$ and $\mathbf{h}$ are the discretized matrix form of the reflected signal $r(t)$ and the impulse-response function $h(t)$; $\mathbf{e}$ is the noise vector.

One long-standing approach for solving (3.4) is the classical least-squares method, expressed as:

$$\min_{\mathbf{h}} \frac{1}{2}\|\mathbf{I}\mathbf{h} - \mathbf{r}\|_2^2 \tag{3.5}$$

where $\|\mathbf{h}\|_2$ stands for the l_2-norm of $\mathbf{h}$, which is defined to be the number of nonzero entries in $\mathbf{h}$. In practice, the least-square solution ignores the ill-posed character of the deconvolution problems and requires numerous iterations to recover $\mathbf{h}$; therefore, regularization methods are required to stabilize the least square solution.

One popular regularization technique, the l_1-norm regularized optimization, is employed to force the retrieval of a sparse vector $\mathbf{h}$ and expressed as

$$\min_{\mathbf{h}} \frac{1}{2}\|\mathbf{I}\mathbf{h} - \mathbf{r}\|_2^2 + \lambda\|\mathbf{h}\|_1 \tag{3.6}$$

where $\|\mathbf{h}\|_1$ stands for the sum of the absolute value of $\mathbf{h}$. The regularization parameter λ controls the trade-off between sparsity and reconstruction fidelity. The most impressive advantages of l_1-norm regularized optimization over the l_0- and l_2- norm regularized optimization is that it is not NP-hard [57], and can achieve sparse solution of Eq. (3.4). The SD-based approach has been widely applied to processing seismic and ultrasonic signals, speech recognition, and image reconstruction.

One of the standard algorithms for solving l_1-norm regularized optimization is the iterative shrinkage algorithm (IST), which involves a matrix multiplication of $\mathbf{I}^\top$ and $\mathbf{I}$ and a shrink/soft threshold operation in each iteration, and is given by

$$\mathbf{h}_{k+1} = \Psi_{\tau\lambda}(\mathbf{h}_k - \tau\mathbf{I}^\top(\mathbf{I}\mathbf{h}_k - \mathbf{r})) \tag{3.7}$$

where τ is the step size and the soft-threshold operator $\Psi_{\tau\lambda}(y) = soft(y, \tau\lambda)$, which is defined as $soft(y, \tau\lambda) = sign(y)max(|y| - \tau\lambda, 0)$. Note that $\mathbf{I}^\top(\mathbf{I}\mathbf{h}_k - \mathbf{r})$ is the gradient of the data-fidelity term $\frac{1}{2}\|\mathbf{I}\mathbf{h} - \mathbf{r}\|_2^2$, demonstrating that each iteration takes a step τ along the direction given by the negative gradient of the date-fidelity term. Due to the simplicity and the low computational cost of each iteration, the first-order IST method is an attractive choice to address the l_1-norm regularized least square problem. One typical example is that Dong *et al.* extracted the qualitatively and quantitatively stratigraphy of a seventeenth century oil painting *Madonna in Preghiera* successfully using this approach [58].

3.1.3 Terahertz autoregressive spectral extrapolation

Autoregressive spectral extrapolation (AR) is an alternative to Discrete Fourier Transform (DFT) that utilizes the history of a signal to extract valuable information hidden in the signal. Therefore, it can achieve high resolution for a short time series. Theoretically, the AR-based approach extrapolates the frequency components within low-signal to noise ratio (SNR) regions based on the frequency components in the high-SNR regions. A "quasi-ideal" impulse response function will be obtained, and therefore, the resolution in depth will be enhanced eventually.

During the AR process, assuming frequency ω_i within a window $\omega_{i_L} < \omega_i < \omega_{i_H}$, where ω_{i_L} and ω_{i_H} define the upper- and lower- frequency limits of that window. The AR model serves as a prediction filter to find data components outside the window $[\omega_{i_L}, \omega_{i_H}]$. For $i > i_H$ using the forward-prediction equation

$$\hat{\omega_i} = -\sum_{k=1}^{p} a_k \omega_{i-k} \tag{3.8}$$

similarly, the backward prediction filter is used to find the missing component for $i < i_L$,

$$\hat{\omega_i} = -\sum_{k=1}^{p} b_k \omega_{i+k} \tag{3.9}$$

where p is the order of the AR process, and a_k and b_k are the coefficients of the AR forward and backward prediction filter, respectively.

The performance of AR is closely related to the selection of bandwidth with high SNR and the p. A small or large value of p, for example, will lead to the failure to represent the subtle features or overfitting of all features, even including the spurious noise features, respectively. The optimal AR coefficients are determined by Akaike's information-theoretic criterion (AIC), a widely used goodness-of-fit criteria to qualify the information loss, which

is defined as

$$AIC[p] = N \log(\sum_{i=i_L}^{i_{pL}} \|\hat{\omega} - \sum_{k+1}^{p} b_k \omega_{i+k})\|^2 + \sum_{i=i_{pH}}^{i_H} \|\hat{\omega} - \sum_{k+1}^{p} a_k \omega_{i-k})\|^2) + 2p \qquad (3.10)$$

here, i_{pL} and i_{pH} correspond to the low- and high-frequency limit of the window band within which the data points are kept the same and serve as the base of the AR model. According to Akaike's theory, the minimum value of AIC corresponds to the best-fit of the AR model [59, 60]. There are also other well-known criteria for the order selection, such as Rissanen Minimum Description Length [61]. Because of the stability and simplicity, Burg's method is usually used to minimize the sum of squares of the forward and backward prediction error term of AIC. More details on Burg's method are found in [30, 62].

3.2 Terahertz thickness measurement of mill scale layer on steel

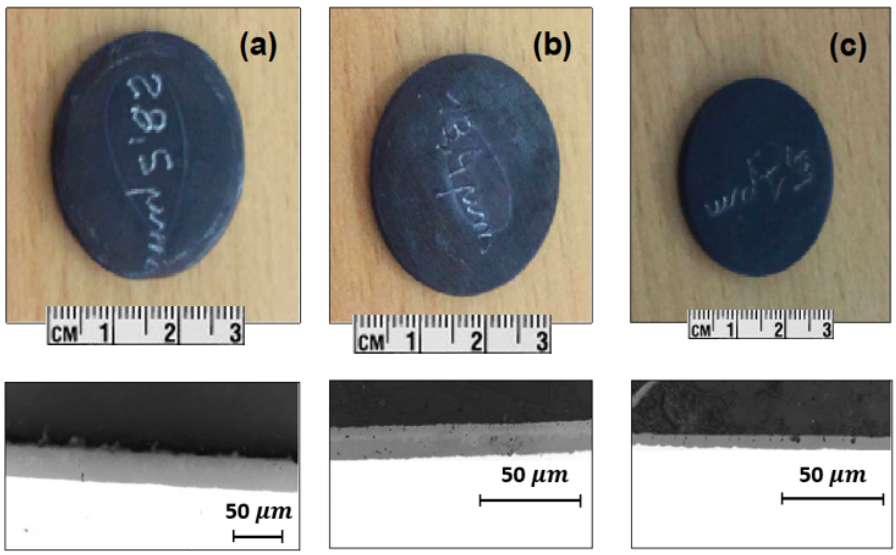

Figure 3.1: Optical photographs of the three scale films of thickness (a) 28.5 ± 1.4 μm, (b) 13.4 ± 0.9 μm, and (c) 5.1 ± 0.3 μm on steel substrates. The steel disks are approximately 3 cm in diameter for all samples. Lower panels show cross-sectional optical micrographs through the samples.

Mill scale is a mixture of iron oxides [iron (II) oxide FeO (wüstite), iron (III) oxide

Fe_2O_3 (hematite), and iron (II, III) oxide Fe_3O_4 (magnetite)] that forms on steel during the hot-rolling process. Wüstite, in particular, is a relatively uncommon phase but may be the dominant constituent of scale at early times before this metastable phase decays into other iron oxides. At room temperature, wüstite is electrically insulating; hematite is also insulating, though magnetite is conducting. In the manufacturing process of rolled steel, a tertiary mill scale may be desirable to suppress surface corrosion, but later, when the steel is to be finished, the presence of the mill scale may inhibit the adhesion of coatings. Scale is thus typically removed before coating through acid pickling or other techniques. Being able to determine in a nondestructive and noncontact way the thickness of the scale layer is useful to optimize the pickling process and other production processes related to steel manufacturing. The determination of mill-scale thickness is typically carried out by destructive testing, which is slow and expensive and requires interrupting the production and shipment of the steel to cut coupons to be tested. If the scale is not fully removed due to insufficient pickling, subsequent coating adhesion is compromised. If pickling is too aggressive, excess toxic material is generated along with higher energy costs.

In this section, THz reflectometry is employed to analyze the thickness of three scale films with thicknesses of 28.5 ± 1.4 μm, 13.4 ± 0.9 μm, and 5.1 ± 0.3 μm on steel substrate, as shown in Fig. 3.1. The films consist of a single scale layer grown under controlled conditions on the interstitial-free steel substrate. Destructive measurements of the cross-sections, based on optical microscopy, were carried out independently to estimate film thicknesses, which are not uniform across the disks, and are reflected by the ranges of values given. The scale films were fabricated under an atmosphere of 20.9 % oxygen and 15 % water vapor. The growth duration and temperature were 2 min at 600 °C for the film of a thickness of 28.5 ± 1.4 μm, 4 min at 650 °C for the thickness of 13.4 ± 0.9 μm, and 3.5 min at 750 °C for the thickness 5.1 ± 0.3 μm. The procedure for surface preparation before scale growth is proceeded by cleaning with ethanol and then light manual polishing at 800 °C for a few seconds to remove any lubricant and hydroxide residue due to preparation and

storage. The scale comprises three iron oxides: wüstite, hematite, and magnetite. Wüstite is the mineral name of iron (II) oxide; Magnetite corresponds to iron (II, III) oxide and hematite to iron (III) oxide. Wüstite is an unstable phase that in the atmosphere undergoes a reaction over the course of weeks to months, depending on temperature and humidity, resulting in magnetite [63]. Wüstite is a poor electrical conductor at 1 THz [64], permitting the incident THz wave to propagate within the material. The same as hematite. Due to the conductive characteristic of magnetite, it is less prone to be characterizable at significant depth through THz reflectometry. Good electrical conductors have high THz reflectivity; THz waves will not significantly penetrate good conductors, such as the underlying steel.

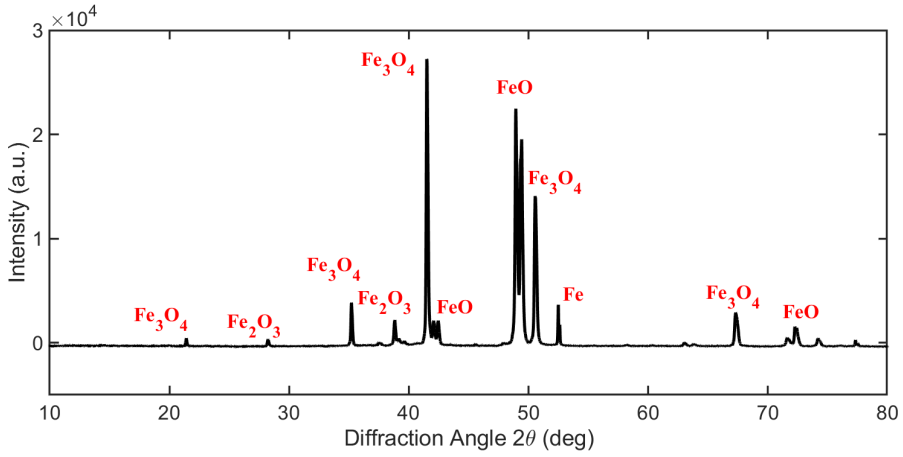

Figure 3.2: X-ray diffractogram of 28.5 ± 1.4 μm thick sample. Diffraction lines associated with various iron-oxide phases are indicated.

After the THz measurements, the composition of the films was verified by x-ray diffraction (XRD) (D2 Advanced x-ray Diffractometer, Bruker, Germany) in the 2θ range of 10 – 80° and scanned with 300 W Co anode radiation produced by a ceramic X-ray tube. The x-ray diffractograms of the 28.5 ± 1.4 μm thick film are shown in Fig. 3.2. Evidence of wüstite, as well as other iron-oxide phases, is present in the x-ray diffractogram. The presence of magnetite and hematite peaks is expected due to the instability of wüstite, and the relative intensities of the peaks indicate the concentrations of each iron oxide in the sample. Based on the Rietveld refinement principle, by adjusting the crystallographic

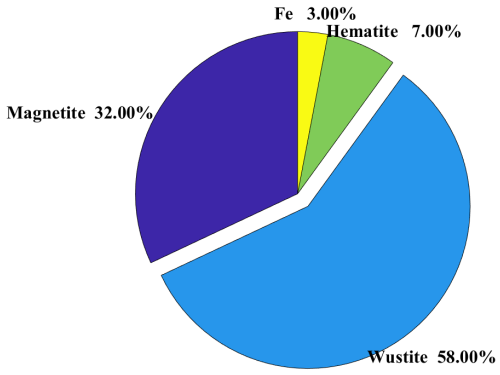

Figure 3.3: Estimated proportion of various iron oxides in the 28.5 ± 1.4 μm sample based on XRD data.

parameters and the proportions of each phase so as to create the simulated diffractogram closest to the experimental diffractogram, the content of each indexed phase in this sample could be estimated, as presented in Fig. 3.3. It shows that the wüstite is the dominant phase (58 % by mass) in the scale films.

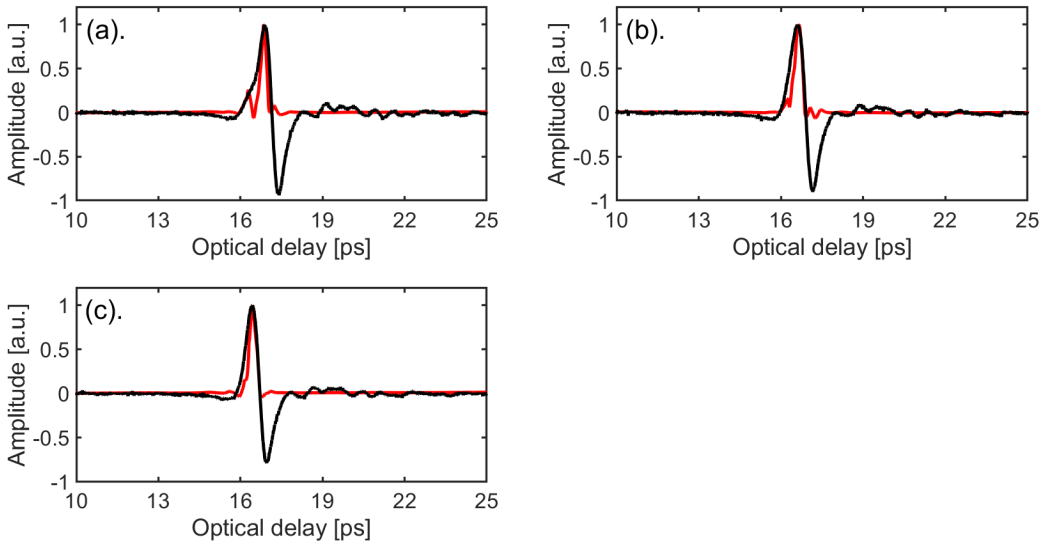

Figure 3.4: The raw reflected THz signal $r(t)$ (black) and the impulse-response function $h(t)$ reconstructed by FWDD (red) for scale films with thicknesses (a) 28.5 ± 1.4 μm, (b) 13.4 ± 0.9 μm, and (c) 5.1 ± 0.3 μm.

The THz experiments were carried out in an air-conditioned laboratory at 22 °C with humidity $< 48\%$. Otherwise, the samples were stored in a dry box to retard the transfor-

mation of wüstite from transforming into magnetite. The experiments shown here were conducted within the three months of sample fabrication to ensure that the scale films were primarily composed of wüstite. The reference pulse produced by the apparatus was recorded first by setting a bare metal plate (*i.e.*, an excellent THz reflector) at the sample position. In particular, numerous water vapor absorption lines are evident in the spectrum. The influence of water vapor absorption is eliminated by conducting measurements in dry nitrogen or *via* various denoising techniques.

Once the reference pulse was characterized, we proceeded with THz TOF tomography. The samples were raster-scanned by a set of motorized stages moving in the transverse x- and y- directions in 100 μm steps over the entire sample (Due to the spectral bandwidth and the relatively high numerical aperture of the THz optics, the transverse resolution is limited to $\sim$ 300 μm). The data sampling period in this measurement is set to T_s = 0.0116 ps. Each recorded reflected temporal THz waveform contains 4096 data points, and the signal is averaged over 10 shots per pixel. For this sampling rate, the entire frequency spectrum obtained by a fast Fourier transform is from 0 to 85.99 THz, containing 4096 data points.

The reflected THz signals as received (the *raw* signals) from the samples with various film thicknesses are shown in Fig. 3.4. The shapes of the reflected THz signals are superficially similar to the reference THz signal, and the echoes off the air/scale and scale/steel interfaces temporally overlap and are not visually distinguishable in the raw reflected signals for any of the three samples. [The impulse response function $h(t)$ governing the measurement, as discussed above, relates the reflected THz signal $r(t)$ to the reference THz pulse $i(t)$. In the ideal case that the reference is an impulse, $\delta(t)$, the reflected signal would be $h(t)$.] In order to separate those overlapped echoes and reveal the structural properties of the samples, a standard frequency-domain approach, frequency-wavelet domain deconvolution (FWDD), is first applied at each pixel. The approach is described in detail in Ref. [26]. The idea is to reconstruct the transfer function $H(\nu)$ with ν the frequency [Fourier transform of the impulse response function $h(t)$; lower case letters with argument t stand

for time-dependent functions; upper case letters with argument ν stand for their respective Fourier transform and are functions of frequency ν] ideally as $H(\nu)$ = $R(\nu)$ / $I(\nu)$, where $R(\nu)$ and $I(\nu)$ are the Fourier transforms of $r(t)$ and $i(t)$, respectively. The problem is that in frequency ranges where noise dominates, this ratio is subject to substantial error.

We implement FWDD after first low-pass filtering to eliminate spurious spikes in the high-frequency region; FWDD itself corresponds to projecting the filtered signal onto a truncated basis of wavelets chosen to resemble the THz pulse $i(t)$, and thus improves the SNR by wavelet denoising. In other words, FWDD is a filter specially chosen to pass features resembling $i(t)$. Finally, $h(t)$ is reconstructed by taking the inverse Fourier transform of the transfer function $H(f)$ obtained by the procedure described above. We first discuss the low-pass filter applied prior to FWDD itself. A Hanning window function is chosen as the filter function. The cutoff frequency f_c = 3.5 THz is chosen t to suppress the low-SNR band of the reference and reflected signals. Due to the THz bandwidth generated by TPS spectra 3000 (60 GHz to 3 THz), we find that if f_c is lower than 3 THz, some weak though valuable features in the signals would be treated as system noise, and be eliminated by the frequency-domain filter; if f_c is larger than 4 THz, residual background noise in frequency-domain blurs the valuable information in the time and frequency domains. For wavelet denoising, $symlet$ (sym4) wavelets were used with a decomposition level equal to 7; no significant improvement is achieved with higher depth to justify the extra computational expense. The estimated impulse responses $h(t)$ when applying FWDD are shown in Fig. 3.4. While the 28.5 μm film might nominally be within the axial resolution limit of FWDD, attenuation (reducing the amplitude of the echo from the back scale/steel interface) reduces the usable THz bandwidth so that the high-frequency part of the detected spectrum lies below the noise floor, We, therefore, conclude that FWDD is not successful even on the thickest film studied. Because the wavelet basis chosen is well suited to the reference pulse, it is not likely that a different basis (or a different filter) will improve the situation.

Next, in order to attempt to reconstruct the layer structure, another technique, namely

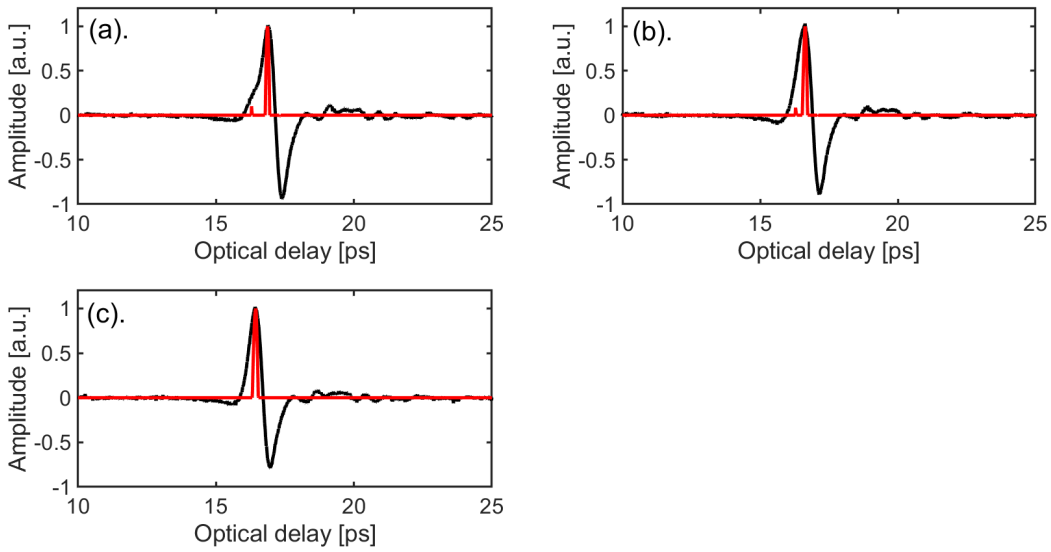

Figure 3.5: The raw reflected THz signal $r(t)$ (black) and SD-impulse-response function $h(t)$ signal (red) for films of thicknesses (a) 28.5 ± 1.4 μm, (b) 13.4 ± 0.9 μm, and (c) 5.1 ± 0.3 μm.

sparse deconvolution (SD), is applied to analyze these samples. SD is a time-domain approach to reconstruct $h(t)$. Heuristically, SD works as follows. The impulse response functions $h(t)$ for layered structures can be treated as a class of signals comprised of a limited number of discrete echoes associated with a reflection from each material interface (multiple echoes are typically too weak to be of importance) on an otherwise signal-free background; therefore, $h(t)$ has a sparse representation (it will be a sequence of sharp peaks on a zero background), which means that only a limited number of data points have nonzero values. By exploiting the sparse constraint, the algorithm focuses on detecting interfaces and can be expected to lead to a better dynamic range than the FWDD technique. Details can be found in Ref. [28].

In the SD algorithm, a regulation parameter λ controls the amplitude of the regularization. Moreover, the energy is minimized by iterative thresholding. In the case of soft-thresholding employed here, the step size τ should obey

$$\tau < \frac{2}{\|\mathbf{I}^\top \mathbf{I}\|_2}$$

Considering the SNR and the tradeoff between the sparsity of the impulse response function h(t) and the residue norm, the regulation parameter λ = 0.8 and the value of the step size τ is set to $1.5/\|\mathbf{I}^{\top}\mathbf{I}\|_2$. We checked that similar results were obtained consistently for λ and τ. Balancing the accuracy of the result and the computational time, the number of iterations is selected as 3000.

The corresponding deconvolved signals are shown in Fig. 3.5. Two pronounced echoes can be identified clearly for all the samples. The first echo, having the stronger intensity, originates from the air/scale interface, while the second echo of lower amplitude is due to the scale/steel interface. Multiple reflections are expected to be weak and are thus not identified in the SD reconstruction of $h(t)$. The optical thickness of the coating can be calculated from the time delay between the first and second peaks in the reconstructed $h(t)$ and the refractive index of scale. The delay between the first and second echoes for the 28.5 μm, 13.4 μm, and 5.1 μm films is 0.9 ps, 0.4 ps, and 0.16 ps, respectively. The physical thickness of the film is obtained from

$$L_{layer} = \frac{\Delta t}{2} \frac{c}{n_{mill\,scale}} \tag{3.11}$$

where c is the *in-vacuo* speed of light, Δt is the time delay between the first and second echoes, the factor $\frac{1}{2}$ arises since the THz pass through the film twice in the reflection geometry and $n_{mill\,scale}$ is the refractive index of mill scale. Owing to the mixed nature of mill scale, the refractive indices of mill scale vary with the oxide composition. Based on the nearly frequency-independent refractive indices of wüstite and hematite within the THz regime, which are $\sim$ 5.0 [65] ($\sim$ 4.7 [66]) and $\sim$ 5.5 [67], respectively, owing to the dominated wüstite phases in mill scale compared with other iron oxide phases, the refractive indices of mill scale film we approximate to 4.7 after accounting for filling factor. In turn, the SD-reconstructed physical film thicknesses are estimated, for a given pixel, to be 28.4 μm, 12.8 μm, and 9.6 μm, which are close to the independently measured ranges of values 28.5 μm ± 1.4 μm, 13.4 μm ± 0.9 μm, and 5.1 μm ± 0.3 μm obtained by destructive cross-sectional measurement. In particular, the two thicker films are within the thickness

variation across the samples of the nominal thicknesses. These results indicate that SD is an effective approach to obtaining the structural properties for the two thicker films. SD, however, appears to fail to provide a high-quality estimate of the thickness of the 5.1 μm film for the explored parameter ranges. SD cannot distinguish multiple echoes if the SNR is too low if the echoes are too close, and/or if the sampling time is too long. In addition, dispersion in the optical constants results in pulse spreading [68], which may degrade the accuracy and axial resolution for SD, though it is not likely to be an issue with thin films.

Since SD was not successful in providing a high-quality reconstruction of the impulse response function $h(t)$ for the thinnest film, we resort to another technique, AR extrapolation [30], which extends the exploitable spectral bandwidth and can be expected to lead to a higher axial resolution. The procedure works as follows. We first obtain $H(\nu)$ in the frequency band where SNR is high from the experimental data as the ratio $R(\nu)$ / $I(\nu)$. In our case, the information we will exploit is that we expect the transfer function $H(\nu)$ to be a sinusoid for layers on a reflective substrate due to the Fabry-Perot effect. Lastly, the reconstructed $H(\nu)$ is inverse Fourier transformed to obtain $h(t)$ and the time delays between peaks are used to determine the relevant optical delays and, in turn, the film thickness.

Unlike FWDD, which discards information as a consequence of filtering, *namely* the frequency components in the low SNR regions in order to suppress anomalous spikes that would otherwise appear in $H(\nu)$, AR deconvolution aims at reconstructing the missing frequency components in precisely the low-SNR regions. FWDD relies on frequency filtering, whereas AR seeks to estimate missing frequency information. Therefore, the entire frequency spectrum of the impulse response function $h(t)$ is estimated, and the enhanced resolution based on these 'quasi-ideal' impulse response functions $h(t)$ is achieved.

Using the AR model as a prediction filter, the missing data in the regions below 0.15 THz and above 2 THz can be extrapolated clearly for all samples. The echo from the scale/steel interface can also be seen clearly. We find that the axial resolution of AR is higher than SD and, we shall see, reliably provides the film thickness, even for the thinnest

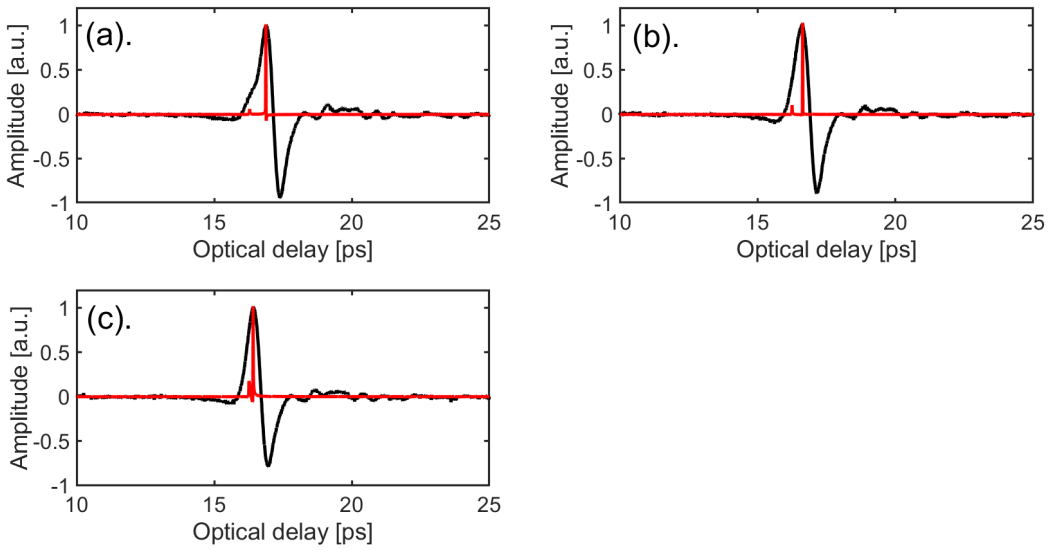

Figure 3.6: Deconvolution results based on AR (red) and the raw THz signal (black) reflected from the calamine sample: (a) 28.5 ± 1.4 μm, (b) 13.4 ± 0.9 μm, and (c) 5.1 ± 0.3 μm, respectively. The estimated frequency spectrum (up to 5 THz) is based on the AR method for each sample.

film. This is consistent with our previous work [30] that has found that AR can be more effective than SD for single-layer structures. The deconvolved signal based on the reconstructed transfer function $H(\nu)$ can also be compared with the spectra of the raw reflected signals, as shown in Fig. 3.6. Due to the estimation and recovery of the frequency components throughout the entire spectrum, the second echo, corresponding to the scale/steel interface, is also identified in all cases. We observe that the calculated thickness based on the optical delay between the two positive echoes matches well with the nominal thickness of 5.1 ± 0.3 μm.

Table 3.1: Comparison of calculated thickness from SD and AR with destructive metrology of micro-sample cross-sections. The mean μ and standard deviation δ of scale thickness are obtained from 20 different pixels for each sample.

μ_{SD} (μm)	δ_{SD} (μm)	μ_{AR} (μm)	δ_{AR} (μm)	$\mu_{cross-section}$ (μm)	$\delta_{cross-section}$ (μm)
28.1	0.6	28.05	0.82	28.5	1.4
12.8	0.63	13.3	0.52	13.4	0.9
6.6	0.41	5.7	0.39	5.1	0.3

To estimate the uniformity of the THz-based measurement of the films, 20 pixels associated with various spatial positions on the samples for each film are selected randomly, the minimum distance between each measured pixel is $\sim$ 500 μm. The reflected THz signals at those pixels are recorded. By measuring the optical delay between the first and second positive echoes, the thickness of the film at each pixel can be calculated with the equation mentioned above. The mean and standard deviation for those 20 pixels for each film is obtained. Table 3.1 shows the calculated scale film thickness based on AR for nominal 28.5 μm, 13.4 μm, and 5.1 μm matching fairly well with the cross-sectional measurements. Table 3.1 summarizes all the results for SD. Hence, we conclude that the axial resolution in this single-layer film is significantly enhanced by AR deconvolution, and the structural properties of scale films with thickness down to $\sim$ 5 μm can be resolved by AR deconvolution. Of note, the cross-section method only gives the thickness along the cross-section; the film thickness was thus estimated based on the assumption that the entire film is uniform in thickness. The AR result, on the contrary, enables one to explore uniformity across a surface. This is a further advantage of the THz measurement versus traditional destructive cross-sectional measurements.

In summary, THz reflectometry may provide a reliable nondestructive and contactless modality to measure scale film thicknesses on metals down to at $\sim 5\mu m$, and by extension other electrically non-conducting oxide film thicknesses. THz pulsed techniques for this application proved successful only due to the combined exploitation of the physical measurement technique with the appropriate signal-processing techniques.

3.3 Terahertz quality measurement of multilayer coatings on steel

Although AR deconvolution based on Burg's method (AR/BM) has attracted interest due to its super-resolution capability [30, 69], due to the high tendency of line-splitting (reconstructions including artefacts that suggest additional layers that are not present) when a larger order p is applied as well as the additional constraints from Levinson-Durbin re-

cursion [30], the AR/BM result may not provide a reliable reconstruction of multilayered coatings, especially when the absence of *prior* knowledge of the various layers, since, in practice, the choice of parameters to provide reliable reconstruction may require one to know the layer thicknesses beforehand, which, needless to say, defeats the entire purpose.

AR-based on the modified covariance method (AR/MCM) to minimize the sum of squares of the forward and backward prediction errors, is proposed and employed in this study [69]. Compared with AR/BM, the most remarkable advantage of AR/MCM is the reduced occurrence of line-splitting due to the restriction in the AR order selection. A drawback is that the stability of AR/MCM cannot be guaranteed when the poles of the system lie outside the unit circle. In order to avoid these singularities, the solution we proposed to stabilize the AR model is to reflect the poles of the model that are outside the unit circle to the inside of the unit circle by reciprocating the magnitude as

$$D_i^{'} = \begin{cases} D_i & |D_i| \leq 1 \\ \frac{1}{|D_i|^2} D_i & |D_i| > 1 \end{cases} \tag{3.12}$$

where D_i are the poles of the system, and $D_i^{'}$ are the updated poles. More details can be found in Ref. [70]. Because of the high sensitivity of the AR model to SNR, the measured data is preconditioned by wavelet denoising to improve the accuracy of AR/MCM. In contrast to typical frequency-domain filters (typically, low-pass and band-pass), the bandwidth of the impulse response function is not narrowed by wavelet denoising.

Numerical simulations were performed first to verify the performance of AR/MCM on multilayered samples. To this end, we consider how AR/MCM performs with synthetic data. An ideal impulse response function $h_0[n]$, which contains 4096 data points with

sampling period T_s= 0.0116 ps, is assumed,

$$h_0[n] = \begin{cases} 0.5 & n = 1560 \\ 0.5 & n = 1620 \\ -0.5 & n = 1680 \\ 1 & n = 1740 \\ 0 & otherwise \end{cases} \tag{3.13}$$

where n is the discrete-time variable and t = nT_s and the subscript 0 denotes quantities estimated from synthesized data. $h_0[n]$ thus consists of a sequence of three discrete-time impulses, and represents a typical three-layer structure; the time interval between consecutive peaks corresponds to the thickness of each layer. After convolution with the measured reference pulse $i[n]$ from the THz system with the impulse response function $h_0[n]$ and adding Gaussian white noise e_0 uncorrelated with respect to n, the reflected THz signal $r_0[n]$ is simulated, as shown in Fig. 3.7. Based on the experimental dynamic range of the THz system, the signal-to-noise ratio of $r_0[n]$ is set to be 50 dB in the simulation. In the following, we shall use the discrete-time argument n and the continuous-time t interchangeably as convenient.

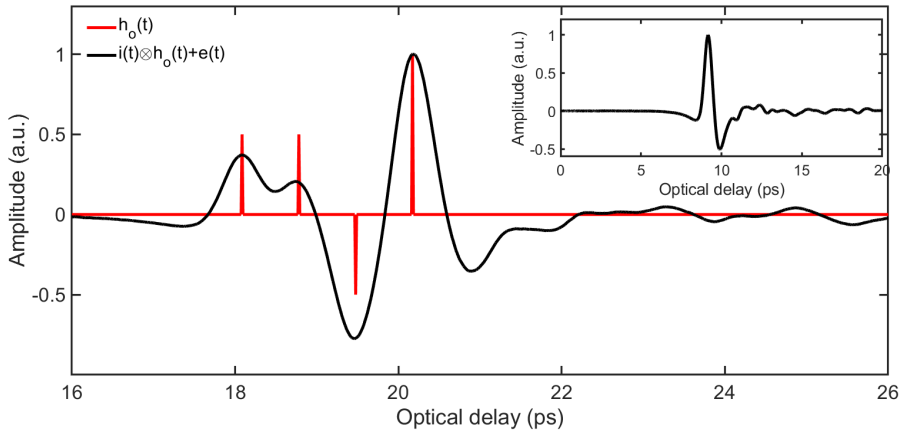

Figure 3.7: Synthetic impulse response function $h_0(t)$ and the simulated reflected THz signal $r_0(t)$. The inset shows the experimental reference signal $i(t)$.

Because of the high sensitivity of AR to noise, the first step in the procedure, before fitting an AR model, is the estimation of the SNR of the reflected signal. Before implementing AR/MCM, a wavelet deconvolution procedure is applied, owing to the high similarity

of the reference pulse with conveniently selected wavelet basis functions [71]. In contrast to the Fourier transform, which employs an infinite set of sinusoids as the basis, the wavelet transform is an efficient representation of a THz pulse because of the time-frequency localization of the wavelet basis function [54], allowing for a highly truncated wavelet basis to be employed. As a result, wavelet denoising selectively drops noise-like features without utilizing a heavy-handed filter such as a low-pass filter. Therefore, the signal bandwidth after wavelet denoising will not be narrowed. In principle, the wavelet technique decomposes a signal by convolving with a low-pass filter and a high-pass filter at each level and removes the wavelet coefficients with small absolute values by thresholding [72]. Based on Ref. [55], balancing the denoising efficiency and computational cost, *symlet* (sym4) wavelets are selected with a level of 5 for the wavelet decomposition.

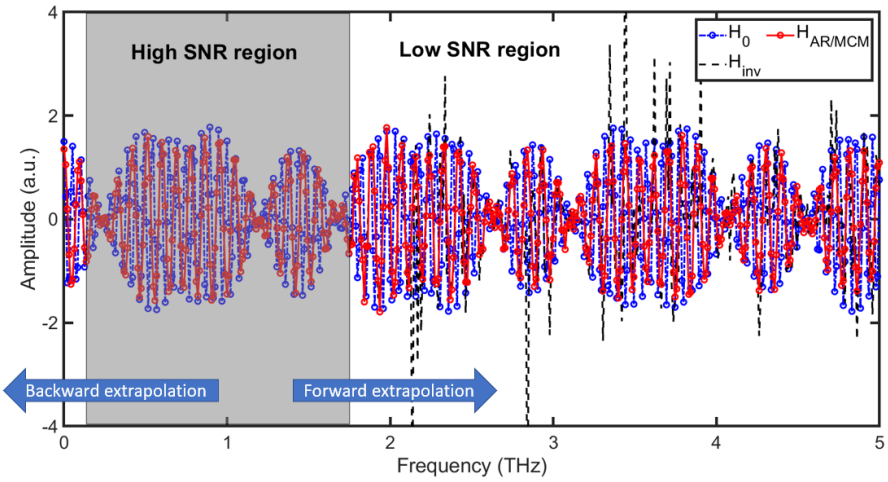

Figure 3.8: Comparison between the deconvoluted spectrum by direct inverse filtering $H_{Inv}(\nu)$ (dashed black) and the estimated frequency spectrum by (red) AR/MCM with wavelet denoising. H_0 (blue) is the transfer function obtained by Fourier transforming the model impulse response function $h_0(t)$.

Figure 3.8 presents the comparison of the deconvolved transfer function (Fourier transform of $h[n]$) $H_{Inv}(\nu)$ by direct inverse filtering and the estimated transfer function $H_{AR/MCM}(\nu)$ by AR/MCM with wavelet denoising. Large spikes due to noise are largely absent from $H_{AR/MCM}(\nu)$. The high-SNR window for the AR model was set to [0.14 THz, 1.75 THz]. By using the data within [0.14 THz, 1.32 THz] for the backward prediction filter and the

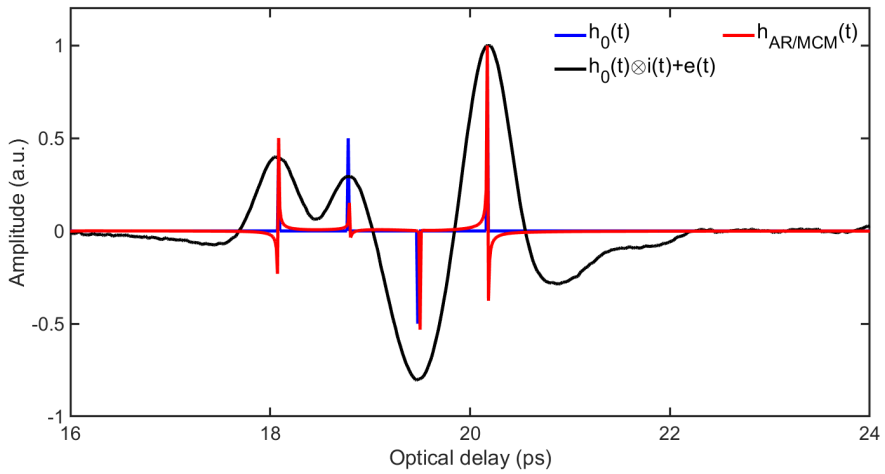

Figure 3.9: Comparison of the simulated deconvolution results $h_{AR/MCM}(t)$ based on AR/MCM (red), the raw reflected signal $h_0(t) \otimes i(t) + e(t)$ (blue), and the assumed impulse response function $h_0(t)$ (black).

data within [0.58 THz, 1.75 THz] for the forward prediction filter, the entire frequency band can be extrapolated. In order to avoid overfitting, the parameters of the forward and backward prediction filters are controlled by AIC. The criterion is found to reach its minimum when the order p is 70. By simply performing the inverse Fourier transform of $H_{AR/MCM}(\nu)$, the reconstructed signal $h_{AR/MCM}(t)$ can be achieved, as shown in Fig. 3.9. Compared with the raw reflected signal $r_0(t)$ from which it is not obvious how one would visually reconstruct the stratigraphy, $h_{AR/MCM}(t)$ exhibits four clear peaks, the exact positions of which are in good agreement with the synthesized impulse response function $h_0(t)$, *albeit* with minor peak shifts as well as the magnitude change, resulting from residual noise even after wavelet denoising as well as the built model. Moreover, the ultimate goal for us is to sharpen the echoes in raw reflected signals and enhance the SNR to improve the temporal resolution, so the amplitude information is not our priority, even though there are also significant. The success of resolving all interfaces demonstrates the potential of AR/MCM for characterizing the individual layer of stacked samples.

We next turn to the experimental study of the nine steel coupons. Three sets of coated steel coupons with different layer configurations, as depicted in Fig. 3.10, to verify and

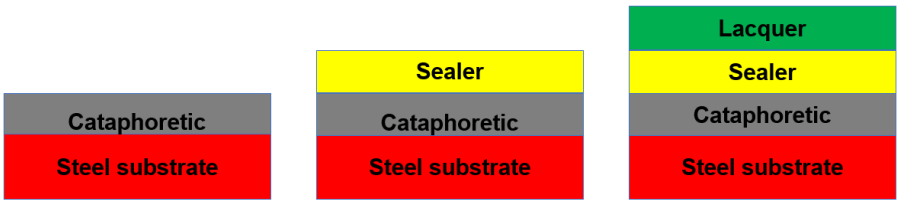

Figure 3.10: The cross-sectional schematic diagrams of the multi-layered samples in this study.

evaluate the performance of the proposed AR/MCM algorithm experimentally. The dimension of all samples is 10 cm × 20 cm. The first set of samples numbered 5, 9, and 10 have a single cataphoretic layer on a flat steel coupon. The second set numbered 12, 14, and 16 has two layers, *viz.*, the cataphoretic layer and a sealer. The third set numbered 11, 15, and 17 has three layers, namely the cataphoretic layer, a sealer, and lacquer. Each layer performs a different function. The cataphoretic layer, which is applied electrochemically, provides corrosion protection to the metal substrate. The function of the sealer is to promote adhesion between the cataphoretic layer and the layer above, and moreover, regularize the rough cataphoretic layer to lead to a smoother overall finish. The lacquer provides ultraviolet protection, resistance to mechanical abrasion, and resistance against chemical attack. In our samples, the lacquer is the thickest layer.

Table 3.2: Mean thicknesses μ and standard deviations δ of cataphoretic layer, sealer, and lacquer for all samples obtained *via* Deltascope measurements.

Sample	Cataphoretic layer		Sealer		Lacquer	
	$\mu\ (\mu m)$	$\delta\ (\mu m)$	$\mu\ (\mu m)$	$\delta\ (\mu m)$	$\mu\ (\mu m)$	$\delta\ (\mu m)$
5	6.6	0.7				
9	14.8	1				
10	21.3	0.9				
16	15.6	0.4	28.4	1.4		
12	20.7	0.4	29	1.2		
14	8.5	0.6	30	1		
15	8.7	0.4	31.1	1.2	35.8	1.4
11	20	0.5	28.9	1.1	36.1	2
17	15.2	0.7	28.1	0.8	36.3	1.9

The thickness of each individual layer of all 9 samples is characterized first using high-resolution Deltascope FMP 30, following the deposition of each individual layer, which is a standard and widely used approach for measuring coatings on ferrous based materials; however, because the eddy-current technique cannot resolve the individual layer thicknesses in the complete multilayer coating, the strategy we applied here to obtain the thickness of all individual layers is to perform multiple measurements at different steps in the layer deposition process. Specifically, an eddy current measurement is performed after the deposition of each layer; simple subtractions can then reveal individual layer thickness. The thicknesses are listed in Table 3.2. THz TOF tomography is thus carried out next and begins with the steel coupons with a single layer composed of the cataphoretic layer.

3.3.1 Single-layer samples

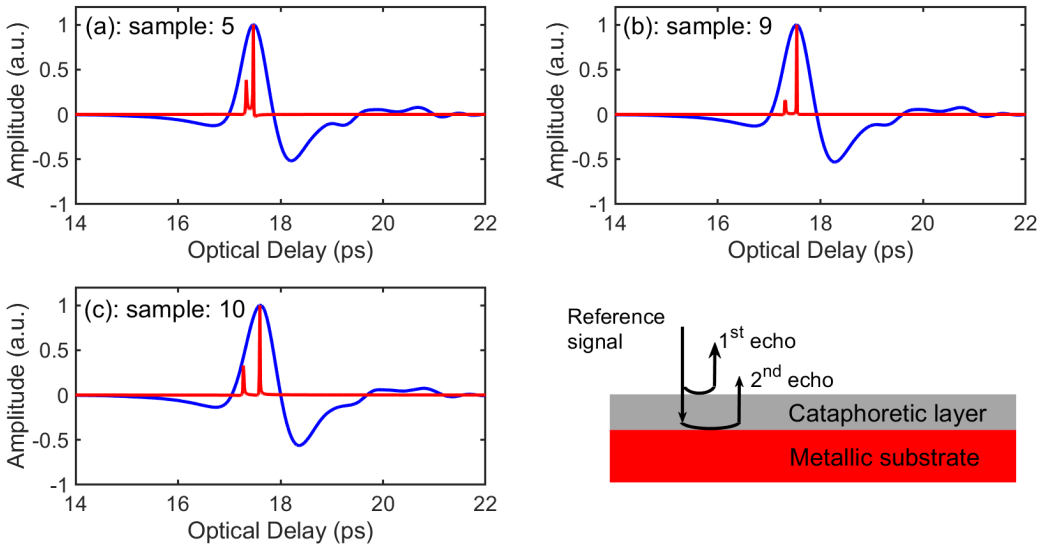

Figure 3.11: The AR/MCM result for samples (a) 5, (b) 9, and (c) 10.

Figure 3.11 shows $h_{AR/MCM}(t)$ for the single-layer coated samples (a) 5, (b) 9, and (c) 10. Two positive echoes, corresponding to the air/cataphoretic layer interface, and cataphoretic layer/steel substrate boundaries, are seen in all cases. The cataphoretic-layer thickness is estimated based on the optical delay between the two positive echoes and on the refractive

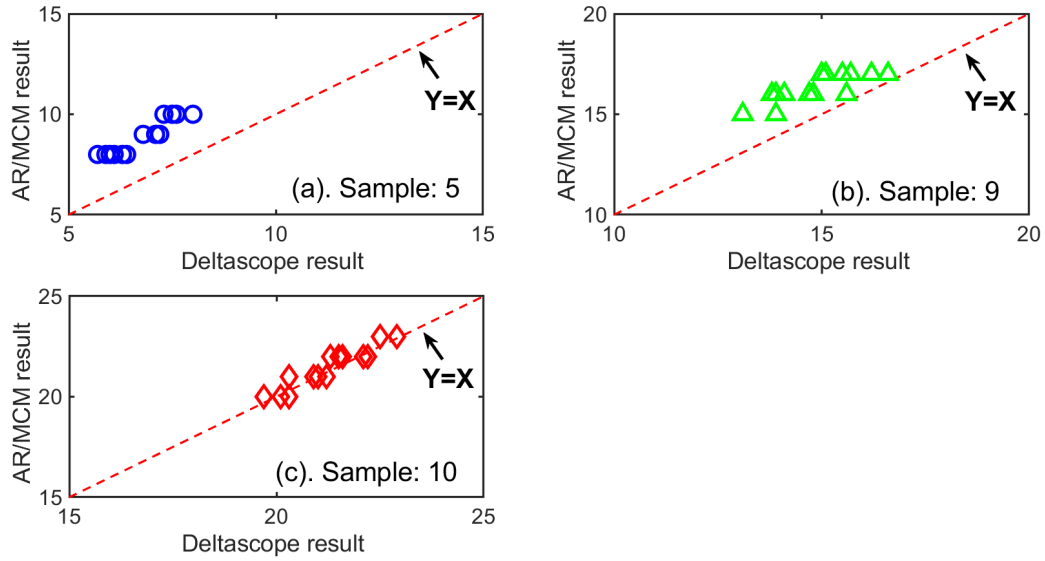

Figure 3.12: Thickness of cataphoretic layer measured by AR/MCM method as a function of thickness measured by Deltascope for samples (a) 5, (b) 9, and (c) 10.

index of cataphoretic material in the THz regime. The optical delay between the first and second positive peaks is (a) 0.14 ps, (b) 0.2 ps, and (c) 0.25 ps, and the refractive index of electrocoating in the THz regime is $\sim$1.72 [25]. Therefore, the physical thickness of the cataphoretic layer on the metal substrate is (a) 12.2 μm, (b) 17.4 μm, and (c) 21.8 μm, respectively. In addition, the uniformity of this layer for samples 5, 9, and 10 are also discussed based on the same 16 pixels that were characterized by the Deltascope (of note, there can be some limited experimental deviation in the pixel positions). The comparison of cataphoretic-layer thickness from Deltascope measurements and AR/MCM for samples 5, 9, and 10 are shown in Fig. 3.12; see below for discussion. Both the weighted linear fit and Y=X are also plotted. The thickness measured by AR/MCM is well correlated with the Deltascope results, confirming the reliability of AR/MCM. To quantify this, the mean square error (MSE) is computed, which is expressed as

$$MSE = \frac{1}{N}\sum_{i=1}^{N}(y_i - y_i^{'})^2 \tag{3.14}$$

where y_i is the thickness value measured by Deltascope, $y_i^{'}$ is the thickness value calculated by AR/MCM, and N is the number of data points; here N is 16. MSE for samples 5,

Table 3.3: MSEs of the thickness of cataphoretic layer based on the Deltascope and AR/MCM for samples 5, 9, and 10.

Sample	MSE of cataphoretic layer (μm^2)
5	8.4
9	2.4
10	2.4

9, and 10 are is given in Table 3.3. The thinner the cataphoretic layer, the larger the corresponding MSE, meaning that the error between AR/MCM and Deltascope measurements increases as the thickness of the cataphoretic layer decreases. The errors result in part from the fact that AR/MCM for the thinner layers may be near its limit of applicability. The thickness of the thinnest cataphoretic layer is close to the minimum time interval that can be distinguished by AR/MCM, which is $\sim 15\ T_s$ [30]. As the thickness decreases further, the two corresponding peaks in $h_{AR/MCM}(t)$ begin to merge, as is seen in Fig. 3.11 (a), and the MSE rises. We have adjusted the parameters of the AR model to separate merged peaks, but the sensitivity of the AR model may lead to worse results. In Fig. 3.12 is shown the cataphoretic-layer thickness reconstructed by AR/MCM versus the measured value by Deltascope. We see an overall tendency in the plots for AR/MCM to give slightly higher values than the Deltascope, with this tendency most pronounced for the thinnest layers. The origin of this discrepancy is the partial overlap of the echoes from the air/cataphoretic layer and cataphoretic layer/steel interfaces, which becomes more severe as the cataphoretic-layer thickness decreases.

3.3.2 Two-layer samples

THz TOF tomographic measurements were also carried out on samples 12, 14, and 16 with a cataphoretic layer and sealer on steel, and the corresponding AR/MCM results are presented in Fig. 3.13. The echo sequence—positive, negative, positive—is seen, corresponding to reflections from the air/sealer, sealer/cataphoretic layer, and cataphoretic layer/steel

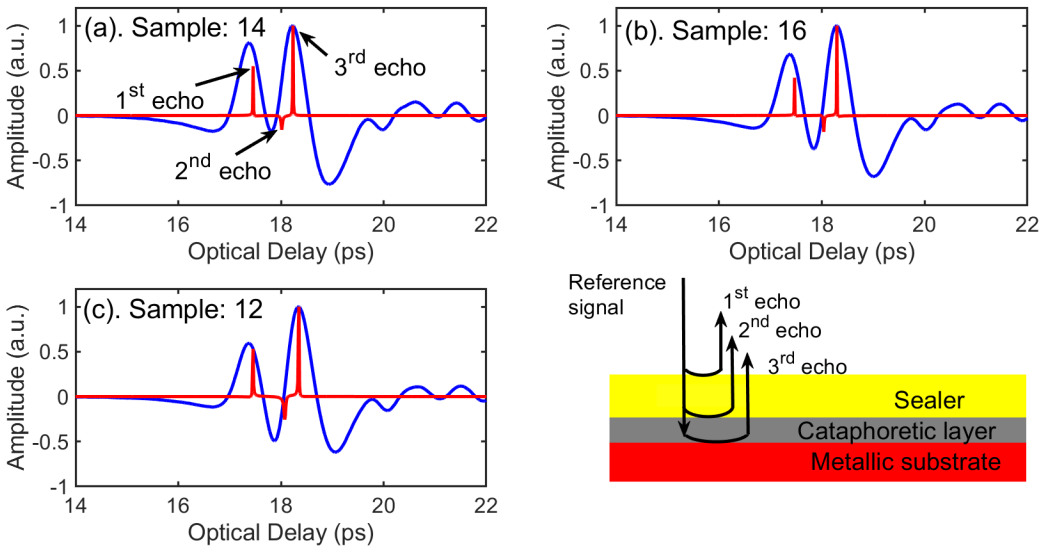

Figure 3.13: The AR/MCM result of samples (a) 14, (b) 16, and (c) 12.

Table 3.4: MSEs of the thickness of cataphoretic layer and sealer based on Deltascope and AR/MCM for samples 12, 14, and 16.

Sample	MSE of cataphoretic layer (μm^2)	MSE of sealer (μm^2)
12	1.2	0.4
14	4.2	0.4
16	1.8	0.7

interfaces, respectively. The negative peak at the sealer/cataphoretic layer interface results from the phase shift of the THz signal as the refractive index of the cataphoretic layer is lower than that of the sealer. The individual thicknesses of the cataphoretic layer and sealer are computed. The assumed refractive index of the sealer is 2.61 [25]. Figure 3.14 shows the comparison of the cataphoretic layer and sealer thicknesses obtained by Deltascope measurements and AR/MCM. The MSEs for samples 12, 14, and 16 are presented in Table 3.4. For the sealer, the low MSE demonstrate excellent agreement with the results obtained directly from Deltascope. Somewhat less agreement is seen for the cataphoretic layer, because of the partial overlap of the echoes from the sealer/cataphoretic layer and cataphoretic layer/steel interfaces, leading to uncertainty in the time delay between the echoes. Similar to the remarks above for samples 5, 9, and 10, the error associated with the

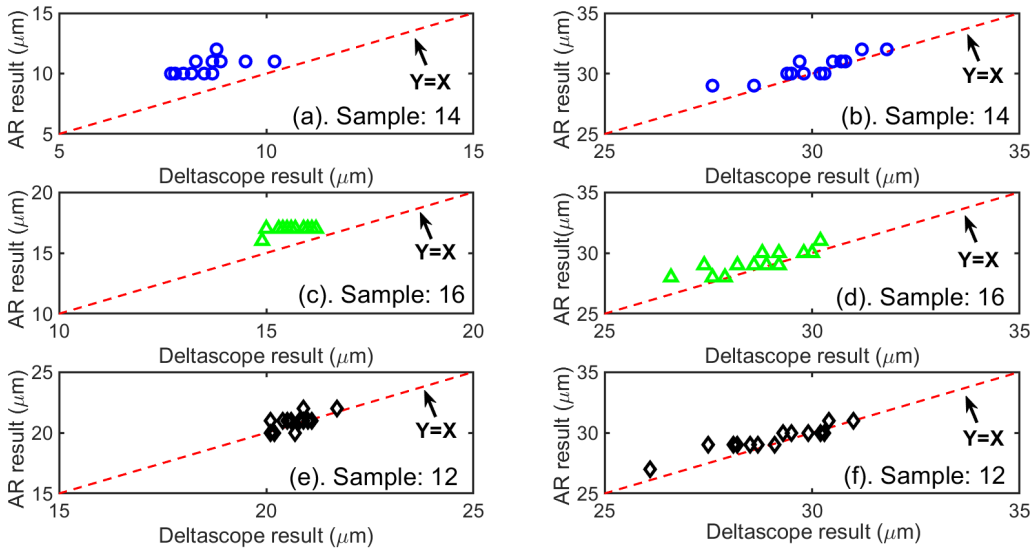

Figure 3.14: Comparison of the thickness of individual layers for samples 12, 14, and 16 between AR/MCM and the Deltascope. Left column: the thickness of the cataphoretic layer as a function of the thickness measured by Deltascope; Right column: the thickness of sealer as a function of the thickness measured by Deltascope.

cataphoretic-layer thickness for samples 12, 14, and 16 increases as the cataphoretic-layer thickness decreases.

3.3.3 Three-layer samples

Table 3.5: MSEs of the thickness of the cataphoretic layer, sealer, and lacquer for samples 11,15, and 17.

Sample	MSE of cataphoretic layer (μm^2)	MSE of sealer (μm^2)	MSE of Lacquer (μm^2)
11	2.3	0.9	0.3
15	13.7	2.4	0.3
17	3.5	1.2	0.6

We now consider three-layer coatings (lacquer, sealer, cataphoretic layer on steel). Results of AR/MCM are shown in Fig. 3.15. Four echoes—positive, negative, positive, positive—corresponding to the air/lacquer, lacquer/sealer, sealer/cataphoretic layer, and cataphoretic layer/steel interfaces, respectively, are identified. MSEs of individual layer thick-

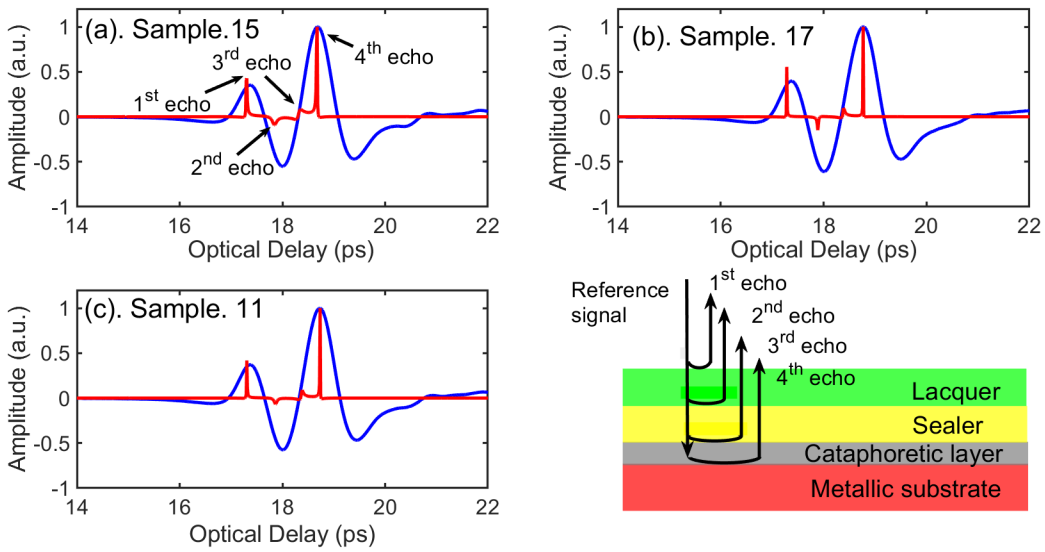

Figure 3.15: The AR/MCM result of samples (a) 15, (b) 17, and (c) 11.

nesses obtained using the Deltascope and AR/MCM for samples 11, 15, and 17 are given in Table 3.5, while Fig. 3.16 plots the AR/MCM values versus the Deltascope measurements. For the sealer and lacquer, due to their relatively large thicknesses, AR/MCM provides thickness values close to the Deltascope measurements, as the echoes are temporally well separated and distinguishable from the echoes reflected from the cataphoretic layer (thin layer). For the cataphoretic layer, again, the greatest deviations between the Deltascope measurements and AR/MCM occur for the thinnest layers.

In summary, THz TOF tomography combined with AR/MCM stratigraphic reconstruction was employed to analyze the thickness of individual layers in multilayer coatings on steel in a nondestructive and noncontact fashion. The calculated thickness of each individual layer based on the THz-based approach shows a good agreement with eddy-current-based measurements, though deviations are observed when layer thicknesses are $\lesssim 10\ \mu m$. Moreover, AR/MCM is a relatively robust analysis technique, that does not require extensive training, unlike model-based approaches, does not require a specific physical model to carry our accurate reconstruction.

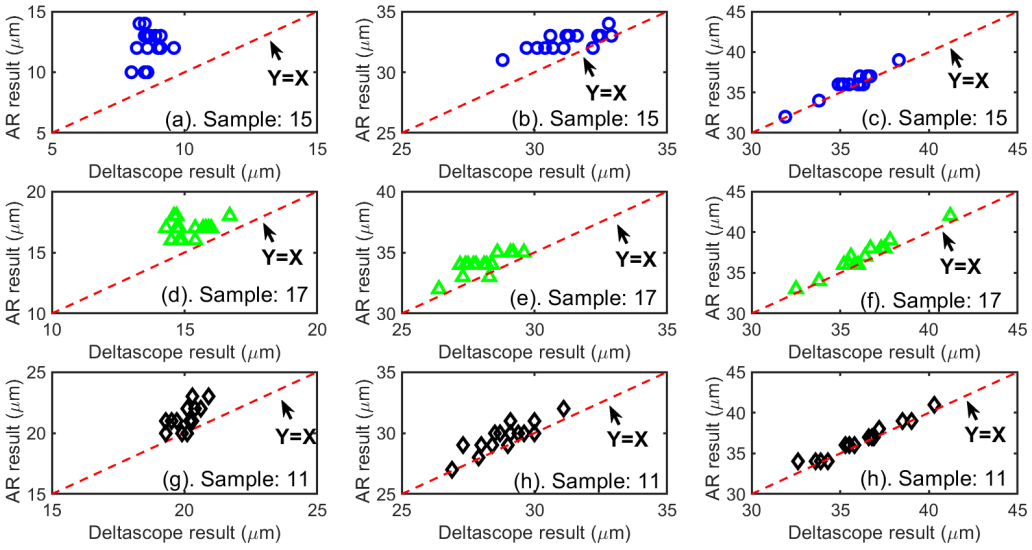

Figure 3.16: Comparison of the thickness of individual layers for samples 11, 15, and 17 between AR/MCM and Deltascope. Left column: the thickness of cataphoretic layer as a function of the thickness measured by Deltascope for samples 11, 15, and 17; Middle column: the thickness of sealer as a function of the thickness measured by Deltascope for samples 11, 15, and 17; Right column: the thickness of lacquer as a function of the thickness measured by Deltascope for samples 11, 15, and 17.

CHAPTER 4

TERAHERTZ DECONVOLUTION FOR STRATIGRAPHY CHARACTERIZATION OF COMPLEX STRUCTURES

In this chapter, terahertz (THz) transmission and reflection experiments were conducted for the non-destructive evaluation of specimens with complex, layered structures. Unlike echoes reflected from optically thin layers that are assumed to be time-shifted amplitude-scaled replicas of the THz reference signal, the echoes reflected from thick multilayered samples can be both sparse and time-varying to the frequency-dependent attenuation and dispersion during the propagation of THz waves in materials. The temporal pulse spreading increases the difficulty in accurately obtaining parameters of reflected echoes and degrades the performances of commonly used deconvolution algorithms based on a time-invariant system.

In the first section, polycarbonate (PC) and poly-methyl methacrylate (PMMA) sheets with different thicknesses are characterized non-destructively by THz time-of-flight tomography in reflection and transmission. Due to THz attenuation and dispersion observed in transmission results, features in temporal reflected signals with structure deep in the sample (*i.e.,* the back interface), might be difficult to be identified easily. Two signal processing techniques, *namely* FWDD and cross-correlation (CC), are employed. We show that straightforward analysis techniques that neglect dispersion are limited to measuring layer thicknesses in these materials of less than $\sim$17 mm, while accounting for dispersion results with a factor-of-two improvement, allowing us to measure samples as thick as $\sim$ 36 mm.

In the second section, complex, layered structures containing both micron-scale and millimeter-scale layers are characterized sparsely using one type of the second-order sparse deconvolution technique based on the interior-point method. One simple but effective propagation model for describing the temporal pulse spreading is also incorporated to enhance

the performance of the SD algorithm in processing time-varying pulses during the propagation of THz waves in materials. Numerical simulations and experimental measurements verify that the proposed algorithm can be an effective tool for stratigraphic reconstruction of moderately thick samples incorporating thin layers.

In the third section, the practical applications of THz time-of-flight (TOF) tomography for addressing several routine tasks related to automated paper handling of unsorted legacy documents, *i.e.*, ascertaining the page count of unconsolidated paper stacks, as well as detecting stapled documents buried in multipage legacy documents, are discussed in detail.

4.1 Pulsed terahertz imaging for thickness characterization of plastic sheets

Six solid PC and PMMA plastic sheets, nominally of thickness d = 2, 4, 6, 8, 10, 12 mm for each plastic, were studied in this section. The relevant physical, optical and mechanical properties for measured PC and PMMA plastic sheets are shown in Table 4.1. The top and bottom surfaces are diamond polished and shaped so as to provide visually smooth surfaces. THz scattering at the surfaces is expected to drop significantly after polishing.

Table 4.1: The physical, optical, and mechanical properties of the PC and PMMA plastic sheets studied.

Properties	Test Method	PC	PMMA
Density	ISO 1183	1.2 g/cm^3	1.19 g/cm^3
Water absorption (in water for 24h at 23 °C)	ISO 62-1	0.35%	0.3%
Refractive index	ISO-489	1.586	1.49
Vicat softening point	ISO 306	106 °C	148 °C
Tensile strength	ISO 527-2	60 MPa	65 MPa
Elongation at break	ISO 527-2	6%	4%

Our aim is to measure the thickness d of relatively thick samples using THz time-of-flight technique (TOFT). To do so, we implement a two-step procedure. In the first step, we characterize the optical constants $\alpha(\nu)$ and $n(\nu)$. This is studied based on the THz propagation in transmission geometry. Once $\alpha(\nu)$ and $n(\nu)$ are known, we carry out THz TOFT in reflection to measure sample thickness d.

The dielectric function of a material is determined in transmission by measuring a reference pulse $E_r(t)$ propagating through an empty spectrometer and a sample pulse $E_s(t)$ propagating through the spectrometer with a sample of thickness *d* placed in the beam path at the normal incidence [73]. We are most interested in the THz pulse propagation within the plastic sheet itself; however, we also need to describe what happens when the propagating pulse encounters either the top air/plastic or the bottom plastic/air interface. The relative amplitude of the signal reflected or transmitted at an interface compared with the amplitude of the reference signal is determined by the reflection and transmission coefficients $r(\nu)$ and $t(\nu)$,

$$\begin{aligned} r_{inc/trans}(\nu) &= \frac{1 - n_{rel(\nu)}}{1 - n_{rel(\nu)}} \\ t_{inc/trans}(\nu) &= \frac{2}{1 + n_{rel(\nu)}} \end{aligned} \tag{4.1}$$

where $n_{rel}(\nu)$=$n_{inc}(\nu)$/$n_{trans}(\nu)$ is the frequency-dependent ratio of the refractive index on the side of incidence to that on the side of transmission.

We define $A_r(\nu)$ and $A_s(\nu)$ as the amplitude of Fourier transform of $E_r(t)$ and $E_s(t)$, and $\phi_r(\nu)$ and $\phi_s(\nu)$ as the phase of Fourier transform of $E_r(t)$ and $E_s(t)$, respectively. The relative phase change $\phi_r(\nu)$–$\phi_s(\nu)$ of the ν frequency component of the signal transmitted through the sample, is used to calculate the refractive index $n(\nu)$ of a plastic of thickness *d*,

$$n(\nu) = 1 + \frac{c}{2\pi\nu d}[\phi_r(\nu) - \phi_s(\nu)] \tag{4.2}$$

(We neglect any dispersion in the Fresnel coefficients.) The ratio $A_s(\nu)/A_r(\nu)$ of the amplitudes can be used to calculate the absorption coefficient through the Beer-Lambert law

$$A_s(\nu)^2 = A_r(\nu)^2 \exp(-\alpha(\nu)d) \tag{4.3}$$

giving

$$\alpha(\nu) = -\frac{2}{d} \ln \frac{A(\nu)}{A_0(\nu)} \frac{[n(\nu+1)]^2}{4n(\nu)} \tag{4.4}$$

where the factor

$$t_{air/plastic}(\nu)t_{plastic/air}(\nu) = \frac{[n(\nu)+1]^2}{4n(\nu)} \tag{4.5}$$

accounts for transmission coefficients t at the front air/plastic and back plastic/air interfaces (n_{air} = 1) [74]. While there may also be a scattering contribution to the apparent reflection and transmission coefficients at the interfaces, we have verified that any such effects are sample (and position) independent. From the point of view of the analysis, that is all that is important, since the analysis ultimately eliminates the effects of surface reflections/scattering.

Due to the roughly single-cycle nature of the THz pulse, the pulse bandwidth extends from $\sim$ 60 GHz to 3 THz. In the high-frequency range, the spectrum is characterized by a gradual roll-off, until the signal level approaches the noise floor of the THz system. The noise floor is relatively frequency-independent and corresponds to the spectrum recorded by blocking the THz beam path completely. The origin of the noise is predominantly electronic.

Apodization functions, which smoothly bring a sampled signal down to zero at the edges of the sampled region, are employed to suppress leakage sidelobes produced as an artefact of the discrete Fourier transform. However, this suppression is at the expense of broadening the waveform, resulting in the decrease of the spectral resolution of the THz system [75]. Many apodization functions have been reported and discussed in the literature [76, 77, 78, 79]. Of those explored, boxcar apodization functions appear to be the best to resolve peaks, but produce more ripple artifacts in the spectrum; Happ-Genzel and triangle functions perform poorly with regard to resolving peaks and peak height, although ripples are significantly reduced. Balancing the noise level against the spectral resolution, we choose apodization functions of the Blackman-Harris 3-term form, a generalization of the Hamming family; more details can be found in Ref. [80].

After carrying out transmission studies to determine $\alpha(\nu)$ and $n(\nu)$, we conducted THz TOFT in reflection at almost normal incidence. The aim is to identify the echo originating

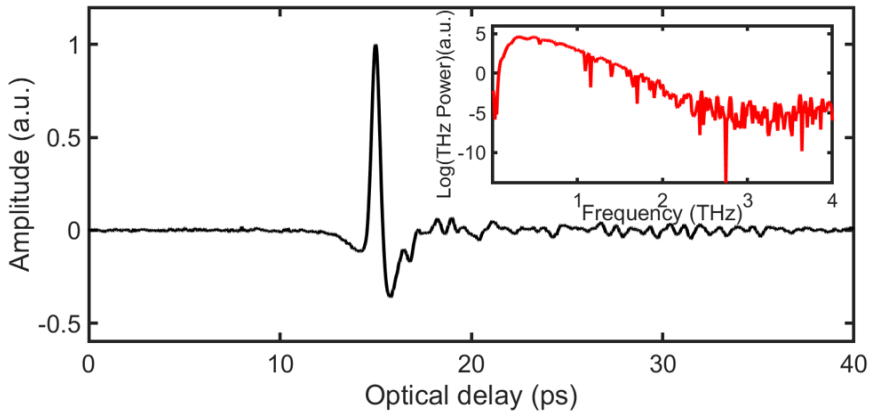

Figure 4.1: THz reference signal (pulse produced by the apparatus) with its power spectrum in the inset. The duration and dynamic range of THz pulse are $\sim$2 ps and $>$ 60 dB, while the corresponding spectrum extends from $\sim$100 GHz to 3 THz before falling below the noise floor.

in the reflection from the back plastic/air interface. The time delay between the echoes from the top air/plastic interface and the bottom plastic/air interface together with a knowledge of $n(\nu)$ the plastic provides a measure of the sample thickness d. In reflection, the time-dependent electric field of the THz reference signal $E_r(t)$, produced by the apparatus, was recorded by reflecting the incident signal from a steel plate (an excellent THz reflector), as shown in 4.1. Note that the sampling period in the measurement is set to T_s = 0.0116 ps, and each recorded temporal THz signal $E_s(t)$ reflected from the sample contains 4096 sampled data points, and these signals are averaged over 10 shots per pixel at a given time delay. Each plastic sample was raster-scanned by a set of motorized stages moving in the x- and y-directions in 0.2 mm steps over 10 mm $\times$ 10 mm regions, corresponding to 50 $\times$ 50 pixels to verify the uniformity of our measurements and analysis. The effect of THz absorption due to atmospheric water vapor was suppressed by carrying out the experiments in dry N_2. More detailed descriptions can be found in Ref. [81]. Of course, this is complicated by attenuation—the thicker the sample, the weaker the back reflection—and by dispersion, which causes the back reflection both to spread and reduce in amplitude. In order to identify the second echo, we apply two techniques: FWDD and CC between the reference pulse and the reflected signal modified to account for dispersion.

4.1.1 Optical constants

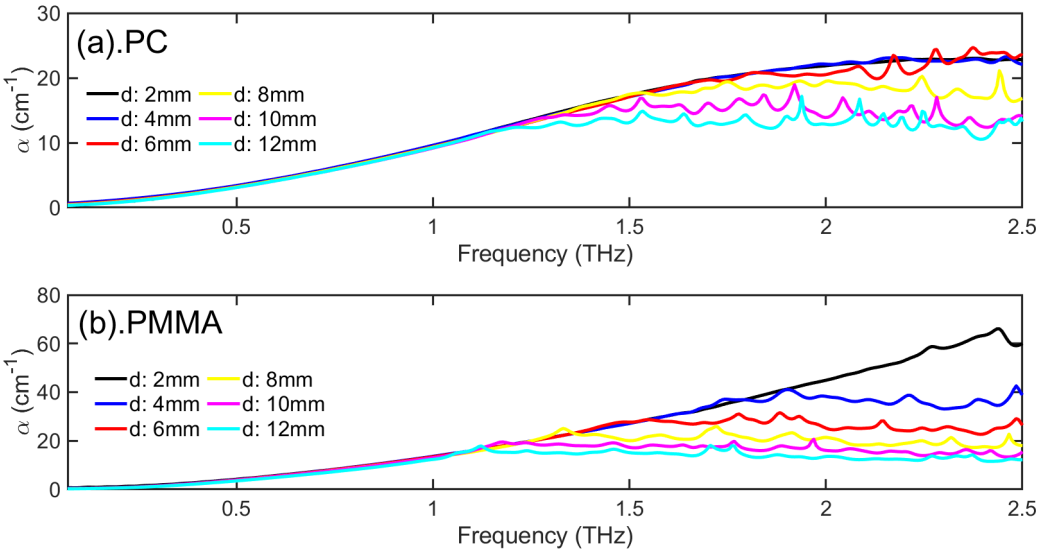

Figure 4.2: Frequency-dependent absorption coefficient $\alpha(\nu)$ for (a) PC and (b) PMMA. The different level of the reflected signal with respect to the noise floor for samples with different d is responsible for the frequency at which $\alpha(\nu)$ appears to level off (and the curves diverge). The absorption is described by the universal dielectric response (power-law behaviour) as discussed in the text.

First, the optical constants of the plastic samples are determined in transmission as described above. The absorption spectra for PC and PMMA of various d are shown in Fig. 4.2. The absorption mechanism is related to relaxation and the amorphous state of the plastics and is manifested within the spectral range lower than 3 THz [82]. Note that the curves for different d agree at lower frequencies (for $\nu < 1.2$ THz), and the absorption coefficients at the frequency of 1 THz of PC and PMMA is 9.2 cm^{-1} and 13.02 cm^{-1}, in excellent agreement with published values 11 cm^{-1} for PC and 12.5 cm^{-1} for PMMA [82, 83]. As d increases, the strength of the transmitted signal decreases due to the attenuation and thus falls below the noise floor at a frequency that decreases with increasing d. The fact that $\alpha(\nu)$ agrees for various d in each plastic where the SNR exceeds unity confirms the consistency of the approach.

The absorption coefficient and conductivity in a broad range of materials show a power-law dependence on ν as described by the universal dielectric response [84, 85, 86]. We find

that the frequency dependence of $\alpha(\nu)$ can be well fit by $\alpha(\nu) = \alpha_0 + \beta\nu^m$ where α_0 = 0.5642, β = 9.075, and m = 1.669 for PC and α_0 = 0.04057, β = 13.66, and m = 1.776 for PMMA, respectively, where ν is measured in THz and α is in units of cm^{-1}.

Frequency-dependent absorption coefficients in plastics showing behaviour reminiscent of universal dielectric response have been widely observed. In particular, results in Ref. [87] for PC are quantitatively quite close to what we observe. Some, but not all, plastics studied in Ref. [88] were observed to exhibit similar behaviour. Again, this tendency is confirmed by the results of Refs. [89] and (including PMMA) [90].

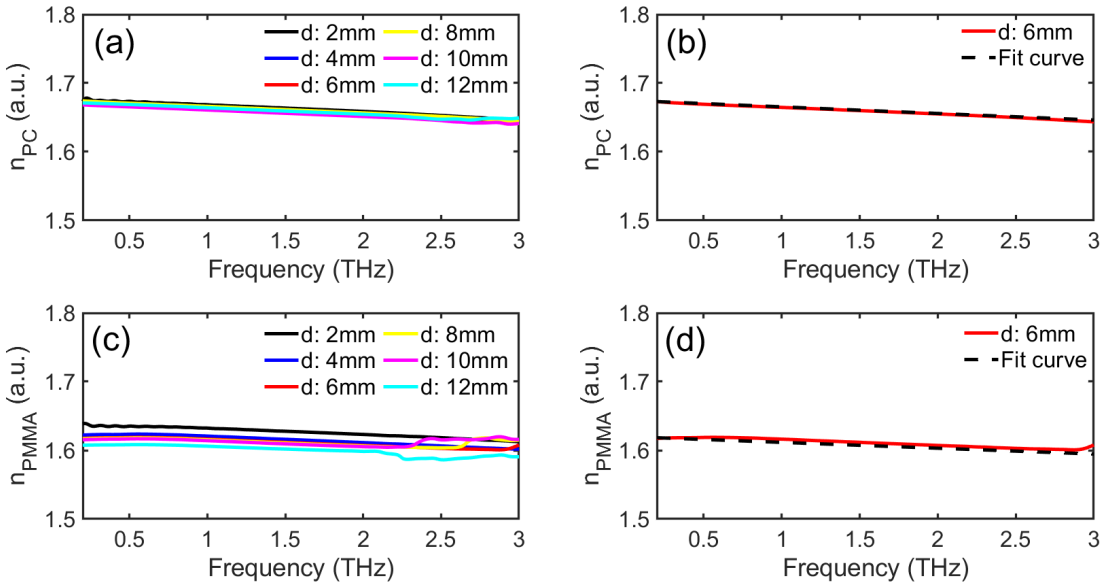

Figure 4.3: (a) Frequency-dependent refractive index $n(\nu)$ for PC; (b) Comparison between $n(\nu)$ = 1.61 - 0.0096 ν and measurement; (c) Frequency-dependent refractive index $n(\nu)$ for PMMA;(d) Comparison between data for the 6-mm thick PMMA sheet and $n(\nu)$ = 1.67 - 0.008476 ν.

The refractive index of PMMA and PC sheets of various thicknesses are shown in Fig. 4.3. Comparing results for sheets of different thickness d (but the same material), we find (as it must be) that $n(\nu)$ is is independent of sample thicknesses, as presented in Fig. 4.3 (a) and (c). Figure. 4.3 (c) shows some apparent nonlinear behaviors of $n(\nu)$, mainly at low and high frequency, likely where spectral density is low. Moreover, $n(\nu)$ for PC in frequency range 80 GHz $< \nu <$ 3 THz exhibits approximate linear behavior with a some-

what more restricted band for PMMA. Fitting the experimental results for d, the thickness for which signal to noise is highest, gives $n(\nu)$ = -0.0096ν + 1.673 for PC and $n(\nu)$ = -0.0085ν + 1.613, with ν measured in THz, as shown in inset figure in Fig. 4.3 (b) and (d), the noticeable negative dispersion in low frequency are also confirmed by published data from Fourier transform infrared spectroscopy (FTIR) measurements [91, 92]. The values 1.66 and 1.61 are the ν = 1 THz refractive indices for PC and PMMA, which are in good agreement with values of refractive index 1.651 for PC and 1.596 PMMA reported in the literature [9, 93]. First, we comment on the overall value of the refractive index, not accounting for dispersion. Ref. [87] finds n in the relevant frequency range to be 1.65 for PC in good agreement with our results. Ref. [93] finds $n \sim 1.6$ for PMMA and ~ 1.63 for PC. Ref. [90] finds for PMMA, $n \sim 1.6$.

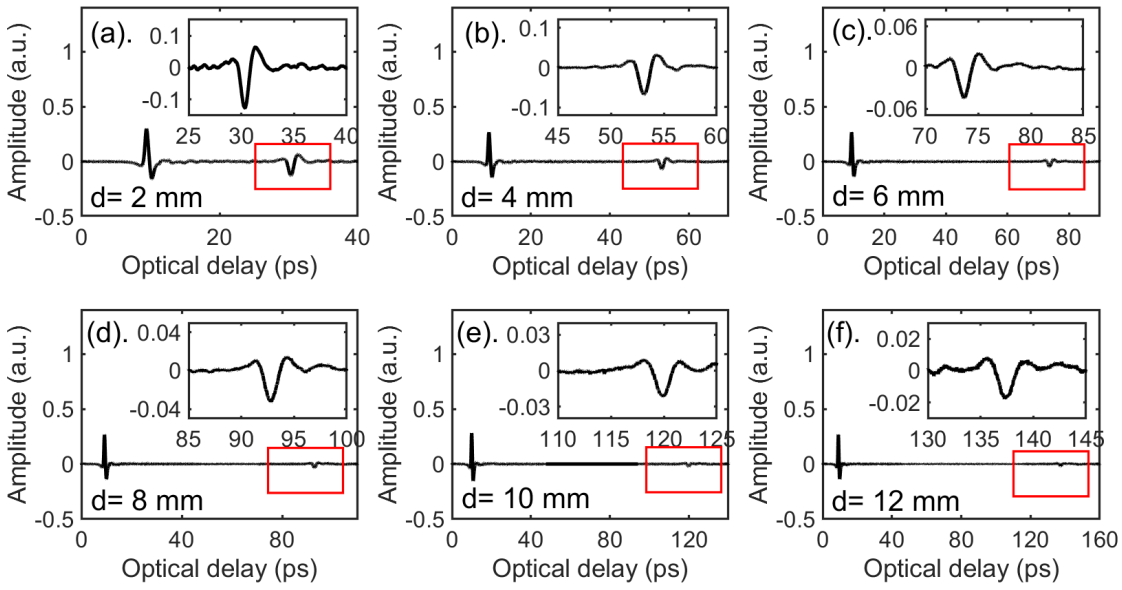

Figure 4.4: Typical measured THz signals for PC plastic sheets of various thicknesses. Insets show the THz pulse, reflected off the back plastic/air interface, on the expanded scale.

We now turn our attention to pulsed THz tomography to measure the thickness d of the PMMA and PC sheets. Typical reflected THz signals for PC and PMMA sheets with various d are shown in Fig. 4.4 and Fig. 4.5. We observe that the reflected signal contains two echoes, the first from the air/top plastic interface, the second from the bottom plas-

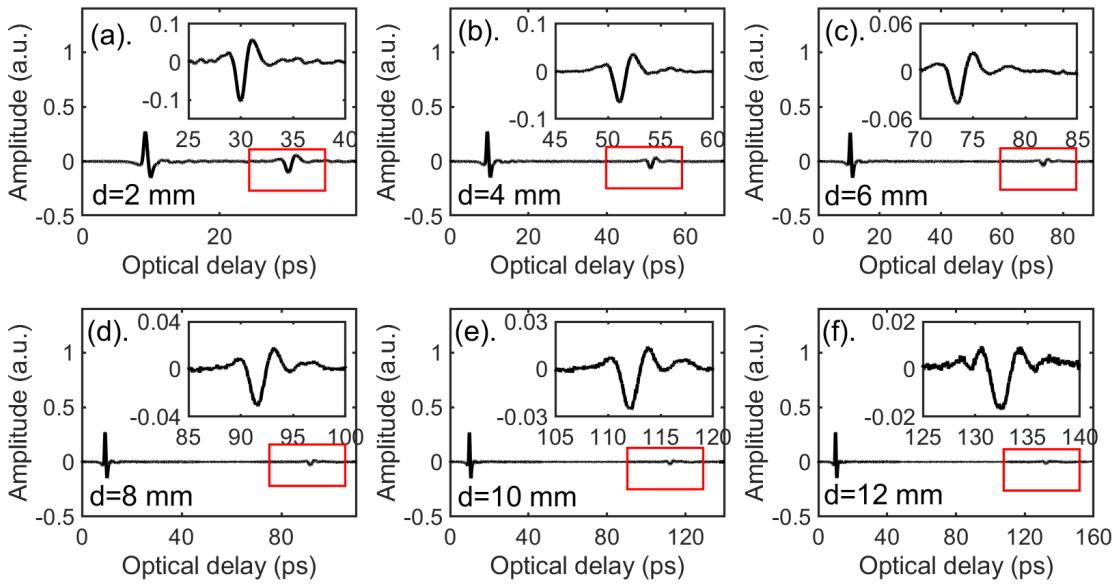

Figure 4.5: Typical measured THz signals for PMMA plastic sheets of various thicknesses. Insets show the THz pulse, reflected off the back plastic/air interface, on the expanded scale.

tic/air interface. The second echo, compared with the first one, has an opposite sign due to the reflection from a high- to low-index medium (Multiple reflections are very weak and occur at larger time delays). Apart from any scatterings that happened at the air/top plastic interface, the amplitude of the first echo with respect to $E_r(t)$ is determined by the relevant Fresnel coefficient, whereas the amplitude of the second peak is additionally affected by dispersion, the attenuation coefficient, and the Fresnel coefficient of the plastic/air interface. The plastic-sheet thickness d is calculated as the product of the refractive index and the difference in optical delay between two echoes. Of course, dispersion complicates the precise determination of the time delay for the second echo. Below, we discuss the mechanism of dispersion during the propagation.

Though dispersion in the frequency range of interest has been found weak by a number of investigators, the influence of dispersion becomes important when the samples are sufficiently thick, as in our study. The tendency for the dispersive term to be an overall negative for these plastics is not universally observed. Ref. [87] appears to show weak positive dispersion for PC and a range of other plastics. Negative dispersion at somewhat

higher frequencies is seen in Ref. [90] for PMMA and PC. A range of plastics (not including PMMA or PC) show weak negative dispersion in Ref. [94]. Though Ref. [95] finds positive and negative dispersion for various common plastics (again not including PMMA or PC), PMMA and various other plastics are found to have a negative dispersion in Ref. [93]. Ref. [96] shows considerable scatter in their frequency-dependent refractive index data and we, therefore, deem it not reliable to ascertain the sign of the dispersion. The lack of detailed agreement between the results of various authors may also have to do with the rather generic nature of the terms PC and PMMA. The materials investigated in the studies may have been fabricated by different methods, with different chemical compositions, and with different surface treatments, any or all of which may lead to different optical constants.

In light of the various results reported in the literature, we comment on the approach above and then present a test of the obtained results. The frequency-dependent refractive index $n(\nu)$ was found above directly from the transfer function. The approach is both conceptually and experimentally straightforward and involves relatively little in the line of sophisticated interpretation. Still, we confirm the dispersive effects we found in the frequency domain by analyzing the temporal pulse shape upon propagation through the plastic in reflection. As we see, this provides a confirmation of the values for $|n_1|$ given above, but not the sign of the dispersive term.

We now describe a simple time-domain model accounting for the effects of dispersion to the lowest order. Instead of the actual temporal shape of $E_r(t)$, we assume a broadband temporal Gaussian reference THz pulse,

$$E_r(t,0) = e^{-\pi {\nu_0}^2 t^2} \tag{4.6}$$

where ν_0 is a measure of its bandwidth. Note that this model pulse's bandwidth is centered at ν = 0, whereas the pulse spectrum of the reference signal in Fig. 4.1 lacks spectral content below $\sim$ 100 GHz. We expect that pulse spreading will not depend too critically on

the pulse shape so long as it covers the relevant spectral bandwidth. After Fourier transformation, the electric field of the THz pulse in the frequency domain, after propagating over a distance d, can be expressed as

$$A_s(\nu, d) = A_s(\nu, 0)e^{-\alpha(\nu)d/2}e^{-in(\nu)k(\nu)z} \tag{4.7}$$

The absorption coefficient $\alpha(\nu)$ originates in the real part of the exponent that only controls the amplitude of the reflected signal. We include only the lowest-order dispersion term (second-order) in $n(\nu)$, *i.e.* $n(\nu) = n_0 + n_1\nu$. In addition, for the application of this pulse-propagation model, we neglect the dispersion in the absorption coefficient within the pulse bandwidth. After taking the inverse Fourier transform, the THz pulse in the time domain is

$$\begin{aligned} A_s(t, d) &= \int_{-\infty}^{\infty} d\nu A_s(\nu; z)e^{2\pi\nu t} \\ &= e^{-\frac{\alpha d}{2}} \int_{-\infty}^{\infty} d\nu A_s(\nu, 0)e^{-2\pi i n_1 \nu^2 d/c}e^{2\pi i\nu\widetilde{t}} \end{aligned} \tag{4.8}$$

where $\widetilde{t} = t - n_0 d/c$ includes the propagation delay. Thus,

$$\begin{aligned} A_s(t, d) &= \nu^{-1}e^{-\alpha d/2} \int_{-\infty}^{\infty} d\nu e^{-pi\nu^2/{\nu_0}^2}e^{-2\pi i n_1 \nu^2 d/c}e^{2\pi i\nu\widetilde{t}} \\ &= {\nu_0}^{-1}e^{-\alpha d/2}\sqrt{\frac{\pi}{p}}e^{-p} \end{aligned} \tag{4.9}$$

with $p = \pi({\nu_0}^{-2} + 2in_1 d/c)$

From Eq. (4.9), the temporal pulse width is determined by

$$\nu_0^{-1}[1 - (\frac{2n_1 d\nu_0^2}{c})^2]^{-1/2} \approx \nu_0^{-1}[1 + (\frac{2n_1 d\nu_0^2}{c})^2] \tag{4.10}$$

with respect to the incident pulse amplitude, the amplitude of the pulse is attenuated as

$$[1 - (\frac{n_1 d\nu_0^2}{c})^2]e^{-\alpha d} \approx e^{-\alpha d} \tag{4.11}$$

here, α is a representative value of the absorption coefficient within the pulse bandwidth. This gives us a rough way to find the dispersion $|n_1|$, based on the temporal shape of the THz pulse following propagation through the plastic sheet. For PC we find $|n_1|$ = 0.0093, and for PMMA $|n_1|$ = 0.0086, respectively. Note that the modification to the pulse shape for the Gaussian depends only on ${n_1}^2$; therefore, we can only determine $|n_1|$ by these means. Nevertheless, the model result is in surprisingly good agreement with the rigorous value obtained in the frequency domain, as shown in Fig. 4.6. Due to the THz pulse shape, the spectral density at low frequency is greater than at high frequency, and the power falls off to the noise floor. This enables us to estimate the noise floor from the measured signal the THz beam path has blocked. The second echo for PC and PMMA is reduced in amplitude

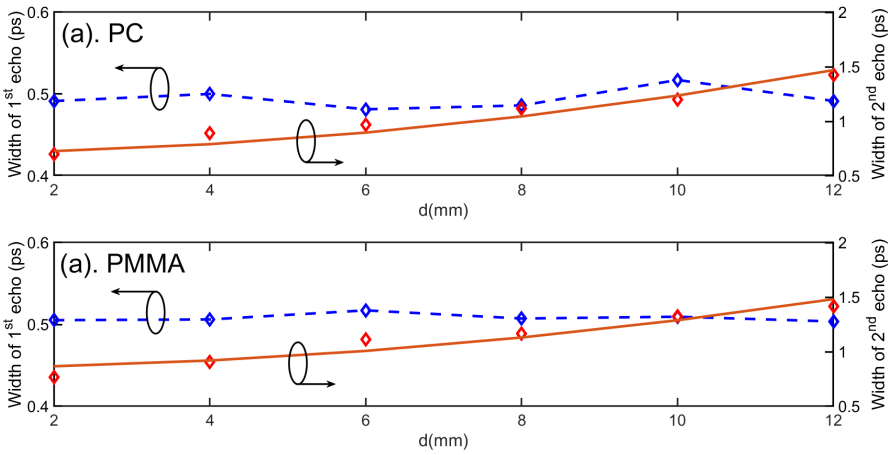

Figure 4.6: Plastic-sheet thickness-dependence of width of the first pulse and the second pulse for (a) PC and (b) PMMA.

with increased d, as shown in Fig. 4.7, both due to attenuation and pulse spreading caused by dispersion [97]. These effects can be distinguished because dispersion also causes the pulse to spread and to become reduced in peak height. Based on the Cauchy formula [98], the width of the reflected signal displays an excellent fit to the model $A + Bd^2$. We find, for PC, A = 0.706, B = 0.0053, and for PMMA, A = 0.721, B = 0.0078, enabling us to estimate n_1 as 0.009 for PC and 0.008 for PMMA. These values for n_1 agree well with the slope of the frequency-dependent refractive index obtained from the frequency-domain

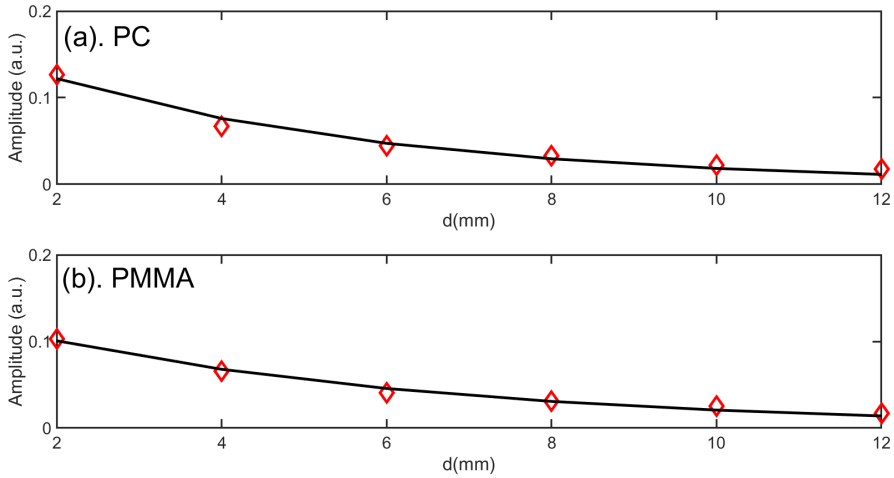

Figure 4.7: Amplitude of the second echo in the reflected THz signal for all (a) PC and (b) PMMA sheets.

analysis of the transmission data. Note as we did in the section, however, that this mode does not determine the sign of n_1.

4.1.2 Thickness estimation

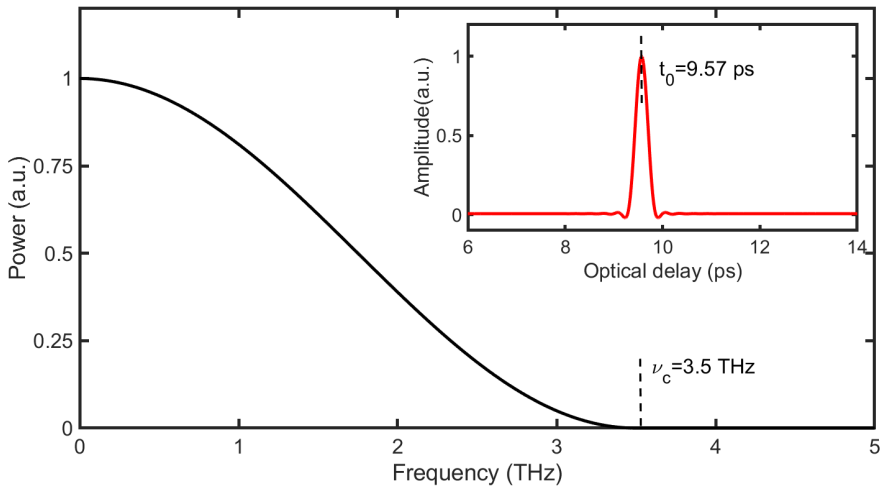

Figure 4.8: The Hanning window function with typical values, t_0 = 9.57 ps and ν_c = 3.5 THz and with inverse Fourier transform in the inset.

Characterization of $n(\nu)$, beyond its intrinsic interest, is of importance in using pulsed THz tomography to measure the thickness of thick samples where the reflection from the back interface may be very weak. But, before we see how this information can be applied

to this problem, we employ FWDD for thickness determination to provide a benchmark. FWDD can assist in suppressing the effects of high- and low-frequency noises and to better distinguish weak features (*i.e.* echoes) in the reflected signal. In this study, Hanning filters are selected, serving as the frequency-domain filters, with transfer function $F(\nu)$ given by

$$F(\nu) = \begin{cases} e^{i2\pi\nu t_0}\cos^2(\frac{\pi\nu}{2\nu_c}) & |\nu| \leq \nu_c \\ 0 & |\nu| > \nu_c \end{cases} \tag{4.12}$$

where t_0 corresponds to the arrival time of the main peak in the time-domain and ν_c is the cutoff frequency. The transfer function for the filter is manipulated by optimizing the cutoff frequency ν_c. The spectrum of the Hanning window function applied in this work is shown in Fig. 4.8. In the wavelet denoising procedure, *symlet* (sym4) wavelets are selected with level 8 for the wavelet decomposition. More details can be found in Ref. [26]. The reconstructed impulse response function for PC and PMMA samples is shown in Fig. 4.9 and Fig. 4.10. Due to the elimination of anomalous spikes in low- and high-frequency regions, the frequency components within the band [0 THz, 3.5 THz] are retained. Consequently, the SNR of the reconstructed signal is significantly improved, and two pulses corresponding to the air/plastic and plastic/air interfaces can be detected clearly for both plastic sheets. While focusing attention on the second pulse of reflected THz signals for various PC and PMMA sheets, broadening of this second reflection from the back interface is evident due to the collective effect of narrowing the bandwidth with the frequency-domain filter as well as the dispersion effect, together with the low SNR of second echo resulting from obvious fluctuations corresponding to the low-frequency residual noises, making it increasingly difficult to precisely identify the time delay of the second echo as sample thickness increases.

FWDD, which decomposes the received signal $E_s(t)$ into wavelets that match the features of the received signal best, is not easily adapted to account for dispersion because of the complexity of employing the dispersion model into wavelets. Instead, we consider the

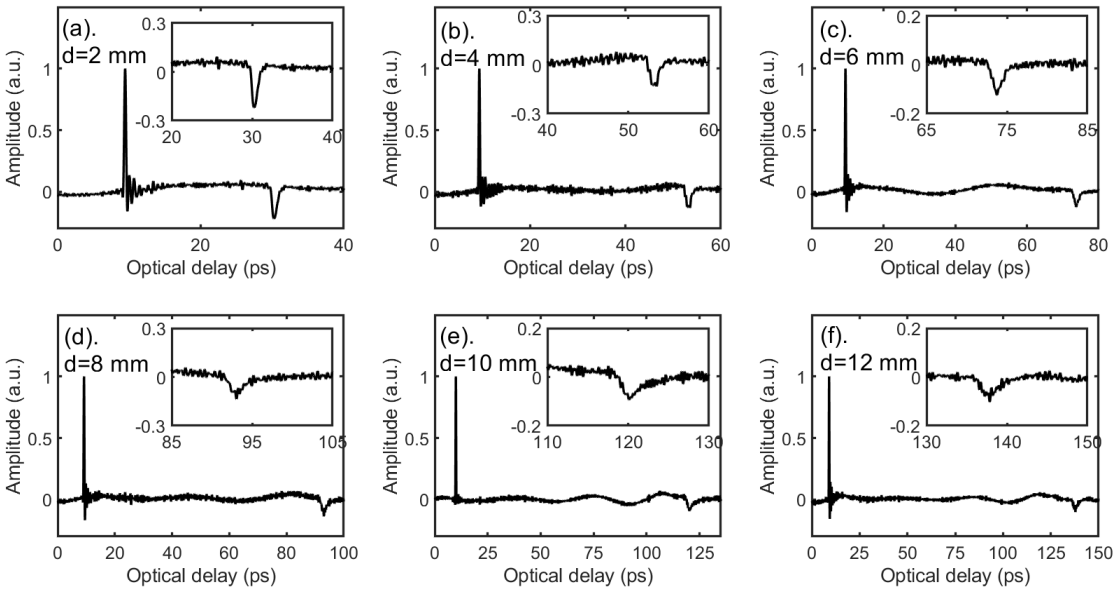

Figure 4.9: FWDD results for the reconstructed impulse response function $h(t)$ for all PC samples.

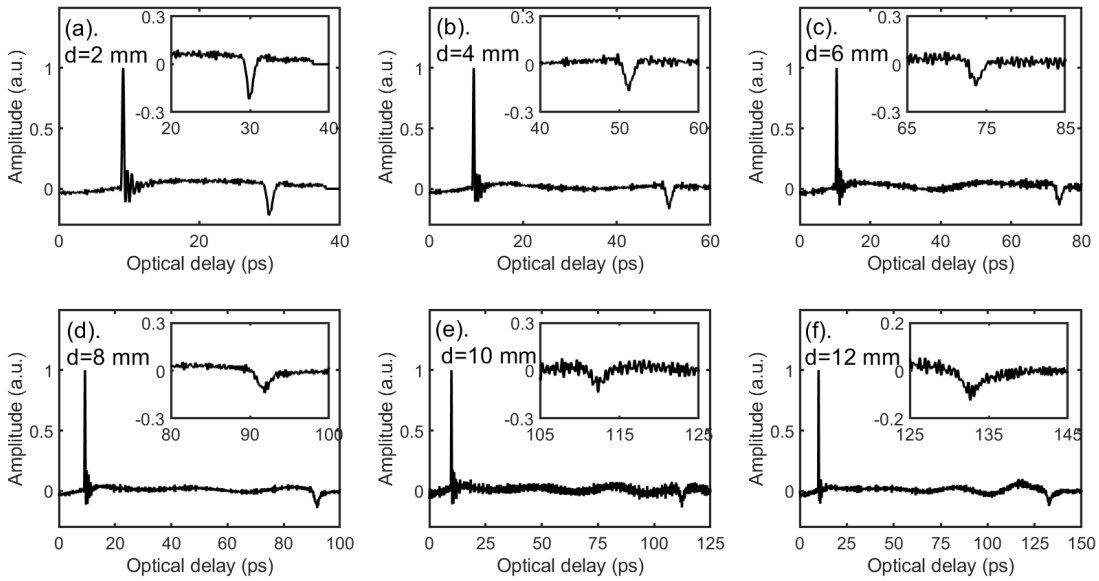

Figure 4.10: FWDD results for the reconstructed impulse response function $h(t)$ for all PMMA samples.

cross-correlation (CC) between the detected reflected signal $E_s(t)$ and the reference pulse $E_r(t)$ suitably modified to account for dispersion. In essence, CC quantifies the degree of linear similarity between the reference and the reflected signal at various time delays [99]. Pulses in $h(t)$ recovered from FWDD are much wider than the ideal impulses because of

the dispersion as well as the narrowness of the bandwidth by frequency-domain filtering, and consequently limits the depth resolution of FWDD. CC, however, provides an intuitively simple way to account for dispersion. It only determines the time delay between the reference and reflected signals. After calculating the CC between two signals, the maximum (or the minimum if the signals are negatively correlated) of the CC function indicates the point in time where the signals are best aligned; Furthermore, these techniques are also powerful for conditions with low SNR where the reflected signal is weak. The CC between the reflected signal $E_s(t)$ and the reference signal $E_r(t)$ can be expressed as

$$\omega(t) = E_s(t) \otimes E_r(t) \triangleq \int_{-\infty}^{\infty} E_s^*(\tau) E_r(t+\tau) d\tau \tag{4.13}$$

In practice, we should consider the discrete form of Eq. (4.13), which is

$$\omega[n] = \sum_{m=1}^{N} E_s[m] E_r[m+n] \tag{4.14}$$

where N the number of data points [100, 101].

In order to enhance the depth resolution, balancing the efficiency and complexity, a linear time-invariant (LTI) system was designed [102] to simulate the effect of pulse-spreading [28]. The temporal spreading was assumed caused by the propagating THz pulse travelling a distance Δz in an attenuative/dispersive medium. Hence, the reference THz pulse $h_{\Delta z}(t)$ can be expressed as

$$h_{\Delta z}(t) = \rho_{\Delta z}(t) \otimes h_0(t) \tag{4.15}$$

where $h_0(t)$ is the THz signal at Δz = 0, corresponding to the reference THz signal, and $\rho_{\Delta z}(t)$ is the impulse response function of plastic samples.

A quasi-Dirac function was used to simulate the impulse-response function is $\rho_{\Delta z}(t)$, which is of the form

$$\rho_{\Delta z}[n] = \begin{cases} a & n = 0 \\ 1 - 2a & n = 1 \\ a & n = 2 \\ 0 & otherwise \end{cases} \tag{4.16}$$

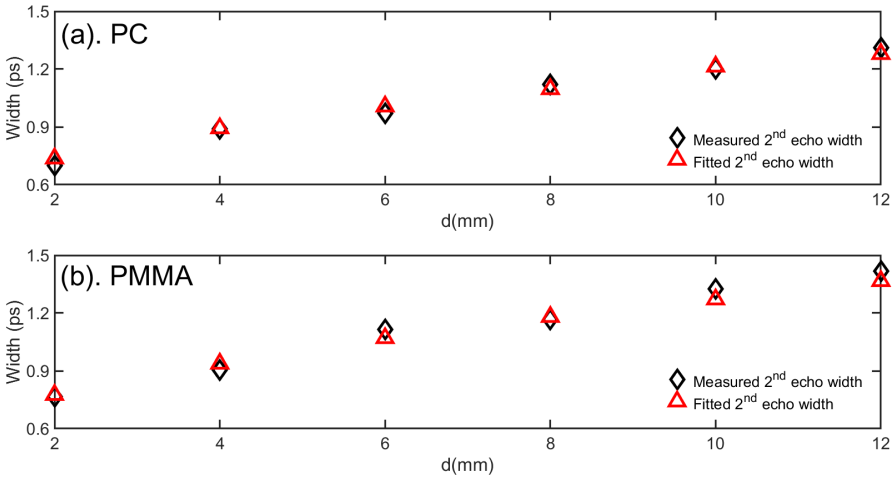

Figure 4.11: Comparison between simulated and measured width of pulse reflected off back plastic/air interface for (a) PC and (b) PMMA samples.

where the parameter a determines the degree of pulse-spreading, and its range should be $0 < a < 1/2$. Note that when a = 0, $\rho_{\Delta z}[n] = \delta[n-1]$, indicating that it only displays a simple time delay of one sampling period without pulse-spreading. The criterion for the fitting parameter a is based on the mean square error (MSE) between the width of the convolved signal $\rho_{\Delta z}(t) \otimes h_0(t)$ and the width of the raw measured signal at 2, 4, 6, 8, 10, and 12 mm. The comparison between the simulated and the measured width of the second pulse for PC and PMMA samples is shown in Fig. 4.11. The optimal value for parameter a in this model for PC is determined to be 0.23 and, for PMMA, it is 0.28. For thicker samples ($d > 10$ mm), the error between the simulated width and the measured width increases, which attributes to the low SNR in that region. The CC results for PC and PMMA with and without accounting for dispersion, are shown in Fig. 4.12 and 4.13. The comparison of the amplitude of the second pulse of the reflected THz signal between the FWDD result and the CC result, with and without accounting for dispersion is shown in Fig. 4.14. For both PC and PMMA, the amplitude of the CC peak of the reflected pulse from the back surface is enhanced significantly when dispersion is included as opposed to when dispersion is neglected, indicating that pulse spreading is a significant factor that degrades the ability to identify weak reflected pulses in thicker samples. Moreover, pulse spreading will also limit

the accuracy of thickness determinations in thicker samples employing analysis techniques that do not account for dispersion.

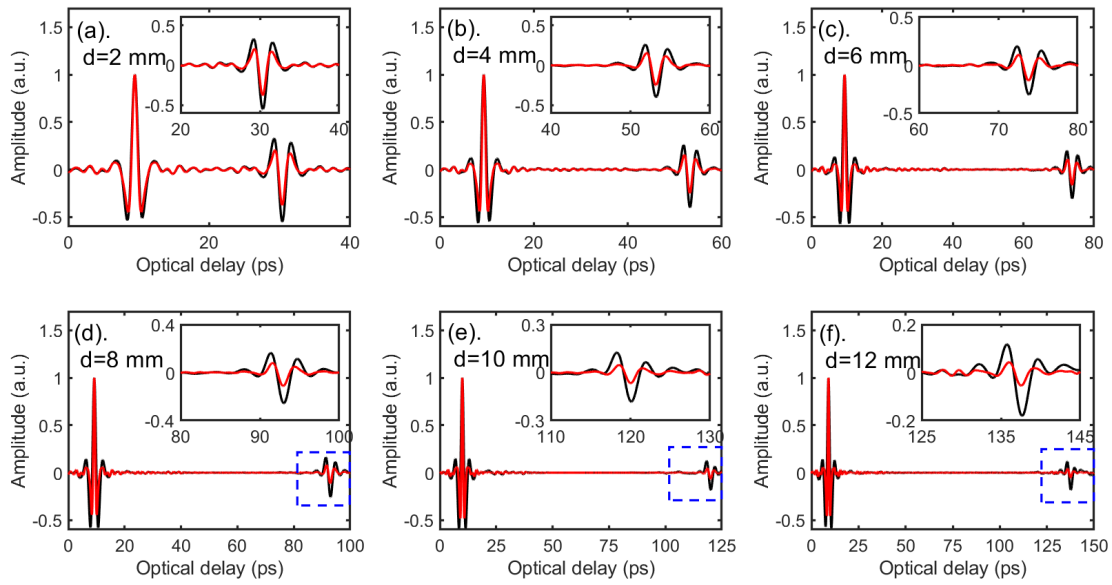

Figure 4.12: CC results for all PC samples accounting for (black) and neglecting (red) dispersion.

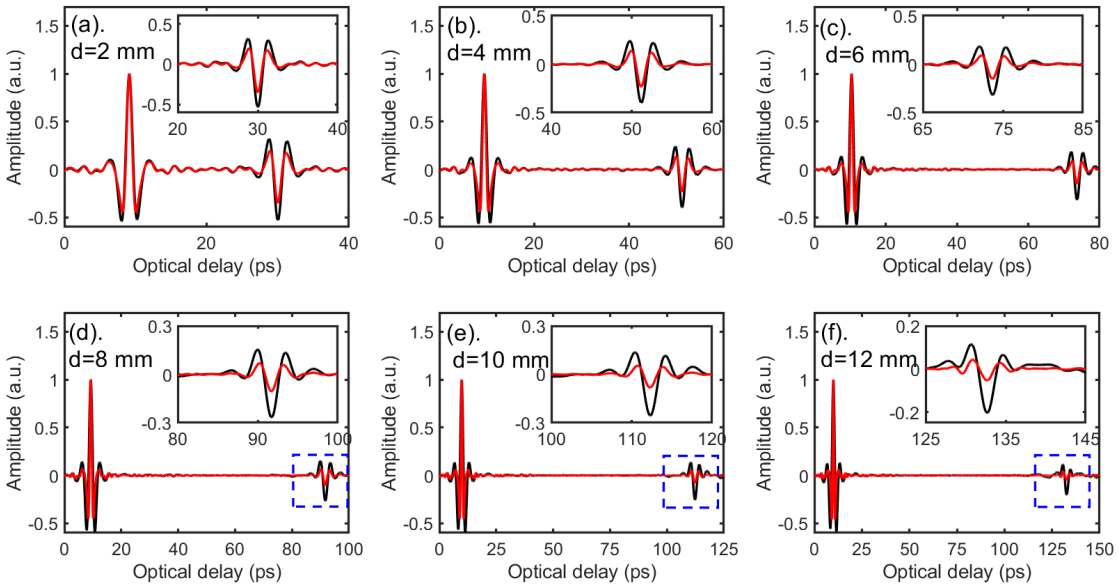

Figure 4.13: CC results for all PMMA samples accounting for (black) and neglecting (red) dispersion.

While FWDD was successful in identifying the echo from the back plastic/air interface

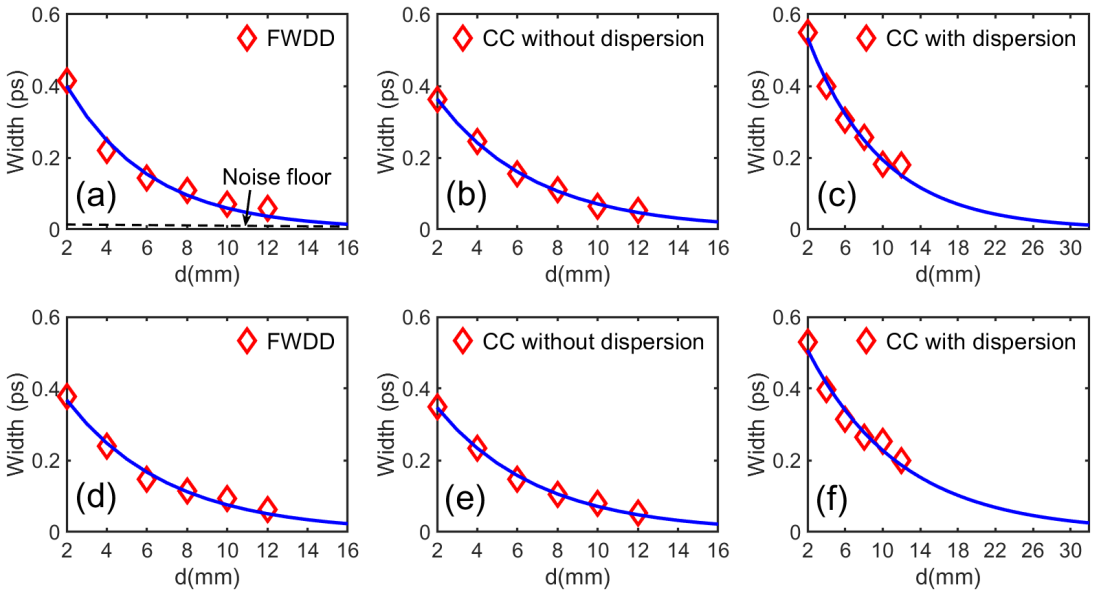

Figure 4.14: Comparison between the peak amplitude associated with the echo from the bottom plastic/air interface for PC (a)-(c) and PMMA (d)-(e).

of all studied sheets, it is clear that this approach is near its limit for the 12 mm sheets shown in Figs. 4.9 (f) and 4.10 (f); CC will thus enable sheet thickness determination for somewhat larger values of d than were available for study here. We can quantify this by extrapolating our results. The extracted FWDD and CC peak values from Fig. 4.12 and Fig. 4.13 are fit to exponentials (since the falloff is dominated by absorption). The noise floor is determined by the mean and standard deviation of the system noise and is indicated in the panels in Fig. 4.14. When the amplitude of the second echo (obtained by FWDD or CC with or without dispersion) descends to the noise floor, the signal reflected from the sample can no longer not be distinguished from system noise. The extrapolated value of d, where the peak amplitude is equal to the noise floor, defines the thickest sample for which a given analysis technique can be used to detect the echo from the bottom plastic/air interface.

In Fig 4.14 (a), (b) and (d), (e), we see that FWDD and CC without dispersion are limited to measuring PC and PMMA slabs with $d \sim 17$ mm. Accounting for dispersion, however, CC enables us to measure samples up to $d \sim 36$ mm. This is a factor of ~ 2

improvement in layer thicknesses that can be measured by pulsed THz tomography.

In conclusion, we have measured the frequency-dependent refractive index and the attenuation constant of PC and PMMA. The refractive indices are $n(\nu)$ = 1.67 - 0.0096ν for PC and $n(\nu)$ = 1.61 - 0.0085ν for PMMA, where ν is measured in THz; the absorption coefficient $\alpha(\nu)$ = 0.564 + 9.075$\nu^{1.669}$ in units of cm^{-1} for PC and $\alpha(\nu)$ = 0.0406 + 13.66$\nu^{1.776}$ for PMMA, where ν is measured in THz. These values are in reasonable agreement with those in the literature, though there is no universal agreement on the sign of dispersion. We then turned our attention to using THz TOF tomography to measure the thickness of PC and PMMA plastic sheets within sample thickness d in the range of 2–12 mm. Due to dispersion, which broadens the width of the THz reflection from the back interface of the sample, the depth resolution for FWDD is significantly degraded. We find that for thicker samples (here $d \gtrsim 8$ mm), the second echo arising from the back plastic/air interface is significantly broadened and reduced in amplitude, leading to this feature becoming hidden in the noise. We show by straightforward extrapolation that naïve analysis techniques that neglect the effects of dispersion (here FWDD and direct CC without dispersion) are limited to measuring layer thicknesses in these materials of less than $\sim$ 17 mm. Accounting for dispersion, however, results in a factor-of-two improvement, allowing us to measure samples as thick as $\sim$ 36 mm.

While our experimental study was limited to PMMA and PC sheets of maximum thickness of 12 mm, our work shows that CC will enable THz TOF tomography to measure thicknesses of a variety of plastics to values of d in the few-cm range using commercial THz systems.

4.2 Terahertz nondestructive stratigraphic analysis of complex layered structures

Although the aforementioned CC-based method used in [103] succeeds in characterizing thick PC and PMMA plastic sheets, there are still some points that deserve to be mentioned: 1). Due to the dispersion as well as attenuation as a THz signal propagates through

the material, echoes following the main pulse associated with the front air/plastic interface are reduced in amplitude and may have a low SNR for thick objects; therefore, errors may be introduced when estimating the pulse amplitude as well as the width; 2). In order to overcome the effect of noise, the calibration set must be large enough to upgrade the prediction accuracy of the quasi-Dirac δ-function model utilized to simulate dispersion; 3). The dispersion model and CC-based approach fail when echoes overlap partially or entirely; 4). Even though the CC-based approach is a robust tool that is less sensitive to background fluctuations, the obtained results are not suitable for direct post-signal-processing due to the residual noise, in particular when the SNR of the reflected THz signal is not high enough.

Even though SD based on iterative shrinkage algorithm (SD/IST) has been widely and straightforwardly implemented, many iterations are generally required to achieve high accuracy results, leading to large computation costs of the SD/IST algorithm, especially when addressing signals comprised of a large number of data points. A more detailed discussion can be found in Refs. [104, 105].

Several refined approaches have been proposed to accelerate the IST algorithm, such as the fast IST algorithm (FISTA) [104], the two-step IST algorithm (TwIST) [106], and the split augmented Lagrangian shrinkage algorithm (SALSA) [106]. In this project, an interior-point method, one type of second-order SD approach, is employed to sparsely reconstruct the impulse response function of specimens that contain both optically thick and thin layers. Compared with the IST algorithm, super-linear convergence can be guaranteed and fewer iterations are demanded to achieve convergence, even though the computational cost of each iteration is significant. Therefore, higher accuracy of the signal reconstruction can be achieved in some cases. Moreover, several approaches have been proposed to accelerate the preconditioned conjugate-gradient (PCG) process, such as rank-one approximation of the matrix multiplication $\mathbf{I}^{\top}\mathbf{I}$ [107]. Balancing the complexity and performance, an approximation of the Hessian matrix (which contains the matrix multiplication of $\mathbf{I}^{\top}\mathbf{I}$) by its diagonal elements is employed in this work; a presentation of the technique can be

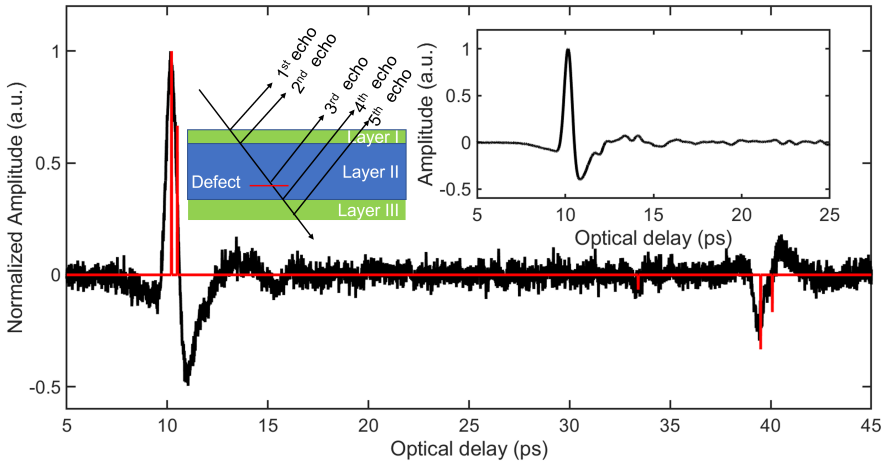

Figure 4.15: The assumed impulse response function $h_0(t)$ (red) and the simulated reflected THz signal $r(t)$ (black). The inset shows an experimentally measured reference pulse $i(t)$ produced by our apparatus. Also shown is a schematic cross-section of the simulated three-layered sample. Layers I and III (green) are Teflon of thicknesses of 30 μm and 60 μm, respectively, while layer II (blue) is silica with a thickness of $\sim$ 2230 μm. A thin air layer exists around the central region of layer II.

found in Ref. [108].

4.2.1 Numerical simulation

As mentioned above, we will show the effectiveness of SD for the characterization of a complex structure that contains both thick and thin layers. These two requirements place what appear to be conflicting demands on approaches employed in the literature to analyze THz TOFT data. To bring out key issues, numerical simulations based on synthetic data (see the schematic cross-section in Fig. 1.2) are performed first to show the problems presented by typical approaches, such as the FWDD algorithm and the CC-based approach, and then to verify the potential advantages of SD for structural characterization on complex layered structures.

Considering the THz TOFT experiment as a linear time-invariant system, the reflected signal $r(t)$ is thus the convolution of the known THz pulse $i(t)$ (reference signal) [we use a typical experimentally measured reference signal, see the inset in Fig. 4.15] and the impulse-response function $h(t)$. An ideal impulse response function $h_0(t)$ of a simple

three-layer structure, represented in Fig. 4.15, is assumed:

$$h_0[n] = \begin{cases} 0.3 & t = 11.6 \\ 0.2 & n = 11.89 \\ -0.02 & n = 34.8 \\ -0.1 & n = 40.89 \\ -0.05 & n = 41.47 \\ 0 & otherwise \end{cases} \tag{4.17}$$

where the unit of t is picoseconds; time-domain signals are discretized with the sampling period T_s = 0.0116 ps utilized later in experiments ($t = nT_s$ with n the discrete index). Nonzero values at a given time are related to the Fresnel coefficient from a given interface and determine the amplitude of the respective echoes. The time intervals (optical delays) between the 1^{st} echo and 2^{nd} echo, 2^{nd} echo and 4^{th} echo, and 4^{th} echo and 5^{th} echo are 0.29 ps, 29 ps, and 0.58 ps, respectively, corresponding to the thickness of the layer I, II, and III. Assuming that the first and third layers are Teflon and the second layer is amorphous silica, based on the corresponding averaged refractive index of Teflon and silica within the THz frequency regime, which are 1.45 [9] and 1.95 [109], respectively, the thicknesses of layers I, II, and III are 30 μm, 2230 μm, and 60 μm. In addition, a thin air layer is also presented in layer II at a time delay t = 34.8 ps. The discussion above holds in the absence of noise. In order to simulate the reflected signal $r(t)$ obtained in the actual noisy environment, additive Gaussian white noise with SNR 10 dB is included in the reflected signal $r(t)$ as shown in Fig. 4.15.

We expect five peaks (two positive peaks and three negative peaks) in $r(t)$. On account of the optical thin thicknesses of layers I and III, the echoes reflected from the front and back of these two layers overlap almost entirely. One could erroneously conclude that the sample consists solely of a single layer. Furthermore, the amplitude of the reflected echo from the small air gap is comparable to the noise background and is difficult to be distinguished directly in the raw reflected signal $r(t)$. Further signal processing is thus necessary to obtain the thickness information of layers I, II, and III, as well as to resolve the reflected echo from the small air layer drowned in noise.

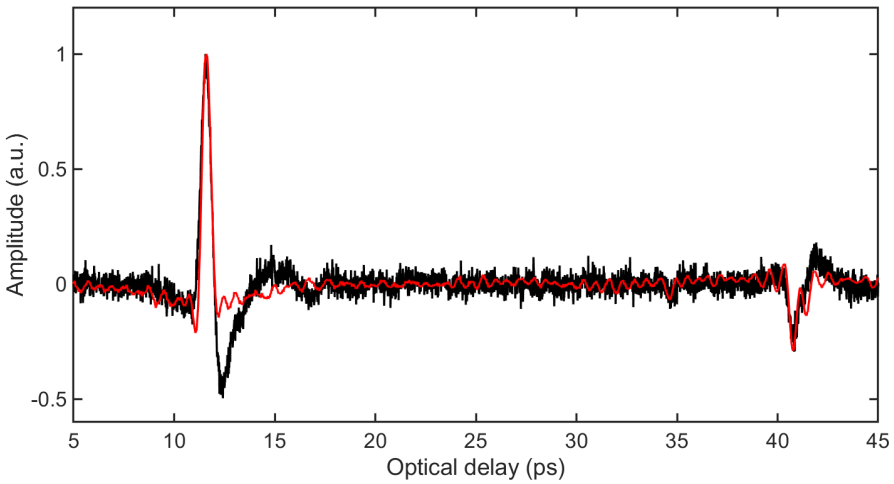

Figure 4.16: Comparison between the raw reflected signal $r(t)$ (black) and the corresponding deconvolved signal by FWDD (red) based on the synthetic data. Results are obtained with simulated data for the assumed impulse response function $h_0(t)$ of Eq. (3.3). Layer III is resolved successfully, while layer I and the air layer locations fail to be identified.

Our first attempt is solely to apply a frequency-domain windowing filter, the conventional and simplest approach to denoise experimental signals. The frequency-domain filters must be used with caution, as meaningful information can be discarded along with the noise. In order to guarantee a satisfactory SNR of the deconvolved signal, the preferred approach is a time-localized filtering approach cascaded with mild filtering of the type above. Here we use wavelet denoising due to the high similarity between the wavelet basis functions and the typical THz signal [54]. How to select the optimal wavelet base function and evaluate the decomposition level is discussed in detail in Refs. [55, 56]. For this work, balancing the denoising performance of FWDD with the SNR of the simulated reflected signal $r(t)$, Wiener filtering with noise desensitizing factor $0.2\max(|I(\nu)|^2)$, where $I(\nu)$ is the Fourier transform of the reference signal $i(t)$, is selected and the $sym4$ wavelet function with decomposition level 10 is set for wavelet decomposition. We note that the performance of the Wiener filter is largely determined by the selection of the noise desensitizing factor. Owing to the relatively low amplitude of the reflected signal from the thin air layer within layer II, a larger noise desensitizing factor will lead to the elimination of the subtle features in the reflected signal $r(t)$.

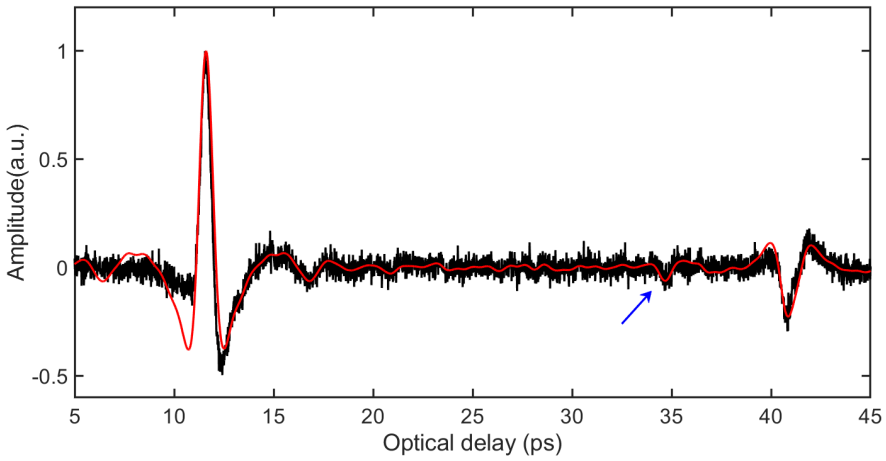

Figure 4.17: Comparison between the raw reflected signal $r(t)$ (black) and the corresponding deconvolved result by CC (red) based on synthetic data. The arrow indicates the echo from the airgap at t = 34.67 ps. Results are obtained with simulated data for the assumed impulse response function $h_0(t)$ of Eq. (4.17).

The FWDD deconvolved signal for the synthetic reflected signal $r(t)$ is displayed in Fig. 4.16. Compared with the raw reflected signal $r(t)$ (black), the SNR of the deconvolved signal is significantly enhanced. Owing to the presence of residual noise even after FWDD as well as the relatively low amplitude of the signal, the echo corresponding to the thin air layer is difficult to be identified clearly in the deconvolved result. Importantly, the thin layer III is resolved successfully, while layer I fails to be resolved. Owing to the narrow effective bandwidth of the impulse response function $h(t)$, the axial resolution of FWDD is moderate. According to the numerical simulation presented in Ref. [26], the minimum time delay reconstructed by FWDD for our setup is $\sim$ 0.35 ps when SNR = 10 dB, corresponding to a thickness for layers I and III of $\sim$ 36 μm, which is larger than the assumed optical thicknesses for layers I and III in $h_0(t)$. Moreover, the appearance of extraneous peaks as well as the pulse broadening in the impulse response function recovered by FWDD, resulting from the application of the low-pass filter, are also observed in the deconvolved result and might deteriorate the resolution in turn [29].

Because we have succeeded in identifying weak echoes from a noisy background using CC in Ref.[103], we attempt that approach next. Unlike FWDD which improves SNR

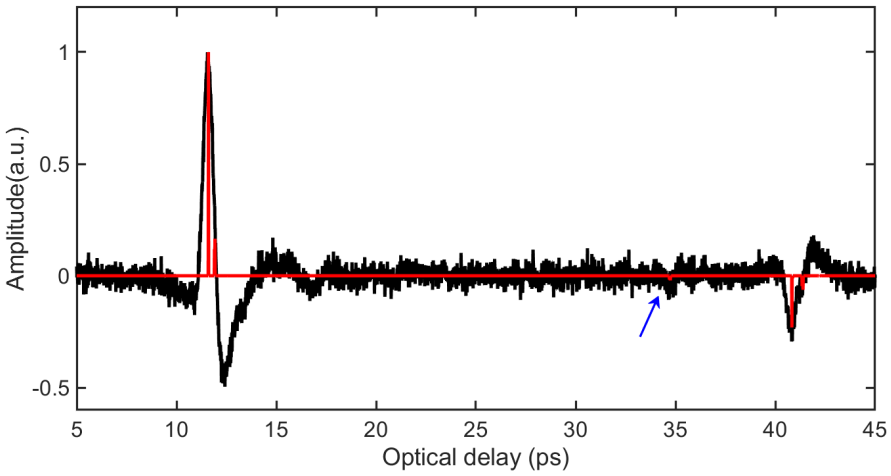

Figure 4.18: Comparison between the raw reflected signal r(t) (black) and the corresponding deconvolved result by SD (red) based on synthetic data. All interfaces are observed successfully in the deconvolved result. The blue arrow indicates the position of the echo from the airgap in layer II, which is identified in the SD reconstruction.

mainly by narrowing the bandwidth of the impulse response function $h(t)$, CC enhances SNR by reducing the noise's spectral bandwidth to that of the reference signal. Superior to FWDD, because of the absence of signal truncation, there is no risk of losing valuable information when applying CC. Therefore, in some cases, the results of CC may be more reliable than FWDD, in particular in the absence of *prior* knowledge of the structure and low SNR in the reflected signal $r(t)$. Figure 4.17 presents the comparison between $r(t)$ and $h(t)$ deconvolved by CC. The ability of CC to identify real echoes is higher than FWDD. The echo reflected from the thin air layer, as indicated by the blue arrow, is easily identified even with a small amplitude, validating the superior capability of CC to pick out weak echoes in a low-SNR environment. Because CC is less sensitive to SNR, theoretically, it can even detect signals buried below the noise floor as opposed to FWDD. However, based on the nature of CC that extracts a known signal from a reflected signal contaminated by noise, it is not designed to separate overlapped echoes associated with optically thin layers. As a result, the echoes reflected from layers I and III cannot be distinguished. Due to these disadvantages, CC is not suitable for samples containing thin layers.

Having considered difficulties encountered in implementing FWDD and CC, we now

Table 4.2: Thickness comparison of layers I–III between SD results and nominal value.

	Layer I	Layer II	Layer III
Nominal thickness (μm)	30	$\sim$2230	60
SD result (μm)	$\sim$33	$\sim$2224	$\sim$58

employ sparse deconvolution (SD). In contrast to CC and FWDD, SD looks for a series of nonzero spikes (corresponding to echoes or reflections from material interfaces) in the reconstructed impulse-response function $h(t)$. That is, $h(t)$ is assumed to be sparse in the time domain, *i.e.*, almost everywhere zero. The approach proves convenient for subsequential signal processing, such as peak detection, as discussed in Refs. [28, 58]. SD can provide axial super-resolution while also performing well on thick layers, and is thus more suitable to investigate samples including thin layers or even in the absence of other information on the layer structure. Figure 4.18 is the reconstructed signal based on SD. Four nonzero peaks (two positive peaks and two negative peaks) associated with the interfaces of layers I, II, and III, and one weak peak reflected from the thin air layer hidden in layer II, are found in the SD reconstructed impulse response function $h(t)$, confirming the higher resolution compared to FWDD and CC. The thicknesses of layers I, II, and III are also calculated based on the corresponding optical distances Δt and are listed in Table 4.2. The minimum thickness that can be resolved by SD, based on our numerical simulation, is $\sim$ 0.174 ps with an SNR of 10 dB, corresponding to a Teflon layer with a thickness of 18 μm. Of note, the SD/IST algorithm, another type of SD our group has previously employed [58], has also been tested. Even though similar results are obtained, it involves a larger computational cost to achieve convergence and may not be well-suited for applications in which computational efficiency is required.

4.2.2 Experimental verification

In the above numerical demonstration based on synthetic data, SD exhibited better performance in addressing a sample having both thick and thin layers. Actual multi-layered structures are designed to evaluate the performance of SD experimentally. The experi-

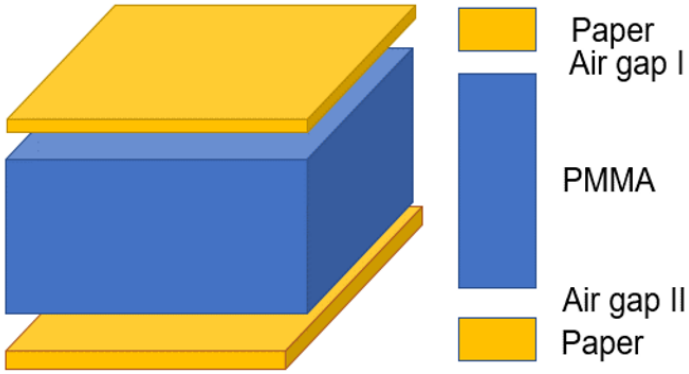

Figure 4.19: Schematic diagram of experimentally measured samples, composed of two paper layers, two air gaps, and one thick PMMA plastic sheet in between. The paper is a standard copy paper and the airgaps are produced by a suitable spacer layer.

mental data are then analyzed based on FWDD, CC, and SD. A schematic diagram of the sample is shown in Fig. 4.19. It is a five-layer structure with a layer of standard copy paper on each side of a thick PMMA plastic sheet. Airgaps are introduced intentionally between standard copy paper and the PMMA with a spacer. The paper thickness is $\sim$ 90 μm measured with a high-resolution calliper. The thickness of the airgap is roughly 150 μm. Six solid PMMA plastic sheets of various thicknesses d = 2, 4, 6, 8, 10, and 12 mm are utilized. Relevant physical properties of the PMMA sheets can be found in Ref. [57]. In order to prevent scattering in nonspecular directions, the top and bottom surfaces of the PMMA are diamond polished and shaped after fabrication.

THz transmission measurements were employed first to characterize the optical constants of PMMA. Based on curve fitting of $n(\nu)$ for a 2-mm-thick PMMA sheet, shown in Fig. 4.20 (a), we find a roughly linear relationship for $n(\nu)$ between 0.06 and 2 THz, *viz.* $\partial n/\partial \nu$ = -0.0096 THz^{-1}, for convenience, we quote values based on $n(\nu)$ with ν in THz. Figure 4.20 (b) displays the deviation between the actual $n(\nu)$ and the fitting; a good fit between the measured $n(\nu)$ and the modeled $n(\nu)$, is found. Similar results are also found for PMMA sheets of other thicknesses and are not presented here. The observation of negative dispersion at low frequency and the corresponding refractive index of PMMA

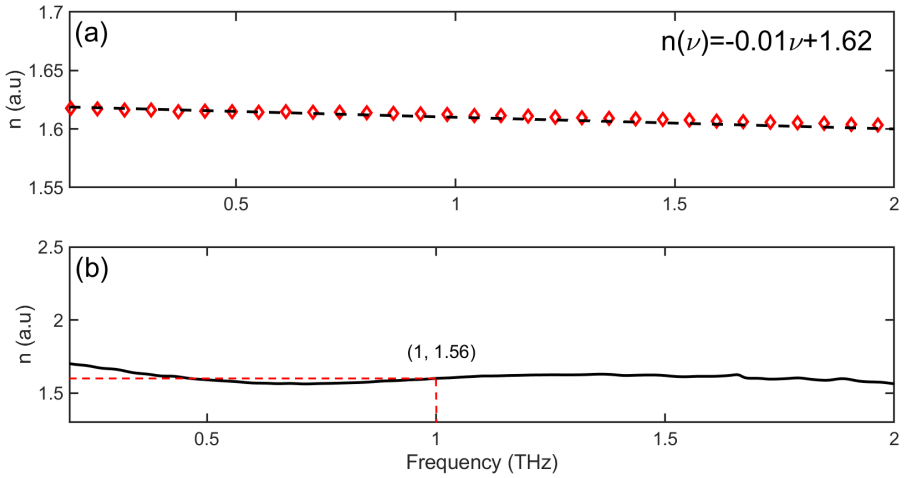

Figure 4.20: (a). Comparison between 1.621 – 0.0096 ν with n measured in THz and the frequency-dependent refractive indices $n(\nu)$ for PMMA. (b). the frequency-independent of refractive indices $n(\nu)$ for copy paper.

are in good agreement with Ref. [93]. It should also be mentioned that there is considerable scatter in published optical constants which may be due to the various spectroscopic techniques employed, differences in materials, or differences in experimental conditions. Our results, however, lie within the range of published values. Figure 4.20 (c) presents the $n(\nu)$ of copy paper between 0.06 and 2 THz. A relatively frequency-independent refractive index is found (*albeit* the paper is rather thin) with n $\sim$ 1.6 at 1 THz.

After characterizing PMMA and copy paper in transmission measurements, THz TOFT experiments were carried out next for stratigraphic characterization of these samples. It is noted that the bandwidth of the setup (TPS Spectra 3000 from TeraView Ltd., Cambridge, UK) extends to 3 THz, corresponding to a wavelength $\sim$ 100 μm; however, in practice, accounting for the SNR of the reflected signal, the usable bandwidth in $r(t)$ in these experiments is limited to about 2 THz. Any layer thickness $\lesssim$ 100 μm is thus considered optically thin. A typical reflected temporal signal (normalized) from the front and back of the sample with 6-mm PMMA is shown in Fig. 4.21. Two positive and one negative echoes are seen in Fig. 4.21(a). The first two positive echoes correspond to the air/paper and airgap/PMMA interfaces. The sign of the second echo is negative due to the Fresnel

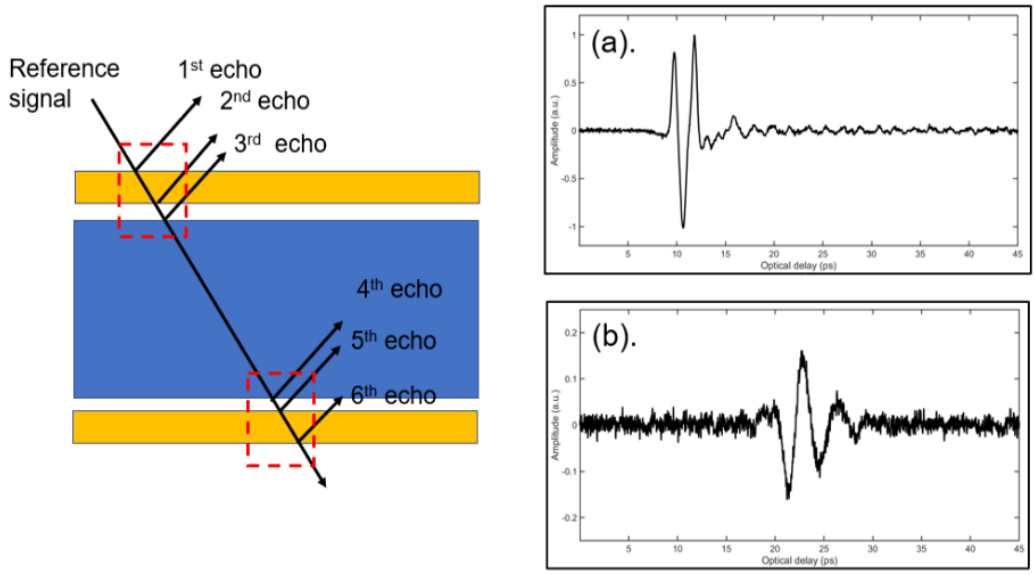

Figure 4.21: A typical reflected temporal signal from the front and back of the sample whose thickness of the PMMA sheet is 6 mm. Notice the different vertical scales for (a) and (b).

coefficient from a high- to low-refractive-index medium. However, when it comes to the signal reflected from the back of the sample, the situation becomes complex owing to the low SNR ensuing attenuation during propagation. Moreover, because of the dispersion in PMMA [*c.f.* Fig. 4.20 (a)], the reflected THz signal $r(t)$ includes echoes that not only decrease in amplitude but also broaden as the propagation distance increases. The reduction in the amplitudes of echoes following long-distance propagation inevitably contributes to the introduction of errors when seeking to locate the peak position as well as estimating the full width at half maximum (FWHM) of the echo.

According to our experience with synthetic data (see above), we directly employed SD to reconstruct $h(t)$. For thick PMMA, because of dispersion and attenuation, pulse-spreading and amplitude reduction occur in echoes associated with echoes that travel substantial distances in the sample, as shown in Fig. 4.22. The broadening, if not taken into consideration, degrades the ability of the deconvolution techniques to reconstruct the stratigraphy. Specifically, to achieve an accurate structural representation of the back of the sample, it is the transmitted signal through the back PMMA/airgap interface, that is used as

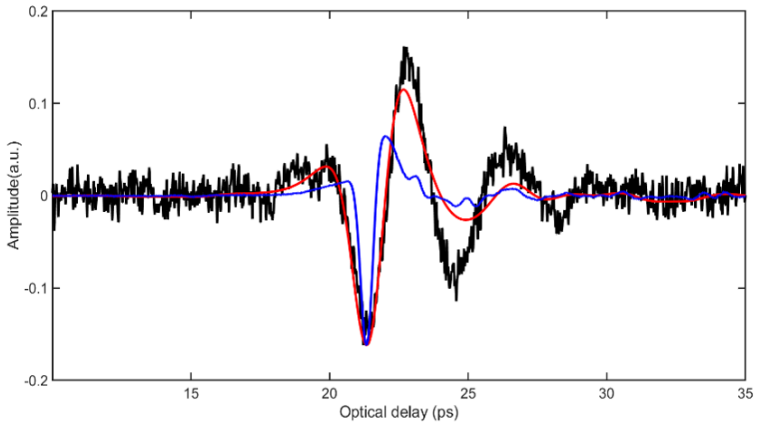

Figure 4.22: Comparison of the raw reflected echoes from the back of the sample whose thickness of PMMA sheet is 6 mm (black), the reference signal (blue), and the signal propagated through the back PMMA/airgap interface extrapolated based on the dispersion model (red).

the reference signal when investigating the echo reflected from the back of the sample. This signal is estimated using the dispersive propagation model presented in Ref. [110]. This model is different from the quasi-Dirac δ-function dispersion model we used in previous work [103], and it does not involve a cumbersome parameter tuning process. All relevant parameters are obtained from the transmission measurement. It is thus simpler and more straightforward to implement. A high similarity between the extrapolated signal accounting for dispersion and the raw reflected signal at the back PMMA/air gap interface is found and shown in Fig. 4.22.

A deconvolved $h(t)$ only with several nonzero points to represent the structural features, is presented clearly in Fig. 4.23 (a) and (b), and six sharp peaks, corresponding to echoes 1 through 6, are clearly observed. The thickness of the paper and airgap on both sides of the sample, as well as that of the thick PMMA plastic itself, can be estimated based on SD. The determined thicknesses are 87 μm, 167 μm, and 5.92 mm, respectively, showing excellent agreement with the independently measured values. It is also worth mentioning that dispersion is a crucial factor that cannot be ignored when analyzing the reflected signals from coatings on the back of the thick PMMA; if dispersion were neglected in the analysis, the broadened peak would be treated as the sum of several erroneous peaks by the algorithm

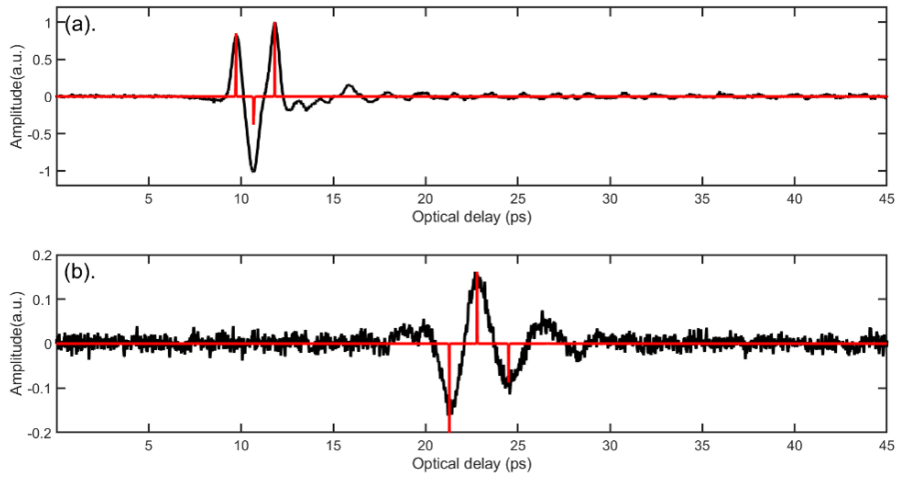

Figure 4.23: The comparison between the deconvolved results by SD (red) and the raw reflected signal (black) from the front of sample (a), and the back of sample (b). The thickness of the PMMA sheet is 6 mm.

of sparse deconvolution. Moreover, we find that when the thickness of PMMA is larger than 8 mm, the 6^{th} echo fails to be distinguished entirely.

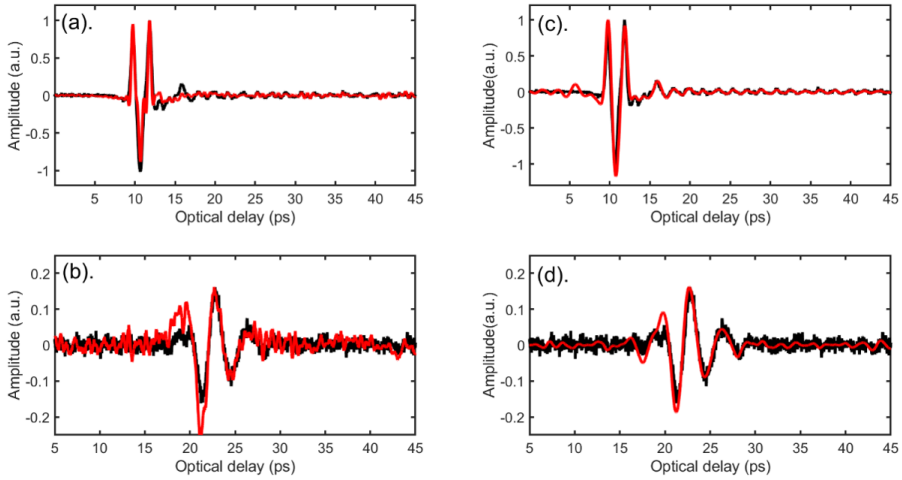

Figure 4.24: Comparison between the deconvolved result for the signal reflected from the front of the sample by (a) FWDD and (c) CC. Comparison between the deconvolved result for the signal reflected from the back of the sample by (b) FWDD and (d) CC. The thickness of the PMMA sheet is 6 mm.

The performance of FWDD and CC is also tested and the corresponding deconvolved results are presented in Fig. 4.24. Figures 4.24 (a) and (b) represent the reflected signals from the front and back of the PMMA sample when FWDD is employed. We observe

some level of improvement in the SNR. In the case of the back reflections [Fig. 4.24 (b)], however, the interpretation is arduous as the amplitudes of the post-processed echoes are comparable to the noise floor and, further, side-peak oscillations are present. The deconvolved signal by FWDD is thus insufficient to provide a reliable reconstruction. Figures 4.24 (c)-(d) show the signals reflected from the front and back of the PMMA sample when CC is employed. Pulse spreading is taken into consideration to overcome the severe waveform distortion of echoes from the back of the sample. It is clear that the SNR of the reconstructed signal is greater than that yielded by FWDD and interface positions on the backside of the sample can be more easily identified. Interpretation is still not as clear as with the quasi-ideal impulse response provided by the SD technique; in particular, the width of the deconvolved echoes leads to estimation uncertainty and additional oscillations observed in the signal could be wrongly interpreted as interfaces. Even though CC performs well for thick samples on the ground that CC maximizes SNR when an *identical* waveform (echo) is immersed in noise, CC performs poorly and is unreliable when thin layers are also involved.

The axial resolution of the SD algorithm also merits quantitative study. Considering the maximum dynamic range $>$ 50 dB of the reference THz signal $h(t)$, generated by the experimental apparatus, we observe, through simulation, that the maximum thickness d of the PMMA plastic sheet that can be resolved by SD is $\sim$ 17 mm, which is lower than the value for CC ($\sim$ 36 mm [103]). Even though the maximum resolvable thickness is lower than for CC, SD provides a clearer and more accurate assessment of the complex structure of samples with intermediate thickness and thin layers since CC fails to identify the thin layers. We last note that multiple reflections are quite weak and have been ignored, even though, for our axially symmetric structure, there are features arising from single echoes from the back surface and multiple echoes from the structure on the front surface that coincide with single echoes from the back surface. As the multiple echoes are quite weak, they do not significantly affect the analysis.

In conclusion, SD-based on an interior-point method in conjunction with a propagation model accounting for dispersion is demonstrated to be successful in reconstructing the stratigraphy of a complex sample incorporating both optically thick and thin layers. The use of an interior-point method with the PCG algorithm significantly decreases the computational cost of the SD technique compared to the standard iterative soft-thresholding algorithm. The dispersion model is used to take into account the significant attenuation and distortion endured by the THz signal in a thick sample. The proposed technique is compared to two other post-processing techniques, *namely*, FWDD and CC. FWDD faces severe limitations as it is ill-suited to resolve thick samples [29] and can also fail to identify optically thin layers. CC has the advantage of performing well for thicker samples than SD but is shown to fail to resolve additional thin layers in thick samples. We demonstrate that the inclusion of a dispersion model in the SD procedure increases the maximum sample thickness than can be resolved while maintaining a significantly better axial resolution than FWDD and CC. As illustrated by the experimental results, SD may be the preferred option for stratigraphic reconstruction of moderately thick samples with complex structures. For example, such an approach will be of value to characterize coatings on electrically insulating materials when there are constraints requiring access from the backside.

4.3 Terahertz imaging for paper handling of legacy documents

Despite predictions of the paperless office, global demand for printing and writing paper remains strong, and the paper appears to be here to stay for some time. Not only firms, but also governments, libraries, and archives are in possession of large collections of legacy documents that still must be sorted and scanned. Our interest here is to explore the potential of THz techniques for various paper-handling tasks. To provide context, though this is not the sole application, in an automated sheet feeder for large-volume scanning, it is useful beforehand to have a sheet count and determine whether any sheets in a feeder stack may be stapled to prevent feeder failure. In this paper, therefore, we focus on obtaining

page count s and locating foreign objects (*e.g.*, staples) in multipage legacy documents, which are prerequisites for subsequent paper-handling tasks, such as scanning. After obtaining the dielectric properties of paper stacks for $\nu \in$ [0.2 THz, 2 THz] in transmission measurements, the internal structure of paper stacks is presented based on the THz TOFT. The page count and staple location within paper stacks are determined from THz reflection data. Finally, the exact position of stapled sheets buried in a paper stack is determined by THz TOFT.

THz transmission and reflection experiments were conducted using a commercial THz time-domain spectrometer (TPS Spectra 3000 from TeraView Ltd., Cambridge, UK) in a laboratory at a temperature of 22 °C with humidity $< 48\%$. The effective bandwidth of the apparatus is $\nu \in$ [60 GHz, 3 THz]; however, to avoid the low signal-to-noise ratio (SNR) at the extreme ends of the band after interaction with the paper stacks, only $\nu \in$ [0.2 THz, 3 THz] is used for analysis. Because of the confounding effects of water vapor, the propagation path was purged with dry N_2 prior to the transmission measurements. Each recorded signal was averaged 1800 times to achieve high SNR. Balancing the noise level with the spectral resolution, the Black-Harris 3-term apodization method was also utilized to smoothen the spectrum and suppress spectral artifacts [111]. For the TOFT measurements (in reflection), the sample is moved in discrete spatial steps of 200 μm in the $x-$ and $y-$ directions by a set of motorized stages. Dry N_2 was also utilized prior to each reflection measurement to remove moisture proximate to the THz emitter and receiver. Before imaging the paper stack, a THz reference signal was recorded by setting a metal plate at the sample position. The result, then, is a three-dimensional dataset with the two transverse directions as two dimensions and the time delay of the measured THz signal as the third dimension.

The paper studied here is standard A4 copy paper manufactured by LECTA (Paperbox brand multifunction white laser-printer and photocopy paper), and the relevant physical properties of the copy paper are shown in Table 4.3. All paper investigated was stored

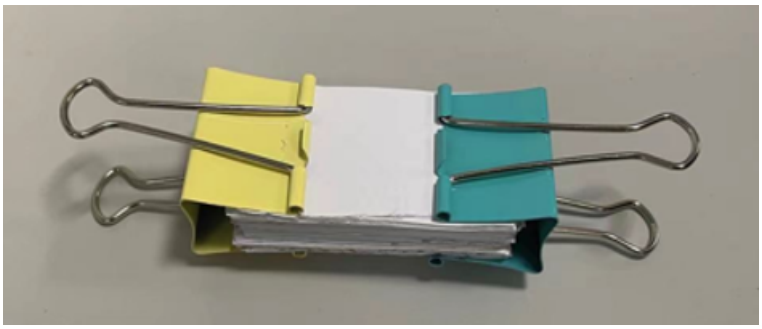

Figure 4.25: Paper stack held in custom-build jig based on binder clips (Home Depot, medium, multicolor). Size of paper sheets is ∼8 cm × 5 cm.

Table 4.3: The physical characteristics of the copy paper studied.

Properties	Value	Tolerance
Weight	80 g/m^2	±4%
Thickness	102 μm	±4%
Opacity	87 %	±4%
Relative humidity	40 %	±5%

under the temperature and humidity conditions of the laboratory for which the moisture content of the paper is approximately 7.5% [112]. While individual sheets of paper may have slightly different water content and may otherwise differ, as we shall see below, in THz TOFT experiments, we are still able to identify the various sheets of paper within a stack. We specifically studied unconsolidated paper stacks ($s \in [1, 155]$), *i.e.*, the paper sheets were not compressed together except at the ends away from the scanning area. Therefore, the paper stacks were comprised of copy paper with naturally occurring air gaps between the sheets, presenting a stratified medium. Stacks of paper were cut down to 8 cm × 5 cm rectangles from full A4 sheets (21 cm × 29.7 cm) before being stacked. The ends of the paper stacks were held in a custom-built jig based on binder clips, but the regions of the stacks imaged were not compressed, as shown in Figure 4.25.

4.3.1 Terahertz dielectric properties

We begin by characterizing the dielectric properties of paper stacks in transmission experiments. In this case, a THz pulse is propagated through the paper stack located at the focus

of the optical system, and the effect on the various spectral components is compared with the reference signal (*i.e.*, the THz pulse produced by the apparatus).

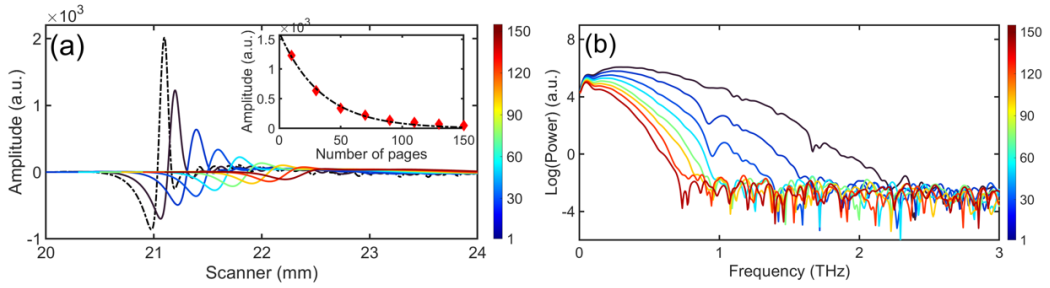

Figure 4.26: (a) THz signals (electric field) transmitted through paper stacks with a various page count s ranging from 1 to 155. Inset shows the peak amplitude as a function of s in the paper stacks. (b) Power spectra of the corresponding transmitted signals are shown in (a). The color bars indicate the number s of sheets in a stack corresponding to a given curve.

Figure 4.26 (a) shows transmitted signals for paper stacks with various page counts s ranging from 1 to 155 sheets, and (b) the corresponding power spectra of these transmitted signals. The number s of sheets in the stack is coded by the color bar to the right of each panel. It is unsurprising that the reference signal has the highest amplitude and shortest propagation time while both propagation delay and reduction of peak height increase with s. Referring to Fig. 4.26 (b), the useable bandwidth decreases with increasing s as the high-frequency portion of the spectra fall below the noise floor of the experiment, demonstrating the loss of high frequency information as the THz waves suffer attenuation in the paper stacks. When $s \gtrsim 155$, the transmitted signal amplitude is comparable to the noise. The observed attenuation is in line with that seen in Refs. [113, 114] where waveplates of 150 to 220 sheets and intervening airgaps were fabricated.

The refractive index $n(\nu)$ and attenuation coefficient $\alpha(\nu)$ are calculated based on the complex fast Fourier transform of pulses transmitted through the paper stack, compared with the incident (reference) pulse. Denote the amplitude and phase of the electric field as $E_s(\nu)$, $\phi_s(\nu)$ and $E_r(\nu)$, $\phi_r(\nu)$. One obtains [111],

$$\alpha(\nu) = -2/d_s \ln[E_s(\nu)/(T(\nu)E_r(\nu))] \tag{4.18}$$

$$n(\nu) = 1 + c[\phi_s(\nu) - \phi_r(\nu)]/(2\pi\nu d_s) \tag{4.19}$$

where d_s is the paper-stack thickness measured using callipers with an accuracy of 10 μm, and $T(\nu)$ is the transmittance associated with the air/paper stack and paper stack/air interfaces,

$$T(\nu) = 1 - [n(\nu) - 1]^2/[n(\nu) + 1]^2. \tag{4.20}$$

The paper stack, of course, also contains air gaps (unit refractive index) between adjacent sheets, leading to a discrepancy between d_s and $s \times d$ with d the single-sheet thickness (102 $\pm$ 4 μm). In measuring d_s, the callipers were tightened to remove excess air from the paper stack without unduly compressing the paper. Though more accurate approaches may be implemented, this provided consistent results as we see below. Moreover, as a multilayer structure, coherent interference effects (due to multiple reflections) will play a role in the reflected signal. Assuming multiple reflections can be neglected in the THz transmission, only the paper contributes to $n(\nu)$ since the refractive index of air is 1. This assumption is justified due to the rather modest value of $n(\nu)$ for paper (see below).

The frequency-dependent optical constants $n(\nu)$ and $\alpha(\nu)$ are plotted in Fig. 4.27 with (a) $n(\nu)$ and (b) $\alpha(\nu)$ for $s \in [1, 155]$. The optical constants are meaningful for ν within the effective dynamic range determined by s as discussed above [see Fig. 4.26 (b)]. The dispersion $dn(\nu)/d\nu < 0$ for all cases, and $n(\nu)$ decreasing from 1.59 at 0.2 THz to 1.54 at 2 THz when $s = 10$, as shown in Fig. 4.27 (c); $dn/d\nu \approx -0.02$ THz^{-1}. The values are in good agreement with those reported in Ref. [115]. The weak dispersion in $n(\nu)$ along with the ν - dependent $\alpha(\nu)$ contributes to the change of pulse shape during the propagation in the paper stack. Figure 4.27 (b) shows $\alpha(\nu)$ for various s, and $\alpha(\nu)$ increases from 1.7 cm^{-1} at 0.2 THz to 32.7 cm^{-1} at 2 THz for s = 10 sheets. The values of $\alpha(\nu)$ obtained in this work are consistent with literature values [115]. The values plotted are only meaningful for ν less than an upper value determined when the power spectra in Fig. 4.26 (b) drops below

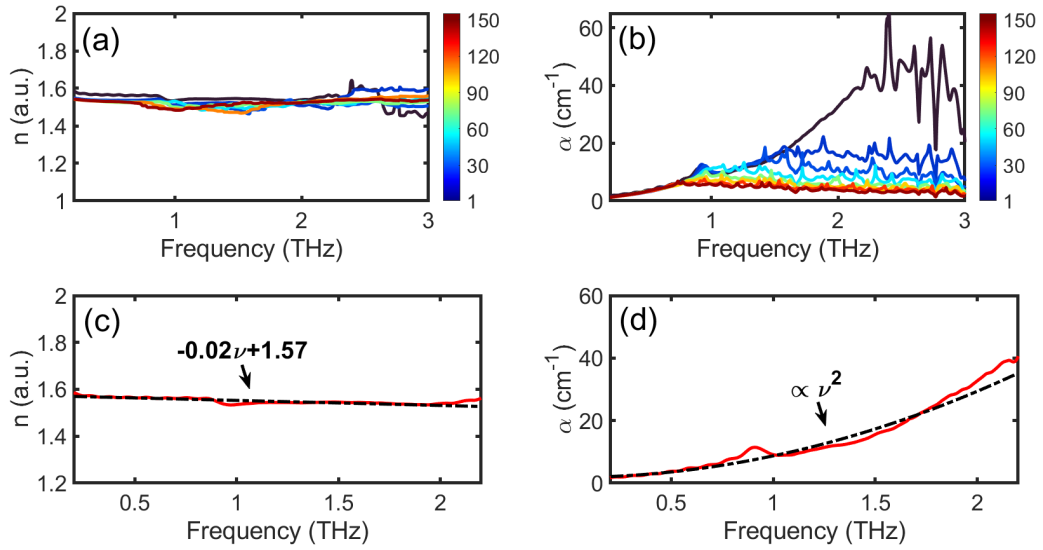

Figure 4.27: (a) Refractive index $n(\nu)$ and (b) attenuation constant $\alpha(\nu)$ of paper stacks with s = 1 to 155. (c) $n(\nu)$ for s =10 (by way of example) and a linear fit. (d) $\alpha(\nu)$ for s = 10 and a quadratic fit.

the noise floor. Referring the Fig. 4.27 (b), this maximum ν decreases with increasing s and corresponds to the maximum frequency for which $\alpha(\nu)$ is quadratic. For higher frequencies, $\alpha(\nu)$ is dominated by noise. Thus, the apparent low attenuation at high ν for large s is just an artifact of this s-dependent dynamic range. $\alpha(\nu)$ within the effective dynamic range [0.2 THz, 2.2 THz] (for $s = 10$) estimated based on Fig. 4.26 (b), varies roughly quadratically in ν, as shown in Fig. 4.27 (d). Similar behavior of $\alpha(\nu)$ was also found in Ref. [115] and is typical of disordered media [9, 116, 117, 118, 119]

4.3.2 Page count s in paper stacks

The first practical application of THz techniques discussed here is to ascertain page count s from the THz data. As observed in the inset of Fig. 4.26 (a), the maximum amplitude of the transmitted signal through the paper stack decreases approximately exponentially with increasing s. We can thus infer s roughly by calibrating the transmitted amplitude against s. Such an approach gives rise to an error of a few sheets increasing with s. It must also be pointed out that this technique only works when the paper in the stack is of a uniform and

known type. For the cases we studied, when $s \leq 60$, the error between the inferred page count and the nominal $s \leq 4$, while the error reaches 30 when s = 150 based on calibrating s against transmission. To extend this approach to larger s would require more powerful THz sources and lower-noise THz measurements.

To circumvent the limits imposed by errors in the above approach as well as the requirement of working with a single known paper type, we employ an alternative approach based on THz TOFT. This approach will produce essentially error-free measurements of s for $s \lesssim 20$ and can provide additional structural information on paper stacks Namely, we employ THz TOFT to reconstruct the stratigraphy of the paper stack. Due to the presence of noise in the measurement, we implement frequency wavelet-domain deconvolution (FWDD) to enhance the signal-to-noise ratio (SNR) in the measurement. FWDD, as a simple but effective denoising technique, involves cascading a band-pass filter with a filter based on wavelets that resemble the incident THz pulse. The wavelet basis selectively filters out unrelated features from the detected signal retaining those features that resemble the incident THz (reference) pulse. Because dispersion shown in Fig. 4.27 (c) is weak (and within the frequency range that dominates the signal, the frequency dependence of $\alpha(\nu)$ is not substantial), FWDD is easily implemented.

Figure 4.28 (a) shows a schematic diagram of a s = 18 stack, while (b) shows the corresponding raw reflected signal from the THz TOFT experiment in red and the FWDD reconstruction in black. FWDD is helpful to clean up the signal to unambiguously track the various echoes. The approach to estimating s is to count the number of reflections (one from each side of each paper sheet) in the reconstructed THz TOFT signal. Associated with each sheet of paper is a positive-amplitude echo (from air to the higher-index paper) and a negative-amplitude echo (from higher-index paper to air). The pink vertical bars in Fig. 4.28 (b) indicate the reconstructed locations of the paper sheets. Between successive sheets of paper are air gaps. Inasmuch as the sheets in the stack are not compressed during the measurement, the air-gap thicknesses vary between sheets. In addition, the surface texture

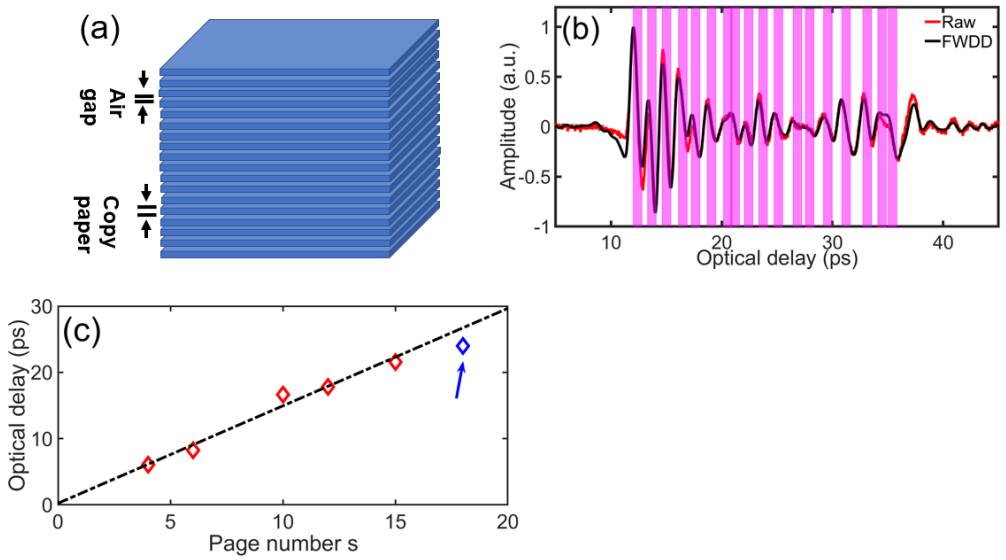

Figure 4.28: (a) Schematic of s = 18 stack. (b) Raw (red) reflected signal in THz TOFT experiment and the corresponding deconvolved signal after frequency wavelet-domain deconvolution (FWDD) (black). Pink vertical bars indicate the reconstructed locations of the paper sheets in the stack. (c) Relationship between optical delay from the linear fit based on the data for s = 4, 6, 10, 12, and 15 (red) and the measured optical delay (blue) for s =18.

may contribute to the formation of the airgaps; it would be interesting to see if this occurs with smoother paper, *e.g.* publication-grade lightweight coated paper or glossy newsprint. Even though we have not fully characterized the air gaps between the sheets, because the refractive index of air is unity, the relative optical delay within paper stacks compared with an equal overall thickness of the air is roughly proportional to s (for a uniform paper type as herein) as shown in Fig. 4.28 (c), in which the experimental points for s = 4, 6, 10, 12, and 15 are also shown. The error between the estimated page count, based on the measured optical delay using the linear relationship, fitted by the data for s = 4, 6, 10, 12, and 15, and the nominal value for s = 18, is smaller than 1. Of course, the error is reduced by looking directly at the stratigraphic reconstruction.

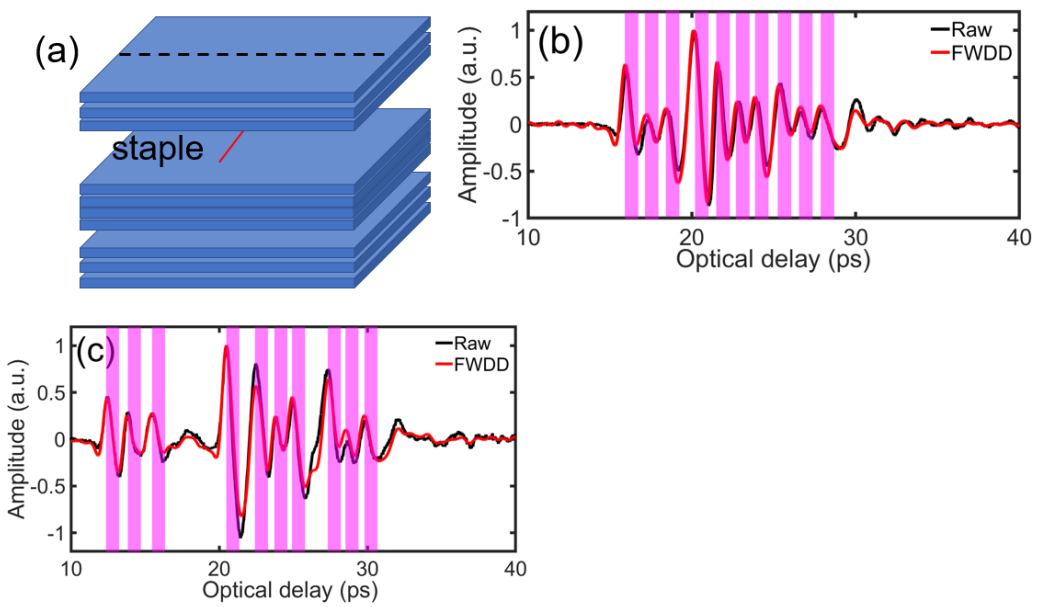

Figure 4.29: (a) Schematic of s = 10 stack with the four central pages stapled together. Raw (black) reflected signal, and FWDD (red) reconstructed signals in THz TOFT data (b) away from the staple, and (c) near the staple, respectively. The horizontal dashed line near the center of paper stack s = 10, marked 'cross-section', refers to the B-scan presented in Fig. 4.30 (a) and (b).

4.3.3 Three-dimensional staple location

The handling of unsorted legacy documents may be complicated by foreign objects hidden in paper stacks. For example, loose staples or paper clips may be located between sheets of paper, and some pages within a stack may be stapled, and these staples may not be visually evident. In this section, we demonstrate the three-dimensional location of stapled documents hidden in paper stacks using the technique of THz TOFT.

We consider a s = 10-sheet stack with the central four sheets stapled together as shown schematically in Fig. 4.29 (a). The raw (black) reflected THz TOFT signals away from and near the staple as well as the corresponding deconvolved signals by FWDD (red) are shown in Fig. 4.29 (b) and (c), respectively. Not surprisingly, near the staple, relatively large air gaps just above and below the four stapled sheets are clearly seen, and the four stapled sheets themselves are compressed together, as evident in Fig. 4.29 (c).

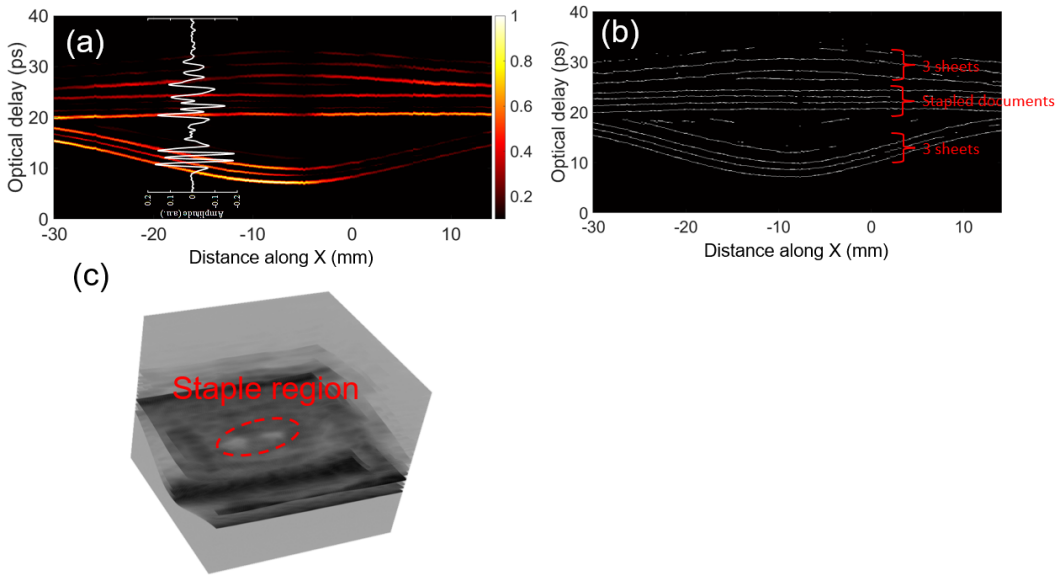

Figure 4.30: (a) B-scan through a cross-section through the $s = 10$ stack containing a stapled document along the dashed line shown in Fig. 4.29 (a) with an example of the FWDD reconstructed signal at the position indicated. Large air gaps above and below the stapled sheets are evident. The color scale is linear in the amplitude of the reflected THz signal. Thus, yellow indicates a strong reflection, red a moderate reflection, *etc*. (b) shows the corresponding binary THz B-scan based on the FWDD reconstruction. (c) Three-dimensional rendering of THz TOFT data to emphasize the staple location.

To better visualize the structure, we present the FWDD reconstructed data in a cross-section through the paper stack, known as a B-scan in Fig. 4.30 (a). A B-scan is a cross-section in space through the three-dimensional data set of the reflected THz signal, *i.e.*, in the two transverse directions across the sample and for the third dimension, the time delay of the detected reflected THz signal serves as a surrogate for depth into the sample in the axial direction. To emphasize, we indeed have a three-dimensional data set and are free to choose any cross-section; we here choose a cross-section that is particularly illustrative of the approach. Figure 4.30 (a) also shows an example of the FWDD reconstructed THz TOFT the signal at the position -20 mm on the cross-section. Note that the B-scan is simply composed of all such signals along the cross-section plotted on the color scale indicated on the right.

In order to eliminate the influence of the alternating signs of the successive echoes as

well as the variation in the amplitudes of the peaks/valleys in the reflected THz signal, we can replot the B-scan in Fig. 4.30 (a) based on the FWDD reconstruction as a binary B-scan in which a valid extremum plotted as a white point against a black background regardless of the sign and amplitude of the peak/valley, as shown in Fig. 4.30 (b). The three loose sheets above and the three loose sheets below the four stapled sheets, as well as the stapled sheets, are clearly seen as indicated. To further facilitate visualization of the staple location, we present a three-dimensional rendering, based on FWDD reconstructed data in Fig. 4.30 (c). Here, the reflection from the legs of the staple is found. Of course, this rendering can be freely rotated on the computer, assisting in the visualization. Note that metals present strong THz reflections whether or not the metal is ferrous; thus, THz TOFT can detect, for example, aluminium staples, whereas simple magnetic approaches are limited to iron-bearing staples. Magnetic approaches are also likely to have poor resolution. In our experiments, the width of the wire forming the staple itself may be close to barely resolved as the width of the beam at the focus at 2 THz is $\sim$ 700 μm in the air for our numerical aperture. Finally, though x-rays are expected to clearly identify staples in paper stacks, ionizing radiation is likely to be avoided due to potential health risks.

The examples demonstrated here to open the door to other related applications. Though the examples we present here focus on a single paper type, legacy documents might also have mixed paper. Other types of foreign objects, including paper scraps, self-adhesive notes, tape, paperclips–both metal and plastic–might also be present. These situations are yet to be studied. Nonetheless, our work suggests that THz techniques merit further exploration for practical implementation in paper handling of legacy documents.

CHAPTER 5

MATERIAL CHARACTERIZATION AT TERAHERTZ FREQUENCIES

In this chapter, terahertz (THz) time-domain spectroscopy (TDS) is carried out for the material characterization of electrically insulating materials. Birefringence, one of the significant parameters of anisotropic materials, is also investigated based on polarization-resolved THz TDS.

This chapter presents three case studies. The first study is to characterize nanoporous (NP) Al_2O_3 films grown on Al substrate through a two-step electrochemical anodization process in a non-destructive manner. Polarization-resolved THz TDS studies THz birefringence associated with the crystal structure of formed NP Al_2O_3 films. Moreover, the surface morphology, as well as the roughness of formed NP Al_2O_3 films, are also characterized by THz reflectometry as well as scattering imaging. It shows that before the second anodization, the irregular surface morphology of the NP Al_2O_3 films leads to significant THz scattering. In contrast, the far more homogeneous films following the second anodization show far less scattering. The THz results are corroborated by field-emission scanning electron microscopy (FE-SEM) and atomic force microscopy (AFM), both of which are time-consuming, not easy to operate, and can only provide the local characterization of nanoporous Al_2O_3 films on Al substrate.

The second case study is to diagnose the injection-molded weld lines in an acrylonitrile butadiene styrene (ABS) thermoplastic electrical receptacle plate using polarized-resolved THz reflective imaging. THz results show morphological features at the weld lines and reveal THz birefringence properties localized around the welds, indicating frozen-in molecular orientation and stress proximate to the welds. Surface acoustic microscopy (SAM) corroborates the morphological features at the welds shown by THz imaging and reveals anomalous mechanical properties at the weld lines. These results indicate that THz-

based technology provides non-destructive reliability assessment and quality control for injection-molded thermoplastic products.

The third case study is to systematically characterize the dielectric and loss tangent of three thermoplastics, *namely*, polycarbonate (PC), polymethyl methacrylate (PMMA), and acrylonitrile butadiene styrene (ABS) using commercial THz TDS over a broad frequency ν range from 0.5 to 2 THz. The plastics investigated possess a refractive index ($\sim$ 1.6-1.7) in the 6G band with low dispersion. The absorption, however, increases at high frequencies, as is common in disordered materials, highlighting a key challenge for 6G. The obtained values of refractive index and absorption coefficients are consistent with the literature. Nonetheless, in absolute terms, all the thermoplastics studied present low loss compared with (higher index) common glasses and ceramics within the entire frequency range, suggesting they are promising candidates for selected applications for future 6G systems.

5.1 Nondestructive characterization of nanoporous Al_2O_3 films at terahertz frequencies

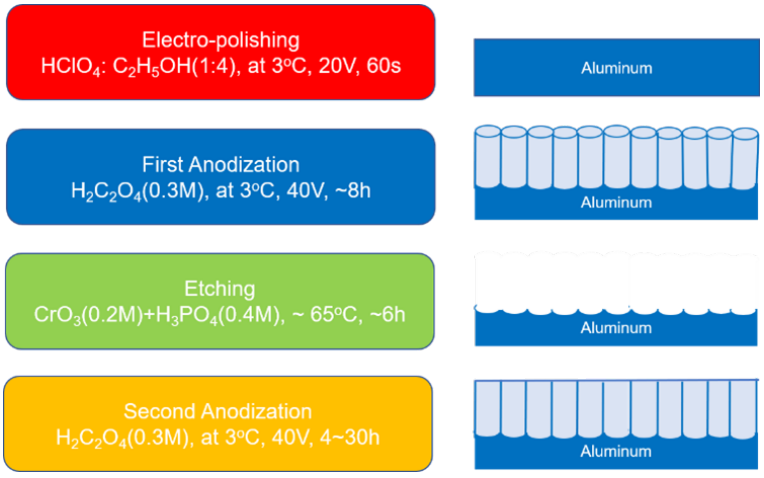

Figure 5.1: Second anodization process. The left column shows process flow; the right column schematic of the cross-section through the surface including the NP Al_2O_3 film.

Eight self-ordered NP Al_2O_3 films are studied *via* THz reflective imaging. The fabrication

of NP Al_2O_3 films on a grain-free aluminium foil (99.99%, 100 μm thickness, Tokai Aluminum Foil Company) [120] is conducted by a typical electrochemical anodization process, and the schematic diagram of the process flow is presented in Fig. 5.1. The dimensions of the Al foil used in this research are 6.7 cm by 1.4 cm. Pretreatments to degrease the foil and remove initial surface oxide are first performed. To minimize surface roughness of the starting Al foil, substrates are first prepared by electropolishing for 60 s with a bias voltage of 20 V in a 1:4 volume mixture solution of $HClO_4$:C_2H_5OH at 3 °C. Field emission scanning electron microscopy (FE-SEM, Hitachi S-4700) is used to characterize the surface morphology of the Al foil after the electropolishing process. The Al strips are removed and there are no obvious defects found in FE-SEM images as shown in Fig. 5.2 (a).

Subsequently, a two-step anodization process is carried out in a 0.3 M $H_2C_2O_4$ solution. The temperature of the reactive solution is set to 3 °C. The duration of the first anodization is 8 h at 40 V bias voltage, and the thickness of the NP film is controlled by the anodization duration. A constant stirring process is maintained through the entire first anodization.

A $\sim$ 80 μm NP Al_2O_3 layer with a nonuniform layer on the top and a uniform layer on the bottom can be observed in cross-section field-emission scanning electron microscopy (FE-SEM), shown in Ref. [121]. Fig. 5.2 (b) displays the top-view SEM image of the sample after the first anodization. It is relatively obvious that this formed NP Al_2O_3 film is irregular. Inhomogeneity may result from the generation of heat on the surface of the electrolyte during the first anodization. Moreover, at the bottom of the NP Al_2O_3 layer, a compact dielectric oxide barrier layer is formed after the first anodization. The structure of the barrier layer can be characterized by cross-section FE-SEM, shown in Fig. 5.3. The thickness of the barrier layer ranges from 30 nm to 45 nm.

In order to improve the regularity of the NP nanoarray, the disordered NP Al_2O_3 film is removed using wet chemical etching with a 0.2 M CrO_3 and 0.4 M H_3PO_4 solution at $\sim$ 65 °C for $\sim$ 6 h. A highly periodic nano-concave structure on the Al substrate is shown in Fig. 5.4. These pits serve as the template for the formation of the uniform NP Al_2O_3 film

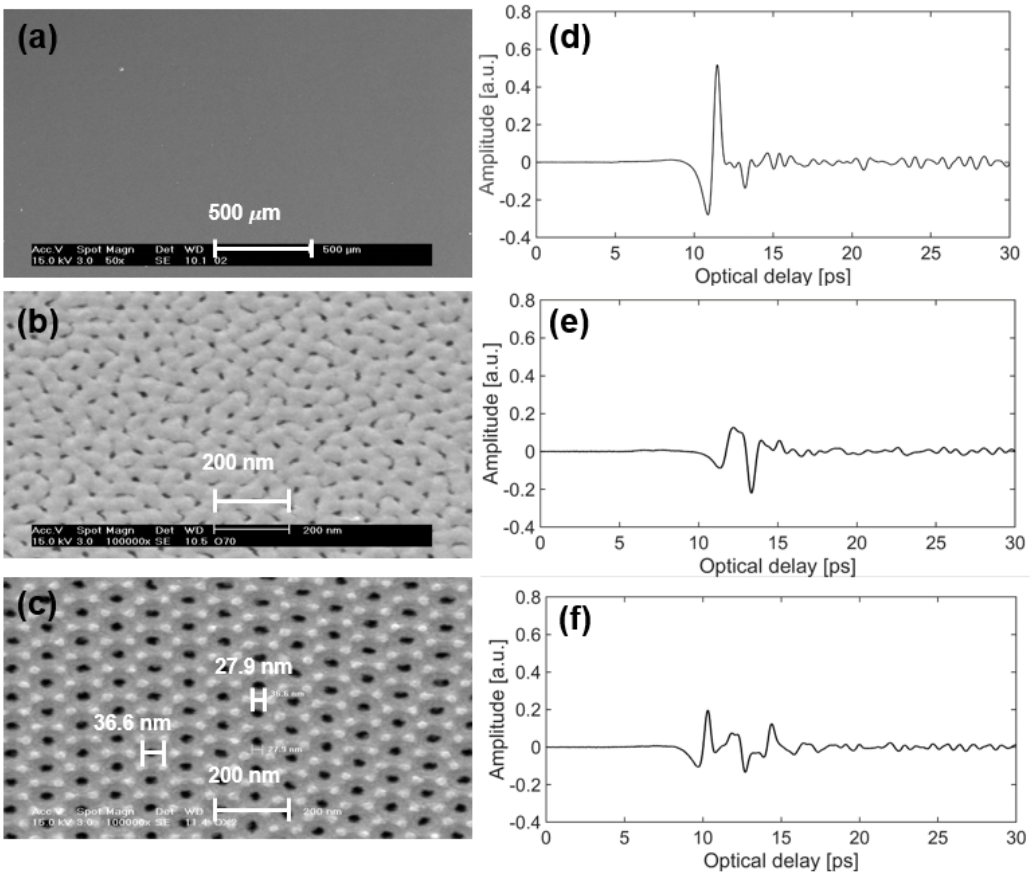

Figure 5.2: FE-SEM showing surface morphology after (a) electro-polishing, (b) first anodization, and (c) second anodization. Corresponding reflected THz signals are presented in (d)-(f).

[122].

The second anodization is carried out using the same apparatus and under the same condition (temperature, concentration of solution, and bias voltage). Well-ordered hexagonal pore arrays are obtained as shown in Fig. 5.2 (c), demonstrating that the irregular pore lattice after the first anodization does not adversely influence the formation of NP Al_2O_3 films during the second anodization. The pore diameter and interpore distance can be estimated based on top-view FE-SEM images. The interpore distance and pore diameter are 105 ± 5 nm and 33 ± 3 nm, respectively.

Pulsed THz reflective imaging and THz scattering imaging are employed first in this study. In scattering imaging, the detector is placed off the specular direction. The genera-

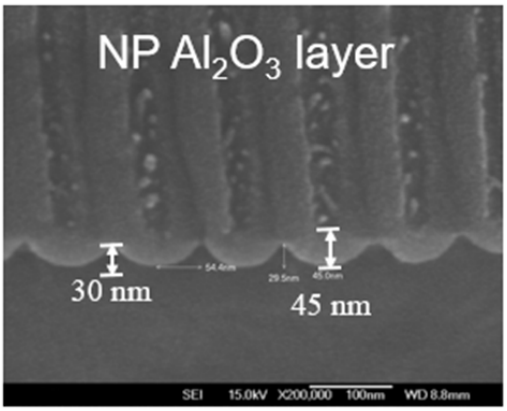

Figure 5.3: FE-SEM image of a barrier layer of NP Al_2O_3 film on Al substrate.

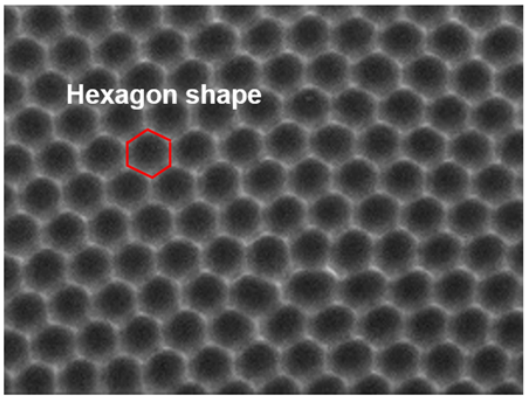

Figure 5.4: Top-view FE-SEM for sample after etching following the first anodization process.

tion of THz pulsed radiation is based on a photoconductive switch. Quasi-single-cycle THz pulses with bandwidth 60 GHz to 3 THz are generated in a biased GaAs antenna excited by an Er-doped fiber laser emitting sub-100-fs 780-nm pulses at 100 MHz repetition rate with an average output power $>$ 65 mW. Coherent detection of the reflected THz radiation is performed in a similar photoconductive-antenna circuit. By focusing the laser beam onto the photoconductive gap of a biased semi-conductor emitter and using a similar receiver, a current proportional to the THz electric field is measured. A delay line is used to change the difference in the optical delay between the incoming THz pulse and the probe laser pulse at the receiver. A bias is also applied across the emitter and receiver to generate a time-gated output signal.

The THz measurements were carried out in an air-conditioned laboratory at 22 °C with humidity < 48 %. Before the THz measurement, the reference pulse, *i.e.*, the THz pulse produced by the apparatus, was recorded by setting a bare metal plate (an excellent THz reflector) at the sample position. The sample was raster-scanned by a set of motorized stages moving in the $x-$ and $y-$ directions with a step size of 0.2 mm. The depth-of-focus (roughly twice the Rayleigh length z_R) and focus spot size are frequency dependent, which is ~ 7 mm and ~ 1.5 mm at 1 THz, respectively. The recorded reflected temporal signal at each pixel contains 4096 data points (corresponding to a sampling period T_s of 0.0116 ps) and is averaged over 10 shots per pixel to reduce the effect of noise.

5.1.1 Surface morphology characterization of nanoporous Al_2O_3 films

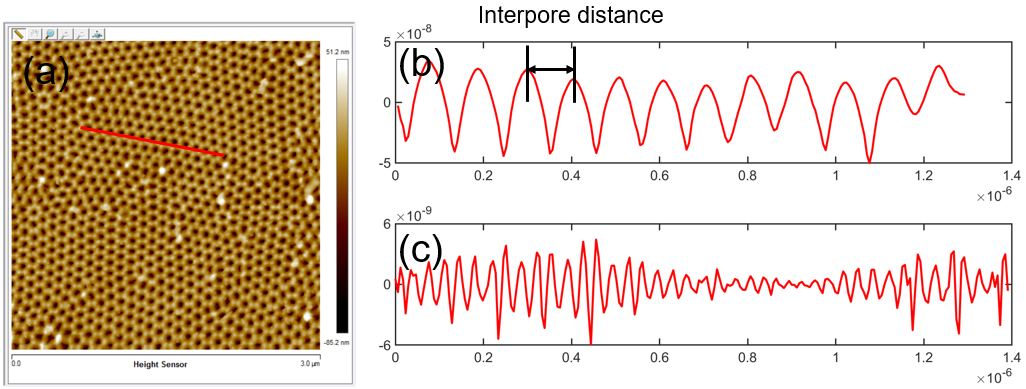

Figure 5.5: (a) AFM image of NP Al_2O_3 film on Al substrate after the second anodization process; (b) the surface primary profile, and (c) roughness profile along the red line in Fig. 5.5 (a).

AFM (Dimension Edge, Bruker) is used to characterize the surface morphology of the NP Al_2O_3 film. Fig. 5.5 (a) shows the typical AFM image of an NP Al_2O_3 film after the second anodization. High regularity of closed packed hexagonal cells with circular nanopores is seen. The pore diameter, the interpore distance as well as the regularity of the NP arrays can be calculated by analysis software through the line scan primary profiles of AFM, shown in Fig. 5.5 (b). The peaks and the valleys refer to walls and pores, respectively. The calculated interpore distance based on the interval between the peak or valley

regions is $\sim$ 110 nm, within the range estimated using the FE-SEM image presented in Fig. 5.2 (c). Based on the primary surface morphology of NP Al_2O_3 film, the roughness profile can be obtained after applying a high-pass filter. The cutoff wavelength of the high-pass filter applied here is 0.039 μm, and the waviness profile obtained through applying a low-pass filter with the same cutoff wavelength to the primary surface profile is comparable to the primary surface profile. Fig. 5.5 (c) is the roughness profile along the red line marked in Fig. 5.5 (a). The presence of the nanoscale protrusions, as well as the rugosity along the line, lead to the distortion of the unevenness of the surface. The closer to these irregular areas, the rougher the surface would be. These nanoscale surface protrusions may result from the collapse of NP Al_2O_3 on the surface [123]. A B-spline smoothing filter is utilized to extract the roughness information from the line-scan roughness profile. Unlike a Gaussian smoothing filter, which has relatively obvious edge effects and large fluctuations [124], A B-spline smoothing filter can guarantee a better performance of the roughness evaluation and has been adopted as a standard to evaluate the roughness [125]. Some stipulated evaluation parameters, such as the roughness average (R_a), the root mean square roughness (R_q), and the average maximum height of the profile (R_z), are estimated based on AFM results, as 1.644 nm, 2.275 nm, and 16.18 nm, respectively.

Because AFM fails to easily provide comprehensive information on the NP Al_2O_3 film and is quite sensitive to the surface fluctuations, THz measurements are performed next in a non-destructive fashion to characterize the samples after electropolishing, the first, and the second anodization, with the reflected THz signals in Fig. 5.2 (d)-(f). The signal reflected from the electropolished Al substrate shown in Fig. 5.2 (d), is essentially the same as the reference signal because the Al substrate is highly reflective of THz radiation.

The reflected signals in Figs. 5.2 (e) and (f) are more complex. A typical signal reflected from the sample after the first anodization is shown in Fig. 5.2 (e). Due to the inhomogeneous surface of the NP Al_2O_3 films in the cross-sectional FE-SEM shown in Ref. [121], reflections occur from features of various heights within the frequency-dependent spot size

of the THz beam ($\sim$ 300 μm at 1 THz), resulting in a complex reflected pulse. Moreover, scattering (signal emitted in non-specular directions) is expected to be important due to the roughness, as we see below. We next turn to samples following the second anodization, for which the NP lattice is quite regular, and the surface morphology is flat. In this case, scattering is expected to be relatively weak. Four temporarily overlapped reflections of the incident reference signal (*i.e.*, echoes) are observed in Fig. 5.2 (f). The first positive echo corresponds to the air/NP Al_2O_3 interface and the second positive echo corresponds to the NP Al_2O_3/Al interface. The third and fourth echoes are the multiple reflection signals as THz waves propagate in the NP Al_2O_3 material, and the change of sign results from the phase shift as expected. The observation of the first two distinct echoes indicates that the two interfaces are smooth on the scale of the THz spot size and are well defined. The time delay between these two echoes and knowledge of the film's refractive indices enable us to measure the film thickness. This technique is known as time-of-flight technique (TOFT).

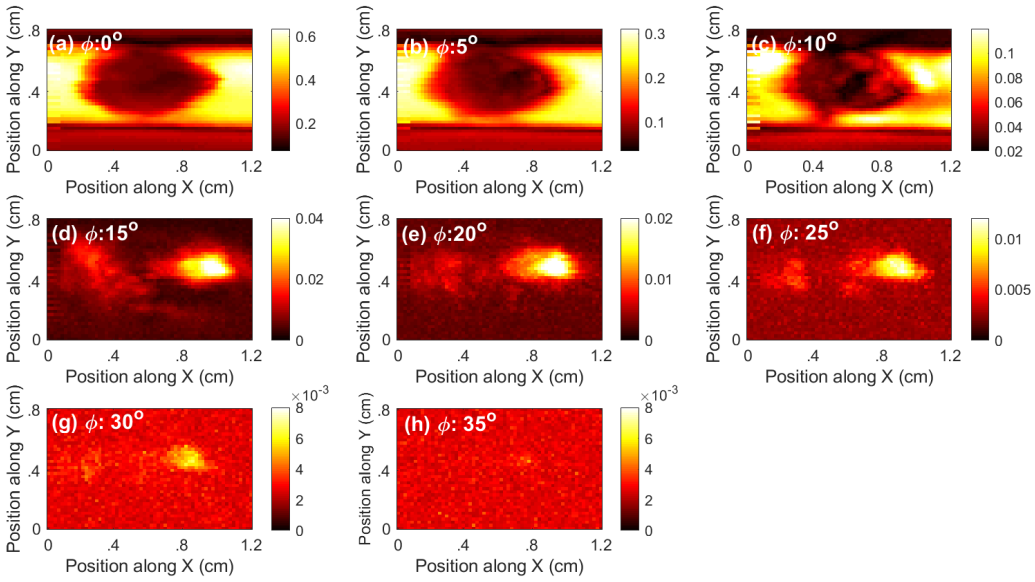

Figure 5.6: C-scans of the sample after the first anodization process for various reflection angles with the polarization angle $\sim$ 0° and incidence angle fixed (at $\sim$ 3°, *i.e.*, near-normal incidence). The contrast mechanism applied here is the maximum amplitude of the scattered signal.

As pointed out above, non-specular scattering is related to inhomogeneity. We explore

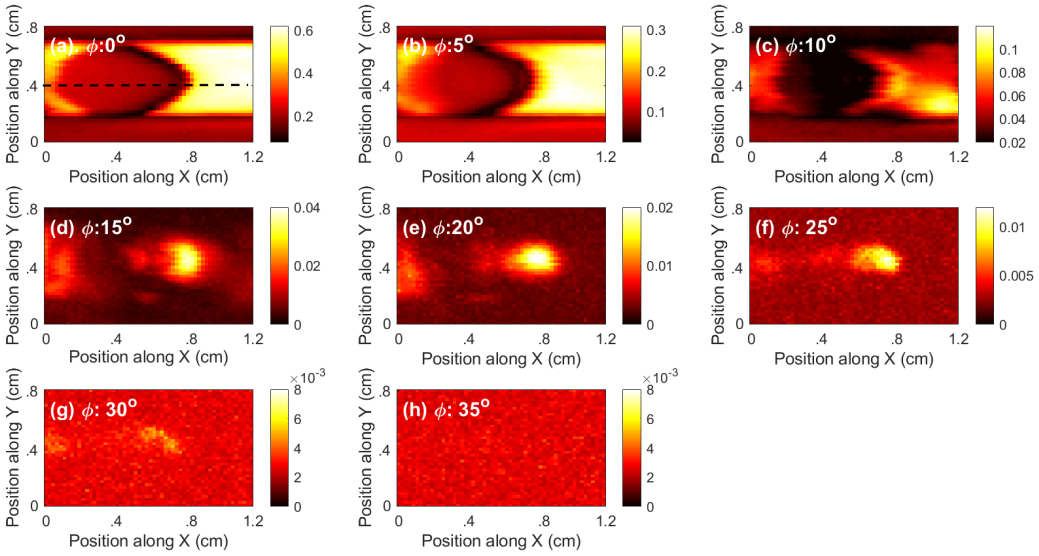

Figure 5.7: C-scans of the sample after the second anodization process for various reflection angles with the polarization angle $\sim 0°$ and incidence angle fixed (at $\sim 3°$, *i.e.*, near-normal incidence). The contrast mechanism applied here is the maximum amplitude of the scattered signal. The horizontal line at Y=0.4 cm, marked "Cross-section", is in reference to the B-scan in Fig. 5.17.

scattering by varying the scattering (detector) angle ϕ while fixing the incidence (emitter) angle near-normal incidence ($\sim 3°$). Corresponding C-scans of the NP Al_2O_3 films after the first and second anodization processes are shown in Figs. 5.6 and 5.7, where the contrast mechanism is the maximum amplitude of the scattered signal. The NP Al_2O_3 film lies only within a 1-cm diameter disk on the substrate, as presented in Fig. 5.8, while the remaining area is electropolished Al. Due to the beam divergence, to ensure a signal dominated by scattering, we need to choose $\phi > 10°$. For $\phi > 10°$, the strength of the scattered signal depends markedly on surface morphology. An inhomogeneous region between 0.7 cm and 1.1 cm in the *x*-, and 0.4 cm and 0.7 cm in the *y*- direction after the first anodization step, and position 0.6 cm and 1.0 cm in the *x*- and 0.3 cm and 0.6 cm in the *y*- direction after the second anodization, are clearly seen in Figs. 5.6 and 5.7. As ϕ increases further, the overall signal level falls significantly, as seen in Fig. 5.9. The increasingly mottled appearance of the C-scans with increasing ϕ is due to the decrease in the signal-to-noise ratio (SNR). When ϕ reaches 35°, the C-scan is dominated by noise.

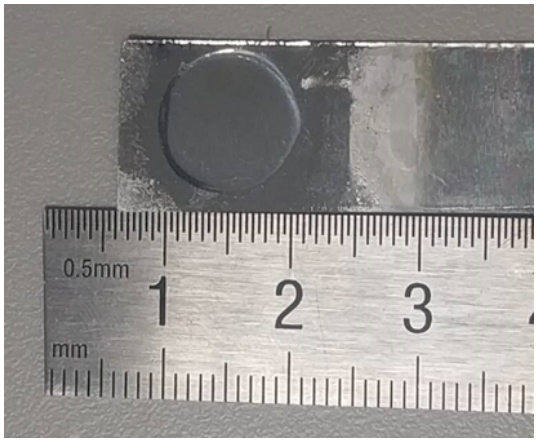

Figure 5.8: Real image of the Al foil after the second anodization process. One 1-cm diameter disk region of NP Al_2O_3 is found on the Al substrate.

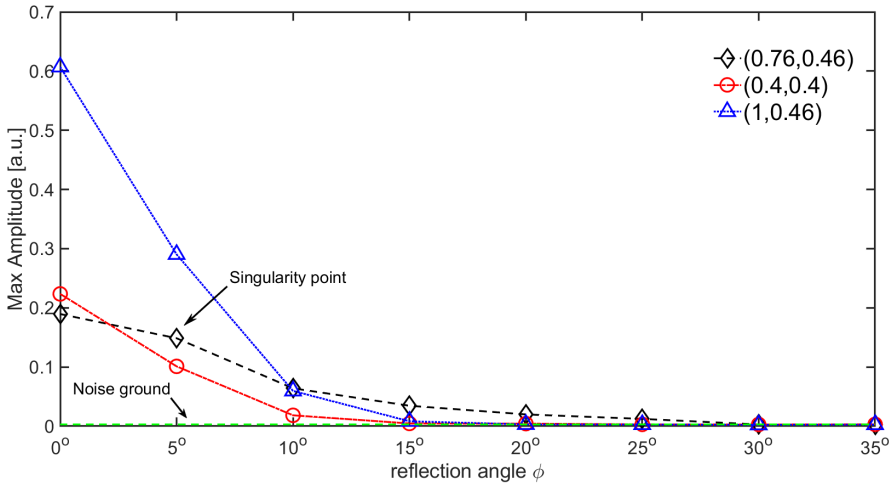

Figure 5.9: The maximum amplitudes of reflected THz signals from the sample after the second anodization at different positions *(x, y)* as a function of the scattering angle ϕ.

In order to investigate the surface morphology and nanopore arrangement of the disordered area, other additional measurements are applied subsequently. Because of the small view field of AFM, it is hard to provide a systematic investigation of the microstructure of the NP Al_2O_3 film and significant contrast at one time. Therefore, top view FE-SEM measurements are employed, and the corresponding result is displayed in Fig. 5.10. Compared with the FE-SEM result for the well-ordered area presented in Fig. 5.2 (c), there is a slight change in density, pore diameter, as well as inter-distance. These distortions contribute to the occurrence of non-specular scattering. The origin of the disordered area is worthy of

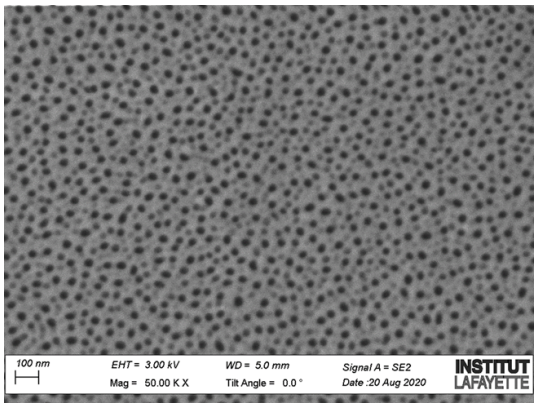

Figure 5.10: FE-SEM image at the disordered area.

study. Based on previous works on NP Al_2O_3 surface morphology, several tentative reasons are presented as follows. (1) Transfer of substrate-related nanoscale defects into the NP Al_2O_3 disturbs the NP array order [126]. (2) Because some pits and bumps persist on the Al substrate even after electropolishing, seen in Fig. 5.2 (a), those macro defects impact the formation of NP Al_2O_3 [127]. (3) Because the degree of NP order is largely determined by a certain value of anodizing potential, nonoptimal anodization parameters could lower the degree of pore order [128]. (4) Due to the long etching process ($\sim$6 h), etching during the first anodization process may be nonuniform, perhaps also connected to defects in the substrates as discussed above. Because of the complicated process of sample preparation, there is no consensus on the details of the roles of the above mechanisms. Indeed, it is likely that the answer depends on various aspects of the materials and processes employed.

5.1.2 Terahertz birefringence characterization of nanoporous Al_2O_3 films

Polarization-resolved THz reflectivity experiments are conducted to accurately obtain the polarization-dependent refractive index n and birefringence Δn of NP Al_2O_3 films. Optical microscopy at 50$\times$ of all films was first carried out (not shown) to understand the macro/mesoscopic nature of the surface after NP Al_2O_3 film growth. All samples evidenced surface striations aligned at $\sim 73^o$ with respect to the horizontal edges of the rectangular samples and are rolling marks; Al substrates are polycrystalline as evidenced by

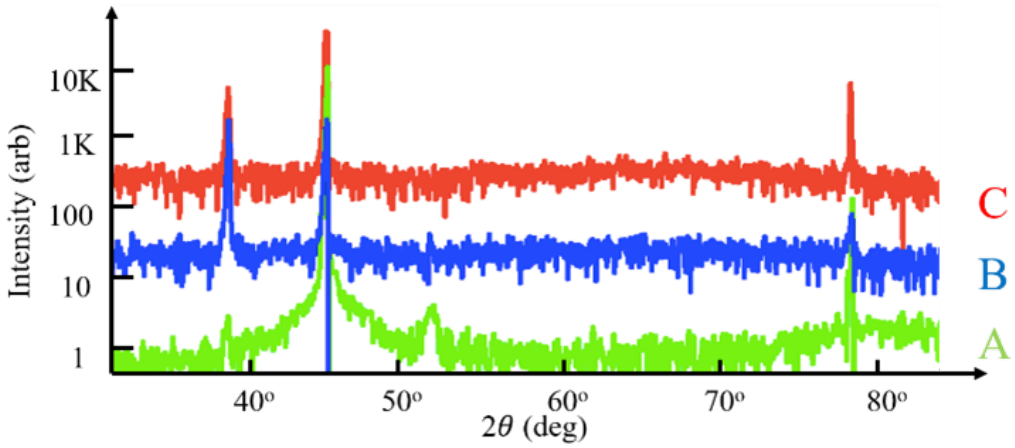

Figure 5.11: X-ray diffractograms of (A) Al, (B) first anodization Al_2O_3 films, and (C) second anodization Al_2O_3 films.

x-ray diffraction (XRD). Striation direction may be connected to Δn observed below. The crystal structure was examined first by x-ray diffraction (HR-XRD) (Panalytical X'pert Pro MRD with Cu Kα radiation in triple-axis mode); diffractograms of bare Al (sample 8), single (sample 1), and second anodization (sample 2) Al_2O_3 films are shown in Fig. 5.11. In all cases, peaks appear at $2\theta = 44.5°$ and $78°$ associated with the cubic Al substrate. After the first and second anodization, peaks occur at $2\theta = 38.5°$ indicating tetragonal Al_2O_3 [122]. The conducting Al substrates result in strong THz reflection [129]. This is also confirmed by the negligible polarization dependence of the reflections from sample 8. Figure 5.12 shows the polarization dependence of the reflected signals from $80°$ to $90°$ for sample 1, which was subjected only to the first anodization process. It is apparent that the first echo reflected from the top air/NP Al_2O_3/Al interface is broad and weak and is not readily distinguished from background noise. Cross-sectional FE-SEM of sample 1 (Fig. 5.14) shows a nonuniform 20-μm-thick NP Al_2O_3 top layer adjacent to air above a uniform 60-μm NP Al_2O_3 layer between the nonuniform NP Al_2O_3 top layer and the Al substrate. The top layer may result from heat generated on the surface of the electrolyte due to the high anodization voltage [130]. Because the air/NP Al_2O_3 interface is far from smooth within the transverse focus ($\sim$ 300 μm) and because of scattering at and within the

20-μm nonuniform Al_2O_3 top layer itself, a small first echo appears ahead of the strong echo reflected from the highly reflective NP Al_2O_3/Al interface.

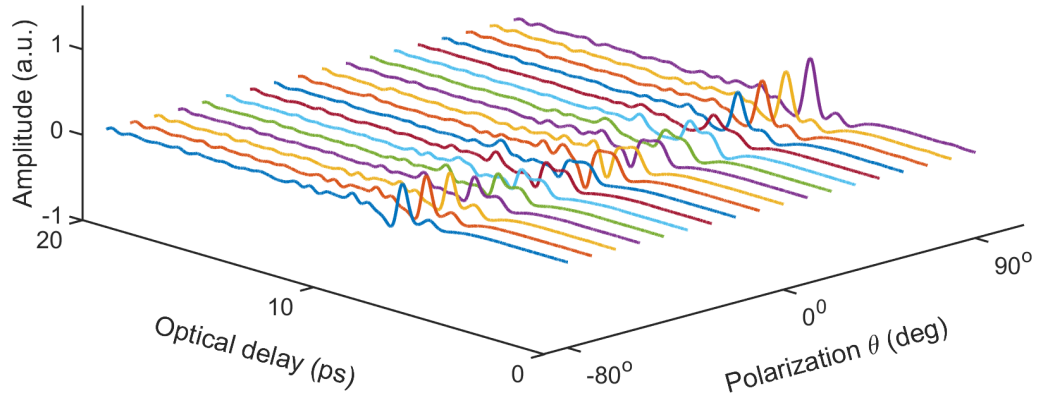

Figure 5.12: The reflected THz signal for various polarization angles for sample 1.

The second anodization results in a far more regular NP-lattice seeded by the first as shown in cross-section and top-view FE-SEM in Fig. 5.14. For samples 2-7 produced by second anodization, while the lattice constant is too small to resolve in THz images, THz polarization anisotropy is also expected. Figure 5.14 shows the reflected THz signals with various polarizations for sample 2, the results for which are representative of all samples produced by the second anodization. Owing to the relative smoothness of the top air/NP Al_2O_3 interface (height variation 45 nm from FE-SEM), scattering from this interface is negligible. Two positive echoes, the first corresponding to the THz signal reflected from the top air/NP Al_2O_3 interface and the second from the NP Al_2O_3/Al interface, are seen clearly. The time delay Δt between the echoes depends on the thickness $d_{Al_2O_3}$ and refractive index n of the NP Al_2O_3 film *via* $n = c \times \Delta t \,/\, (2d_{Al_2O_3})$; c is the *in-vacuo* speed of light.

We treat the NP Al_2O_3 film as an effective medium since the NPs are far smaller than the wavelength ($\sim$ 100 μm) in the usable THz bandwidth and neglect dispersion. Also, in order to assess n, we must begin with a sample having a larger known thickness d. The polarization-dependent refractive indices are shown in Fig. 5.15 along with a fit to $A\times\sin(2\theta+\varphi_1)+B\times\sin(6\theta+\varphi_2)+C$. The first term describes Δn, while the second term

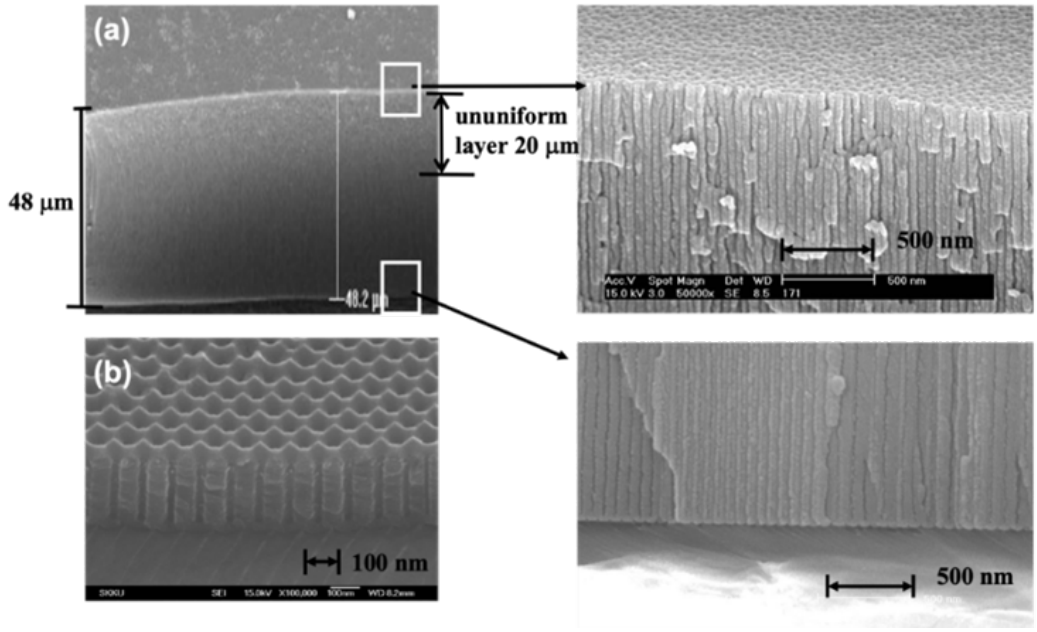

Figure 5.13: Cross-sectional FE-SEM image after the (a) first (sample 1) and (b) second anodization process. In (a) we see a relatively irregular lattice and a rough air/NP Al_2O_3 interface; (b) shows much greater regularity.

reflects any effect of the hexagonal lattice. We find A = 1.36 and B = -0.335 and conclude B is not significant; the polarization anisotropy does not appear to track the NP lattice. We find $\varphi_1 = 80^\circ$ for which the polarization is aligned parallel to the roll marks, and the ordinary refractive index is n_o = 3.5; the extraordinary refractive index is n_e = 3.2. Similar results are obtained for samples 3–7 that are also processed with second anodization. It is not clear if this similarity in directions is fortuitous or if the roll marks influence the optical properties of the NP Al_2O_3 films. In principle, n_o and n_e are obtained once the orientation of the respective axes aligns parallel to the incident THz polarization. Birefringence for the NP Al_2O_3 film can also be calculated based on the orientation of the optical axis, which is Δn = -0.3, close to the value reported for Al_2O_3 reported elsewhere [47, 131, 132]. (Although Δn was not studied in Ref. [132], refractive indices of Al_2O_3 in the THz range slightly larger than 3 were reported.)

The NP structure means that the films are a mixture of air and Al_2O_3. In Ref. [133], n of NP Al_2O_3 films was characterized in the visible and near-infrared regions of the spec-

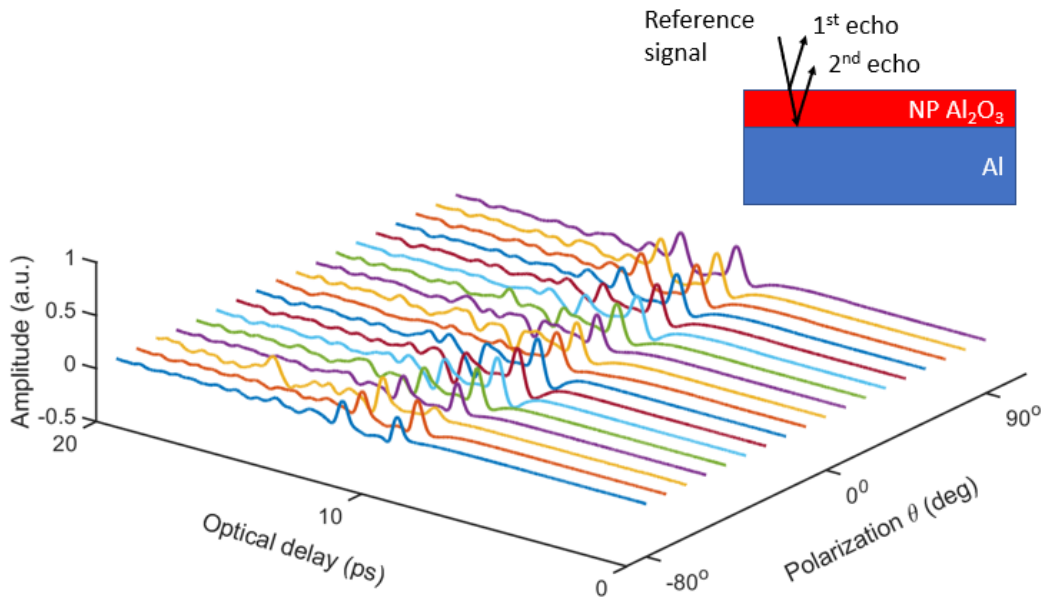

Figure 5.14: Reflected THz signal for various polarization angles for sample 2. Inset shows the origin of the two echoes in the reflected THz signal: one from the air/NP Al_2O_3 interface and the second from the NP Al_2O_3/Al interface.

trum. The films have air volume fill factors f from 4% to 22%. The measured values of n were significantly less than for bulk, and this was accounted for using the Maxwell-Garnett (MG) theory. For us, f = 9%. While the NPs and the NP lattice constants themselves are small on the THz wavelength scale, we do not expect appreciable photonic-crystal effects, suggesting that, neglecting Δn, the refractive indices should be well predicted by the MG theory. Neglecting Δn, for propagation along the axis of the air-filled holes (specular direction), the effective refractive indices of NP Al_2O_3 are $n_i = n_{i,Al_2O_3}[(1+\Gamma_i)/(1-\Gamma_i)]^{1/2}$, where $\Gamma_i = f(1-h^2_{i,Al_2O_3})/(1+h^2_{i,Al_2O_3})$ [133], where $i = ||, \perp$ and n_{i,Al_2O_3} is the refractive index of bulk Al_2O_3. Putting $n_{||,Al_2O_3}$ = 3.39 and $n_{\perp,Al_2O_3}$ = 3.07 [131], we find $n_{||}$ = 3.14 and $n_{\perp}$ = 2.85. Note, however, Δn = 0.29, which is close both to the value for bulk Al_2O_3 and to the value we measure.

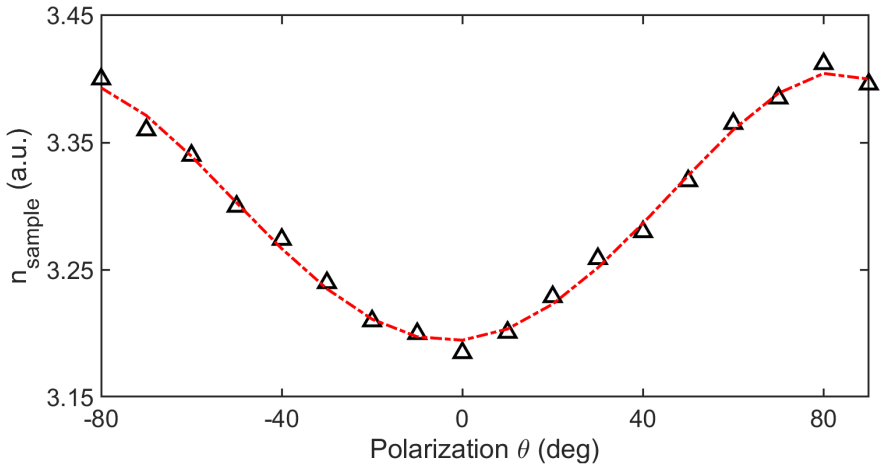

Figure 5.15: Calculated refractive index n of the NP Al_2O_3 film as a function of polarization for sample 2.

5.1.3 Structural characterization of nanoporous Al_2O_3 films

Next, the film thickness of samples 2–7 is measured next by reflective pulsed THz tomography. As mentioned above, the echoes arising from the air/NP Al_2O_3 and NP Al_2O_3/Al interfaces strongly overlap in time and cannot be visually distinguished. Deconvolution is essential to extract the time delay between the two echoes as well as to identify meaningful features in a background of noise. We use sparse deconvolution (SD), as described in Ref. [28]. The idea behind SD is that for a stratified medium, the impulse response function $h(t)$ is a sequence of peaks with zero in between; $h(t)$ gives the reflected signal expected with very short incident pulses; Δt, the time between successive peaks in $h(t)$, and n gives $d_{Al_2O_3}$ as discussed above. The sparsity assumption is thus additional information we have about the samples that supplement the measured reflected signal and enables us to extract the time delay, even if the corresponding optical thickness of the film is close to or somewhat below the axial resolution limit.

The reflected signal $r(t)$ from samples 2–7 with NP Al_2O_3 layers of various $d_{Al_2O_3}$ and the corresponding $h(t)$ reconstructed by SD are shown in Fig. 5.16. Two positive peaks are observed, the first corresponding to the position of air/NP Al_2O_3 interface and the second to the NP Al_2O_3 /Al interface. The amplitude of the second peak is larger due

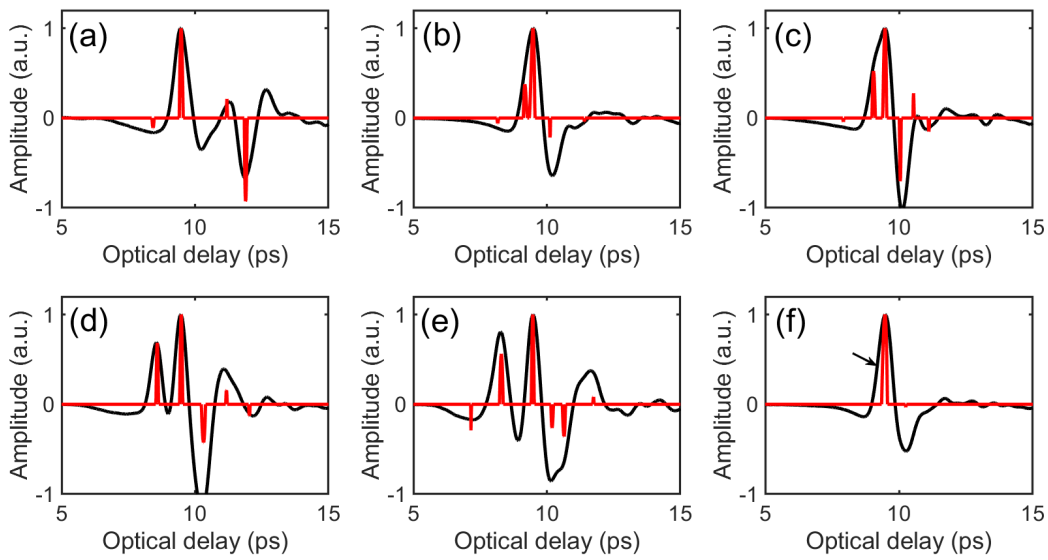

Figure 5.16: $h_{SD}(t)$ reconstructed by SD (red) and the reflected THz signal $r(t)$(black) for samples 2–7. The arrow in (f) indicates the position of the feature in $h(t)$ reconstructed from SD, associated with the air/NP Al_2O_3 interface.

to the strong reflection from the dielectric/metal interface. The optical delay between the two peaks can be used to estimate $d_{Al_2O_3}$. Even for sample 7, with $d_{Al_2O_3}$ = 12 μm, a weak peak arrow in Fig.5.16 (f) can be seen that overlaps with the strong peak due to the NP Al_2O_3/Al interface. As for sample 1, due to scattering and possibly dispersion, occurring in the 20-μm top nonuniform Al_2O_3 layer, the signal reflected from NP Al_2O_3/Al interface is weak and broad, thereby degrading the performance of SD.

The uniformity of the NP Al_2O_3 film thickness is also investigated among samples 2-7 by randomly selecting 20 pixels from the entire NP Al_2O_3 region, and with the minimum distance between two selected pixels 0.5 mm. Table 5.1 shows $d_{Al_2O_3}$ in samples 2-7. We see that the mean thickness agrees well with the value measured by destructive cross-sectional measurements. The low standard deviation indicates the high uniformity of the NP Al_2O_3 films as well as the robustness of SD and the stability of the THz measurement.

The stratigraphy of the well-ordered NP Al_2O_3 film can also be characterized based on THz B-scans along a cross-section using TOFT. Such a B-scan in Fig. 5.17 is along y = 0.4 mm as shown in Fig. 5.17. The narrow bright band near an optical delay $\sim$ 10

Table 5.1: The thickness of NP Al_2O_3 films (Samples 2-7). The first column is the nominal thickness of NP Al_2O_3 from the cross-sectional FE-SEM. The second and third columns (sampled at 20 random pixels) are obtained from relevant peaks in $h_{SD}(t)$. The low standard deviations confirm a high film uniformity as well as the robustness of THz-based estimates.

Sample	Nominal Film Thickness $d_{Al_2O_3}$ (μm)	Mean $d_{Al_2O_3}$ Measured by THz Tomography (μm)	Standard Deviation of $d_{Al_2O_3}$ Measured by THz Tomography (μm)
2	90	87	2.4
3	20	19.3	1.3
4	30	27.9	1.9
5	50	50.6	2.6
6	60	61.4	2.4
7	12	13.3	0.7

ps, corresponds to the top air/NP Al_2O_3 interface. In addition, the NP Al_2O_3/Al interface as well as the multiple reflections at later delays can be identified clearly. It is noted that the reflection from the Al substrate occurs later in the regions with the NP Al_2O_3 film than from where it is absent, which is expected due to the refractive index $n > 1$ of the film. Based on the optical delay Δt between the 1^{st} and 2^{nd} echoes, and the refractive index n of Al_2O_3 within the THz regime ignoring the air fill factors [47], which is $\sim$3, the Al_2O_3 film thickness is $c \times \Delta t$ / $2 \times n \sim 87\ \mu m$, with c the speed of light. This is in good agreement with the destructive cross-sectional FE-SEM. More detailed discussions on thickness characterization of NP Al_2O_3 films by sparse deconvolution can be found in Ref. [121].

5.2 Diagnosis of injection-molded weld lines in ABS thermoplastic by polarized terahertz reflective imaging

Injection molding is the most commonly used method to manufacture plastic parts, providing design flexibility and high-output production. Stagnating weld lines, one common defect in injection-molded thermoplastic products form where two separate melt fronts

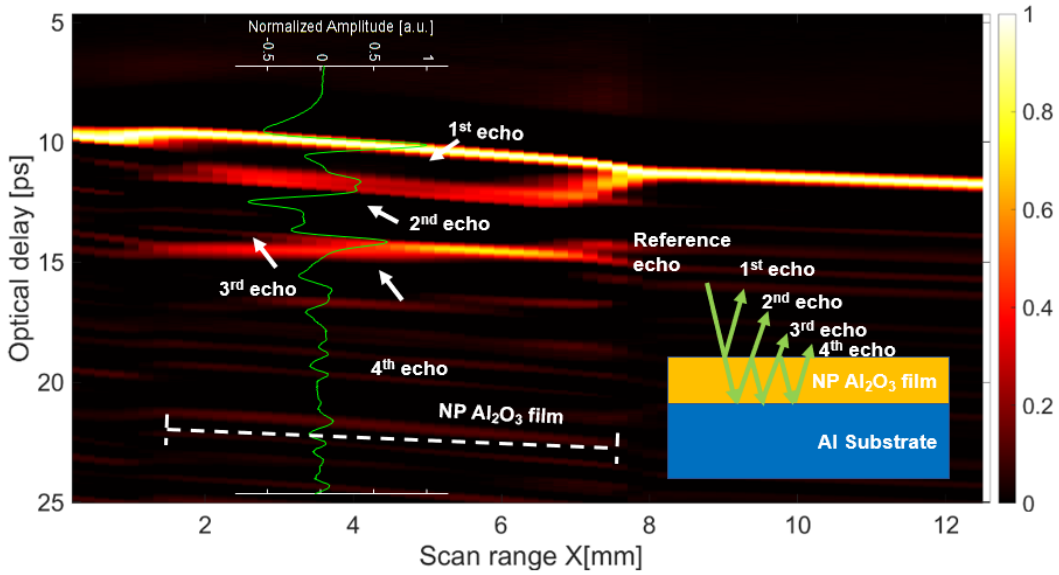

Figure 5.17: B-scan based on the raw data with the cross-section Y = 0.4 cm. Inset shows origin of echoes in reflected THz signal: 1^{st} air/NP Al_2O_3, 2^{nd} NP Al_2O_3 /Al, and 3^{rd} and 4^{th} multiple reflections.

impinge head-on after which there is no subsequent flow, as shown schematically in Fig. 5.18(a). Of practical concern, such surface defects degrade the mechanical properties and are places where the fracture or other failure is likely to occur [134, 135, 136, 137, 138]. Generally, the origin of the reduced mechanical strength at weld lines is molecular entanglement, the formation of V-notches at the weld surface, as well as the presentation of contamination at the weld interfaces. In order to guarantee the quality of fabricated injection-molded thermoplastic products, it is important to understand the geometry, morphology, and nature of melt flow at weld lines.

Injection-mold weld lines may or may not be easily identified by naked eyes or straightforward optical microscopy. The most common method for weld-line characterization is mechanical testing by means of a tensile or bend stage [139, 140]. The relative weld-line strength is defined as the ratio of the strength of specimens with a weld line and a comparable sample with the same geometry but without the weld line, and this measure mainly depends on the molding conditions, such as melt temperature, mold temperature, and injection pressure[141]. Even though these approaches provide qualitative and quanti-

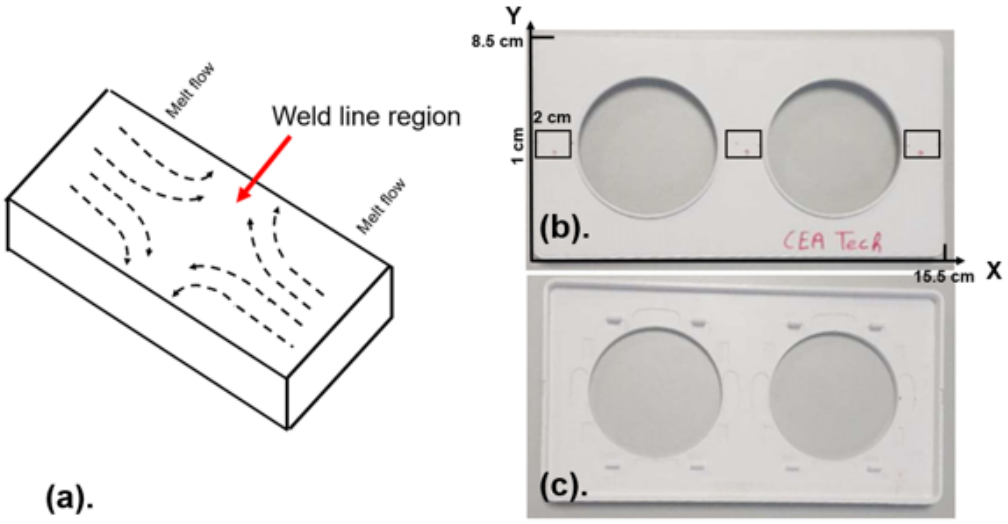

Figure 5.18: (a) Schematic diagram of the generation of a stagnating weld line due to fountain flow. Optical photographs of (b) front and (c) back surface of the injected-molded ABS thermoplastic electrical-receptacle plate. THz imaging and SAM are carried out within the three ROIs marked I, II, and III with the THz or acoustical signal incident from the front side. The injection-molded weld line runs horizontally through these three ROIs, and the small red arrow points to the weld location. Dimensions of the plate are 85 mm (vertical direction), 156 mm (horizontal direction), and 8 mm (maximum thickness).

tative information, they are restricted to certain geometries and, moreover, are destructive. x-ray computed tomography can also provide a three-dimensional reconstruction of the microstructure of weld joints, though x-ray induced damage may ensue after the measurement [142, 143]; moreover, x-ray measurement may engender significant health risk and is therefore not suitable for practical applications. Surface probes, such as atomic-force microscopy, suffer from limited scan area, relatively long scan duration, and may fail to provide sufficient information [144]. For scanning electron microscopy, the sputtering of a conductive gold layer limits the reuse of samples for other tests [141, 145]. As for conventional far-field ultrasound testing, the frequent requirement of a coupling medium may make the approach cumbersome and acoustic waves at the requisite frequencies ($\sim$ 10 MHz) for high resolution may suffer from high attenuation in thermoplastics [142, 146]. Therefore, alternative nondestructive evaluation (NDE) techniques for understanding thermoplastic injection-weld lines and for monitoring components in production are of interest.

In addition to surface morphological features at injection-mold weld lines in thermoplastic specimens, internal features might also be used for the NDE of such weld lines. For example, anisotropy might also be induced in the weld-line vicinity as a consequence of the rheological state of the melt flow. Typically, most amorphous polymer plastics at equilibrium are inherently isotropic and exhibit no birefringence. However, due to fountain flow [147, 148], a combination of shear and elongational flows, the melt-flow fronts are subjected to shearing flow during the mold filling process, which leads to the increase of elasticity and preferential molecular orientation proximate to the weld line, and the formation of complex anisotropic structure at the weld line of the injection molded parts after cooling [149]. The solidification of melt flows leads to frozen-in anisotropic stress and molecular orientation in injection-molded plastics, which in turn can induce the reduction of the mechanical strength when the forces are applied perpendicular to the weld line [150, 151]. The degree of orientation can be quantified by the birefringence index. In Ref. [152], optical birefringence distribution along the flow direction of injection-molded thermoplastic specimens has been investigated through a photo-elasticity method. The influences of the temperature distribution and shear-rate field within various areas near a weld line during the injection molding affect birefringence have been studied using Z-MOLD analysis software, which is an integrated computational simulation suite for injection-molded products [153]. The local anisotropic stresses specifically proximate to injection weld lines have not, however, been as extensively studied experimentally. Such spatially dependent anisotropy could also provide a contrast mechanism for various NDE techniques to validate and characterize the presence of injection-mold weld lines even when such weld lines are not easily identified visually. In particular, detecting the weld-line location, understanding their spatial extent, and gaining insight into local anisotropy could be used to optimize the manufacturing processes that avoid the reduction of weld strength of fabricated injection-molded thermoplastic products.

In this study, polarization-resolved THz reflective imaging and scanning acoustic mi-

croscopy (SAM) are utilized to characterize injection-mold weld lines in an Acrylonitrile Butadiene Styrene (ABS) thermoplastic electrical receptacle plate. Figure 5.18 (b) and (c) show the injection-molded component, with dimensions 156 mm $\times$ 85 mm $\times$ 4 mm (at rim), studied here. It is an ABS thermoplastic electrical receptacle plate produced by Schneider Electric (S520704 Odace 2-gang electrical receptacle plate). ABS is a common thermoplastic used in a host of electrical, decorative, structural, medical, and consumer applications due to its impact resistance, toughness and chemical stability. Besides, ABS is amorphous and may have a range of compositions; the specific values for the component studied here are unavailable. In general, ABS is a two-phase material mixed with a styrene-acrylonitrile copolymer with polybutadiene. A two-gate injection mold was used to fabricate this component showing symmetry along the long axis. The processing condition of the injection molded parts, including melting temperature, melting speed, and mold temperature, are unavailable. The injection-mold line runs horizontally through the three rectangles indicated in Fig. 5.18 (b), which shows the front of the plate (decorative side). Figure 5.18 (c) shows the back of the plate (facing the electrical box).

5.2.1 Terahertz characterization

We are unable to sense the weld-line by touch or to see it with the unaided eye. We, therefore, imaged the electrical receptacle plate in the weld-line region at 50 $\times$ by optical microscopy [Axio Scope.A1 Microscope (Zeiss)]. No weld-line defect was easily identifiable under the optical microscope. Moreover, due to the irregular shape, it is hard to achieve a good focus on the surface of the thermoplastic specimen without cutting. We also conducted tensile testing for failure on nominally identical receptacle plates. In most cases, macroscopic fracture initiated at the same positions, *i.e.*, the weld lines, which are known to be common sources of mechanical failure in injection-molded thermoplastic components.

THz imaging in reflection mode from the front (decorative) side was conducted first to characterize the surface morphology of injection-molded plastic samples. Owing to the

symmetry of the receptacle plate along the horizontal axis and the location of the input ports for the injected flows, the weld lines are expected to be located horizontally within the regions of interest (ROI) marked I, II, and III in Fig. 5.18 (b). The dimension of the ROI we investigated is 1 cm and 2 cm, respectively. Based on the set experimental parameters as well as the scanning area, the duration can be calculated, which is ~ 2 hours. By monitoring the arrival time of the peak of the reflected THz signal as a function of position across the ROIs, we obtain a measure of the surface morphology of the front side. That is, if the peak of the reflected signal arrives later in some area, the surface there is indented compared with surrounding areas due to the additional time of flight involved to receive the main feature of the reflected signal. In other words, the additional time delay Δt in receiving the signal, gives the relative local depth of the surface $d = c \times \Delta t/2$. Here, c is the *in vaccuo* speed of light and the factor of 2 in the denominator accounts for the additional time for the peak signal's round trip.

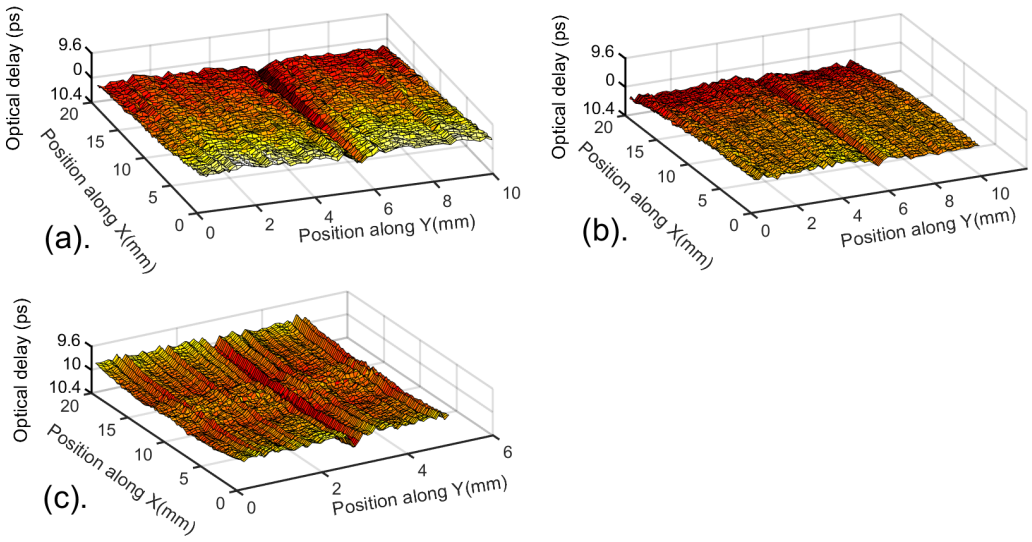

Figure 5.19: THz C-scans in ROI (a) I, (b) II, and (c) III are based on the peak reflected signal arrival time as the contrast mechanism. The V-shaped notch surface morphological feature at the weld line can be seen clearly for all ROIs. The transverse spatial step size is 200 μm. The notch width and depth are approximately 400 μm and 10 μm, respectively.

C-scans (two-dimensional presentations of components) based on this contrast mechanism, corresponding to the air/injection-molded plastic sample interface, are plotted in Fig.

5.19. The THz polarization was first set to 0°, defined to be parallel to the horizontal weld line. In all three ROIs, we detect a V-shaped notch at the presumed weld-line locations, which is perpendicular to the direction of melt flows meeting at the center of the thermoplastic electrical receptacle plate. The surface morphology of the V-shaped notches can be estimated based on the arrival time of the echo reflected from the surface of the thermoplastic as discussed above. We obtain values for the notch width and depth of $\sim 400\ \mu m$ and $\sim 10\ \mu m$, respectively, based on the THz C-scans of Fig. 5.19. The width and depth of the notch extracted from the THz measurement are limited by the applied experimental parameters, such as the transverse resolution ($\sim 300\ \mu m$), the spatial step size in rastering the sample ($200\ \mu m$), and the sampling frequency (~ 0.0116 ps). The use of SAM, which can provide $\sim 3.5\ \mu m$ transverse resolution at center frequency at 420 MHz to validate the THz measurements, is discussed below. Here we note that we attempted atomic-force microscopy to verify the surface morphology, but due to the irregular sample geometry (of the back of the plate) and its size, vibrations rendered these measurements fruitless.

There are several plausible sources for the formation of V-shaped notches at injection-mold weld lines. One is poor bonding due to insufficient time prior to solidification for the polymer molecules to diffuse across the interface. Another is frozen-in molecule orientation, which is preferentially parallel to melt flow and ends up being parallel to the weld line. Others include anisotropic shrinkage near the weld during cooling [154], air entrapped at the interface between the flow fronts [155], or the poorly bonded region near the surface in combination with the large shrinkage due to the high molecular orientation [156]. Because of the absence of detailed information on the fabrication procedure of this thermoplastic receptacle plate, we can only provide these plausible, though tentative, explanations. The measurements discussed above of the surface morphology show negligible dependence on the THz polarization. The bulk internal properties of the thermoplastic, however, show significant polarization dependence as is now discussed.

Broadly speaking, optical birefringence is known to provide a sensitive probe of molec-

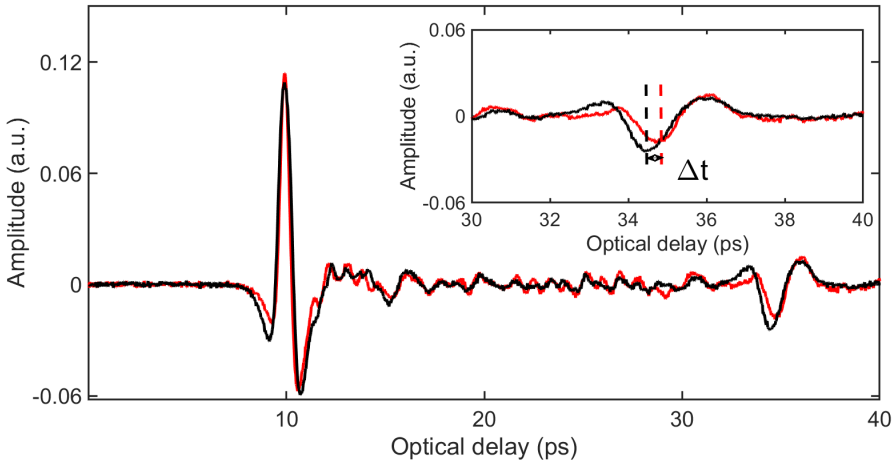

Figure 5.20: Typical reflected THz signals from the expected weld line in ROI I with polarization perpendicular (red) and parallel (black) to the injection-mold weld line. The first echo at an optical delay $\sim$ 10 ps is due to the reflection at the top air/plastic interface; The second echo at $\sim$ 35 ps is due to the reflection from the back plastic/air interface. Note that the arrival time of the second echo depends on polarization as is seen more clearly in the inset. The polarization-dependent time delay between the first reflected peak and the reflection from the back plastic/air interface is indicative of the polarization-dependent refractive index of the material near the weld line.

ular orientation and residual stress in amorphous polymer injection plastics [150, 152, 157, 158], and can also be treated as a microscopic structural feature as well as the anisotropic manifestation of injection-molded thermoplastic products. The component understudy is optically opaque, so THz birefringence arises as a candidate to probe the internal structure near the weld lines. Figure 5.20 shows typical reflected THz signals close to the weld for THz polarization perpendicular (red) and parallel (black) to the weld line. Each reflected signal shows a pronounced first echo (near optical delay 10 ps) from the air/plastic interface (decorative side) followed by ringing (due to noise, atmospheric H_2O, and after-pulses in the photoconductive emitter). At $\sim$ 35 ps, we observe a weaker echo originating from the back plastic/air interface. The sign of the second echo is negative, as expected since the refractive index of air is less than that of the plastic. The inset shows a slight difference in arrival time of the second echo for the two polarizations with the echo arriving Δt earlier for perpendicular ($\perp$) polarization with respect to the case of parallel ($\parallel$) polarization, indicating that the refractive index $n_\perp$ for the former polarization is slightly larger than

that $n_{\parallel}$ for the latter polarization. The polarization-dependent refractive index is attributed to the variation of local density and melts flow direction due to the fountain flow (from perpendicular to the weld line to parallel to the weld line, shown in Fig. 5.18 (a)) [49]. The values of refractive indices at different polarizations can be obtained from $w = c \times T_i / (2 \times n_i)$ where w is the thickness of the receptacle plate at the location measured, c is the *in vaccuo* speed of light, T_i is the time delay between the first and second echo in the reflected signal for polarization $i = \perp, \parallel$, n_i is the refractive index for polarization i, and the factor of 2 in the denominator is due to the fact that the reflected signal passes through the plate thickness w twice. Calliper measurement of the plate thickness at the location measured on the weld line gives w = 1.6 mm. We thus find the values $n_{\perp}$ = 1.7277 and $n_{\parallel}$ = 1.693 giving THz birefringence Δn ($|n_{\parallel} - n_{\perp}|$) = 0.035. We neglect the effects of THz dispersion, which are relatively weak in thermoplastics [103]. In general, the variation of the refractive index for different polarizations might result from the change in position of the preferential molecular orientation. During mold filling, molecular chains at the melt front are stretched parallel to the weld line as a result of this flow, and the initial orientation begins to freeze in from the surface. Because the molecules in the interior have more time to relax their orientations before they are frozen, the molecular orientation might be partially relaxed during solidification. The remaining frozen-in molecular orientation affects the tensile strength of the weld line, as well as the THz birefringence [135]. Moreover, the variation of the mechanical density near the weld line will also influence the refractive index n, even though it is difficult to quantify the spatial dependence [159].

To study the birefringence Δn and its spatial dependence in more detail, we measure the refractive index n as a function of polarization angle θ with respect to the weld-line direction in ROI I. Because the THz polarization angle is fixed, the THz time-domain waveforms, according to different θ, are measured by rotating the injection-molded component placed on the focal plane. Figure 5.21 shows the polarization dependence of n at the weld line where the dotted black curve is a fit of the data to $A \times \sin(2\theta + \phi_1) + B$; The Root Mean

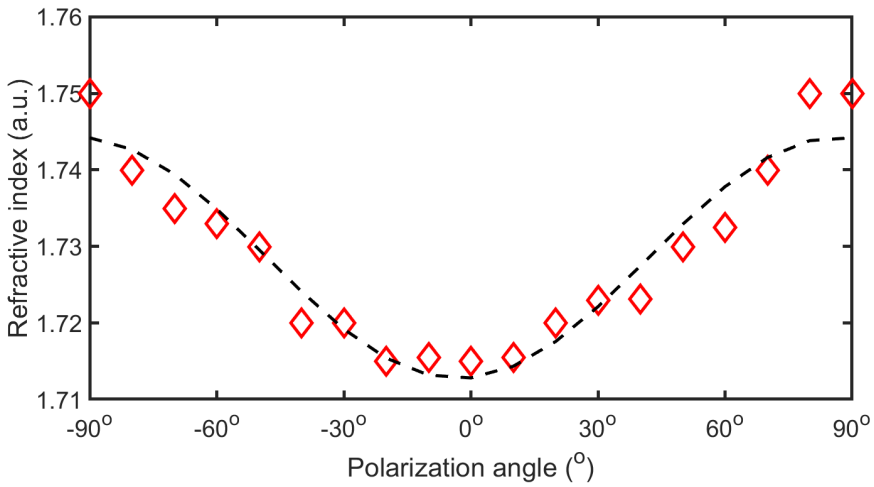

Figure 5.21: The THz refractive index n at the weld line as a function of polarization. $\pm 90^{\circ}$ and 0° correspond to polarization perpendicular and parallel to the weld line, respectively. Birefringence Δn = 0.035. The corresponding RMSE is 0.003787.

Square Error (RMSE), a standard approach of evaluating the distribution of the residuals, is calculated to assess the fit quantitatively. A small RMSE, which is 0.003787, shows an excellent correlation between the measured values and fitting results. The polarization-dependent refractive index n achieves its minimum at $\theta = \sim 0^{\circ}$ corresponding to $n_{\parallel}$ and its maximum at $\sim \pm 90^{\circ}$ corresponding to $n_{\perp}$. We then investigated Δn in ROI I, but $\sim$ 1mm away from the weld line as presented in Fig. 5.22. In this case, Δn = 0.0087, less than half that on the weld line itself, demonstrating that the degree of anisotropy decreases while moving away from the weld line. Similar results (not shown) are found in ROI, II, and III.

The tentative explanation of these results is that, at the weld line, the flows result in a preferred frozen-in molecular orientation and/or stress field parallel to the weld line. As one moves away from the weld line over a certain length scale, Δn tends to be zero as the ABS tends toward an isotropic state [149, 160]. We expect that this distance depends on the flow and cooling rates as well as the composition. Such spatially dependent anisotropy and morphological features could provide contrast mechanisms for various NDE techniques to detect the presence of and characterize injection-mold weld lines.

To verify that indeed this pronounced variation in Δn is connected with the weld line,

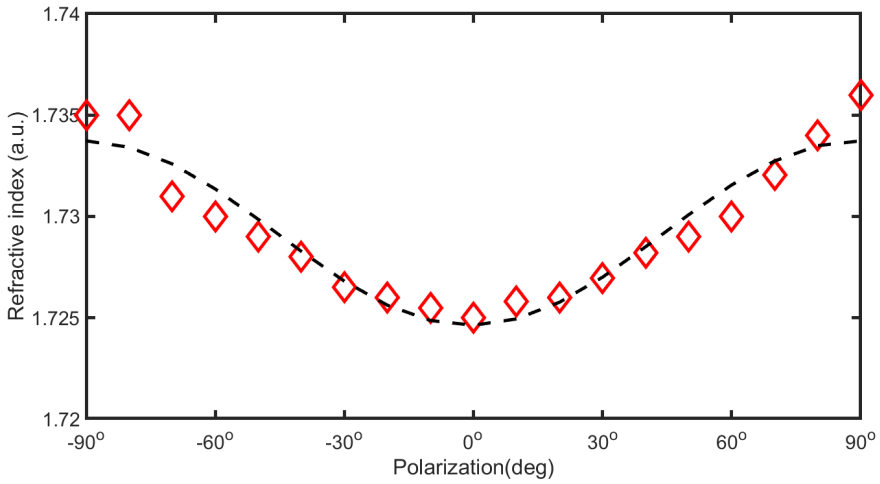

Figure 5.22: THz refractive index n 1mm away from weld line as a function of polarization. -90°(90°) and 0° correspond to polarization perpendicular and parallel to the weld line, respectively. Birefringence Δn = 0.012. The corresponding RMSE is 0.001287.

in Fig. 5.23 we plot Δn as a function of position along a section perpendicular to the weld in ROI I with d = 6 mm corresponding to the weld. A Gaussian fit to the data is shown as a guide to the eye. We see that the enhanced THz birefringence is localized around the weld and is gradually decreasing on the length scale of 2 mm with distance from the weld. The weld lines in ROIs II and III show similar behaviours.

5.2.2 Scanning acoustic microscopy characterization

Another NDE technique that can provide insight into the weld line is scanning acoustic microscopy (SAM). In addition, we wish to validate our interpretation of the THz results by independent measurements. SAM is of interest to ascertain the effects of the welding process on the visco-elastic properties and to visualize the micro-elastic spatial variations near the weld lines. SAM is an established choice for the quality control of industrial products and for health monitoring, quality control, and troubleshooting [161, 162, 163, 164]. It enables the non-invasive and non-destructive assessment of the micro-elastic properties of objects with a high spatial resolution when a focusing piezoelectric transducer (acoustic lens) is utilized at ambient temperature using water as a coupling fluid [165].

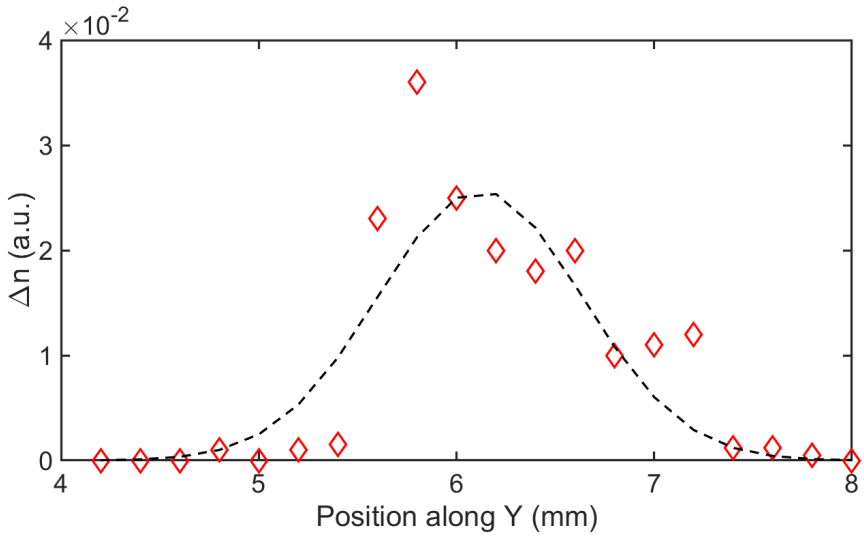

Figure 5.23: Birefringence Δn along a section perpendicular to the weld line. The maximum value of Δn occurs at the weld line, indicating a local enhancement of the molecular orientation parallel to the line and frozen-in anisotropic stress. The corresponding RMSE is 0.005507.

The acoustic microscope utilized in this study (ELSAM, Ernst-Leitz Scanning Acoustic Microscope; PVA TePla Analytical Systems, GMBH, Deutschordenstrasse 38, 73463 Westhausen, Germany) operates in reflection mode. A piezoelectric transducer mounted on the back surface of an acoustic lens receives a short RF pulse (approximately 10–30 ns in duration) and converts it into mechanical waves. The acoustic waves propagate through the sapphire rod and are focused sharply by the spherical cavity of the lens into a diffraction-limited point in the interface between a coupling fluid and the sample. The signal reflected at the different interfaces is collected back by the same transducer and converted into an electric signal. An image is then formed by scanning in two dimensions and processing the reflected signal into a greyscale map.

The contrast in SAM is based on the acousto-mechanical properties of the sample. The amplitude reflection coefficient under a plane wave assumption from medium i to j is

$$R = \frac{Z_i - Z_j}{Z_i + Z_j} \tag{5.1}$$

where $Z_{i,j} = \rho_{i,\,j} V_{i,\,j} / \cos\theta$ is the acoustic impedance of medium i, j of mass density $\rho_{i,j}$ and acoustic velocity $V_{i,\,j}$, with θ the angle of incidence. $V_{i,\,j}$ is related to the bulk

and shear moduli, and consequently to Young's modulus of elasticity for a material with a constant Poisson's ratio.

For the work presented here, SAM with a center frequency of 420 MHz was employed to achieve sufficient resolution to probe anomalous acousto-mechanical and morphological behaviour close to the weld lines. The lateral resolution of SAM that operates at a center frequency of 420 MHz is close to 3.5 μm at room temperature, which is much smaller than the spatial step size we employed (100 μm). In that sense, SAM has a much higher spatial resolution than the THz-based approach. SAM also allows us to overcome resolution difficulties that arise in standard far-field ultrasonic approaches.

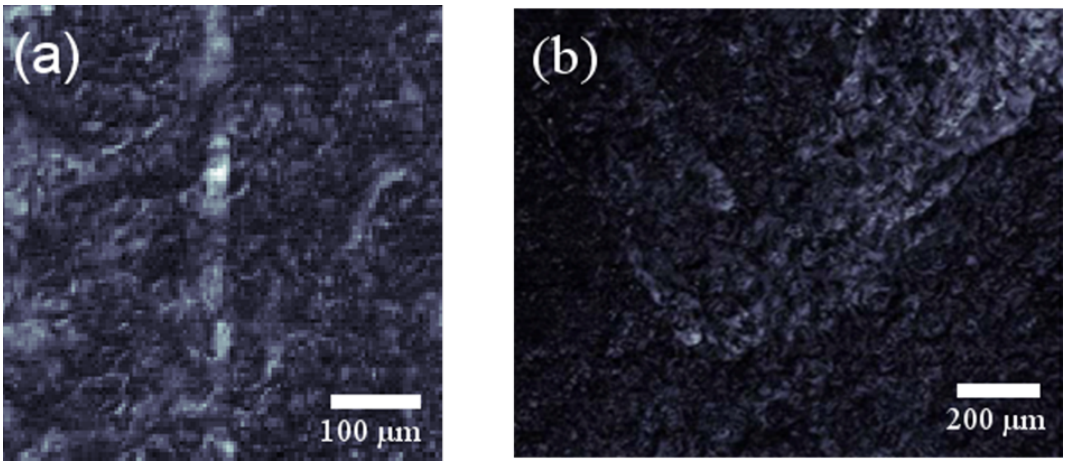

Figure 5.24: (a) SAM micrograph of region I of Fig 5.18 (rotated by 90° with respect to Fig. 5.18). The vertical whitish feature is the weld line; irregular flow patterns and surface heterogeneity are also evident. (b) SAM micrograph of a morphological deformation on the surface of the mold about 1 mm distance from the weld line. Surface heterogeneity is also observable.

From the SAM image of ROI shown in Fig. 5.24 (a), a weld line with heterogeneity in the microstructure with respect to the mechanical properties and flow patterns is detectable, as was also reported in Ref. [159]. The estimated width of the weld line is $\sim$ 500 μm. In Fig. 5.24 (b), morphological deformations on the surface of the mold about 1 mm distance from the weld line are observed at the weld, which may be linked to the thermal effects followed by solidification of the mold during the injection molding process. Similar structures are also found in ROIs II and III.

In addition to the observation of the morphological features at the weld line, SAM imaging offers contrast depending on spatial variation in the viscoelastic and mechanical properties, hence, the complementary nature of this technique with THz imaging. In the magnitude-contrast acoustic microscopy images, shown in Fig. 5.24 (b), surface heterogeneity, mainly associated with the reflectivity but also to some degree with the attenuation, can be assessed. Variations in ultrasonic reflectivity are connected to local variations in the mass density, elastic moduli (bulk compression, shear, and Young's), or both. Variations in the attenuation, attributed to absorption and/or scattering, are associated with local variations in the viscous properties. Moreover, the mechanical properties appear to show local differences near the weld line, compared with areas away from the weld, verifying the spatial-dependent refractive index presented in the THz measurements, because the refractive index tends to be higher in a denser medium. Anisotropy also contributes to the contrast [166], as the orientation of fibers in mold polymers was reported to be different within an area close to the weld lines, consequently the spatial variations in the velocities of the different polarizations result in a corresponding variation in the reflectivity; however, probing directional dependencies caused by anisotropy can be done with SAM only when using a cylindrical acoustic lens, which was not the case in this research.

To conclude this section, THz imaging has demonstrated its ability to detect the presence and spatial extension of anomalies associated with injection-mold weld lines in the nominally amorphous thermoplastic ABS, and the corresponding THz results are supported by SAM measurements and mechanical failure tests. This work suggests that THz techniques may provide useful means to characterize and locate injection-weld lines in thermoplastic components and potentially this information can be used to improve manufacturing and for the NDE of components on the production line and in service.

5.3 Terahertz dielectric characterization of low-loss thermoplastics for 6G applications

Great effort is underway to deploy commercial fifth-generation (5G)–and to develop future sixth-generation (6G)–networks. The 5G spectrum is limited above 100 GHz; however, 6G extends the upper frequency to 3 THz. Applications such as artificial reality (AR), real-time super-resolution imaging, autonomous driving, smart city, and the internet of things will benefit from 5G deployment, but more so from 6G systems. At every level, choices will need to be made concerning materials–from the device level to microelectronics packaging to handheld device packaging to building metasurfaces for reflectors and filters. Glasses, ceramics, and semiconductors have been investigated for high-index THz materials [167, 168, 169]; however, with high index typically comes high losses for disordered materials. For waveguides and transmission lines, high-index media may be desirable. A low refractive index, though, is also of interest to enhance radiation efficiencies that are otherwise suppressed due to substrate coupling [170]. Our focus here is on selected low-cost and common plastics for their low-loss/low-index properties in the 6G band for microelectronics packaging and other high-frequency applications.

Thermoplastics provide a wide range of materials choice. The THz dielectric properties of several polymers have been investigated previously [45, 51, 88, 29, 9, 116, 117, 171, 172, 173, 174], For example, Polytetrafluoroethylene (PTFE) is often used for THz lenses and windows [172, 174]. Our focus here is on three common and inexpensive plastics, *namely*, polycarbonate (PC), polymethyl methacrylate (PMMA), and acrylonitrile butadiene styrene (ABS), though many other materials are readily available. Despite past THz characterization of plastics, there are not many measurements in the literature on these specific materials covering the same frequency band. Moreover, some of the measurements are up to two decades old, while the sample-to-sample variability of many plastics calls for more measurements. These materials are of interest not necessarily for microelectronics

packaging, but for packaging of entire handheld devices or systems or providing low-cost windows to enable high transmission of signals. When it comes to various applications, other considerations will also come into play, including moisture absorption, poor thermal conductivity, and poor thermal and chemical stability of many plastics. In addition, ultra-smooth surfaces may not be readily attainable. Still, plastics remain attractive choices for situations where low cost is important and exposure to demanding environments may not be an issue. In other words, ultimately, materials choices for deployment in the field will require tradeoffs.

The literature related to the THz dielectric properties of materials is vast but scattered. The specific 6G context in this regard, however, has attracted limited attention, while much of the discussion that does exist concentrates on microelectronic packaging with little consideration of applications related to packaging entire handheld devices or subassemblies. In Refs. [175, 176, 177], polymer films were laminated on both sides of the glass substrate to explore the use of this stack up as a microelectronics substrate and to fabricate waveguides and transmission lines. Loss tangent $\tan\delta \approx 0.01$ were measured in the 50–140 GHz range, barely touching the 6G band. Such structures are of interest for microelectronic packaging applications for 5G, and likely for 6G. It is important to note, however, that the dielectric properties of materials in the THz regime are quite different from DC, microwave, and optical-frequency values, necessitating actual THz measurements.

Mass-produced thermoplastics vary widely insofar as polymer-chain length, chemical purity, degree of crystallization, density, degree of preferential molecular orientation, incorporation of frozen-in stress, and tacticity (for certain polymers). Surface texture also affects measured losses and varies widely depending on the manufacturing conditions and surface treatment. It is not our aim here to provide precise values for ultrahigh purity materials prepared under controlled conditions, but to give representative values for off-the-shelf materials. As mentioned above, for applications such as packaging entire handheld devices or subassemblies and windows, low cost and no requirement for a long lifetime may drive

interest in these plastics.

In this study, a systematic characterization of the dielectric properties of three frequently used, low-cost, and off-the-shelf thermoplastics using a commercial THz TDS system over a broad frequency ν range from 0.5 to 2 THz, is presented. The frequency-dependent refractive index $n(\nu)$, attenuation coefficient $\alpha(\nu)$, complex permittivity $\varepsilon(\nu)$, and loss tangent $\tan\delta(\nu)$ of PC, PMMA, and ABS are calculated and compared. These characterized materials present a low refractive index (compared with glass and many crystalline materials) and low loss.

The transmission measurements were performed using a commercial pulsed broadband THz TDS system (TPS Spectra 3000 from TeraView Ltd.). Compared to vector network analyzers (VNA), another instrument employed in Ref. [177] to measure the dielectric properties of materials in the fifth-generation (5G) band, the higher frequency resolution thus enabled, is of little interest due to the rather featureless nature of $\varepsilon(\nu)$ in the THz band [167, 178]. The system produces quasi-single-cycle THz pulses at a repetition rate of 100 MHz. The detection is capable of mapping out the amplitude of the THz electric field in time subsequent to propagation through the plastic sample. The effective bandwidth of THz pulses generated by our THz system is from 60 GHz to 3 THz. Because of the low signal-to-noise ratio (SNR) after interacting with the sample at the extreme ends of this band, however, only $\nu \in$[0.5 THz, 2 THz] is used for the analysis. Note that we measure the full time-dependent electric field of THz signals, *i.e.*, we obtain full amplitude *and* phase information. A flow of dry N_2 was introduced into the propagation path during the measurements to suppress atmospheric water-vapor absorption. The frequency resolution for this setup is $\sim$6 GHz and 1800 scans were collected and averaged to eliminate random amplitude fluctuations in the femtosecond mode-locked laser and photoconductive THz source. Balancing the noise level in the spectrum as well as the spectral resolution, a Black-Harris 3-term apodization was utilized to suppress apparent noise in the spectrum.

The frequency-dependent refractive index $n(\nu)$ and attenuation coefficient $\alpha(\nu)$ of the

plastics are obtained from the measured time-dependent electric field after Fourier transforming the time-domain signal (electric field) transmitted through the sample and through the air (reference signal), with electric-field amplitude and phase $E_s(\nu)$, $\phi_s(\nu)$ and $E_r(\nu)$, $\phi_r(\nu)$, respectively [111],

$$\alpha(\nu) = -2/d \ln[E_s(\nu)/(T(\nu)E_r(\nu))], \tag{5.2}$$

$$n(\nu) = 1 + c[\phi_s(\nu) - \phi_r(\nu)]/(2\pi\nu d) \tag{5.3}$$

where d is the sample thickness and $T(\nu)$ is the transmittance associated with the air/plastic and plastic/air interfaces,

$$T(\nu) = 4n(\nu)/[n(\nu) + 1]^2 \tag{5.4}$$

Furthermore, the complex permittivity $\varepsilon(\nu) = \varepsilon' + i\varepsilon'$ and loss tangent $\tan\delta(\nu)$ are related to $n(\nu)$ and $\alpha(\nu)$ by

$$\varepsilon' = n^2 - k^2 \tag{5.5}$$

$$\varepsilon'' = 2nk \tag{5.6}$$

$$\tan\delta = \varepsilon''/\varepsilon' \tag{5.7}$$

where k is the extinction coefficient (imaginary part of the complex refractive indices ($n + ik$), $k = \alpha\lambda_0/(4\pi)$ with $\lambda_0 = c/\nu$ the wavelength *in vacuo* and c the speed of light.

Three commercial thermoplastics, *viz.* PC, PMMA, and ABS are studied in this present work, with relevant material properties given in Refs. [103, 179] (in which certain similar THz measurements were also made). Since the surfaces of all investigated samples are visibly smooth and flat, surface scattering is not expected to be significant for our study's near-normal incidence (though it is expected to be an issue for propagation in the plane of the plastic sheets).

From Eqs. (5.2) and (5.3), $n(\nu)$ and $\alpha(\nu)$ were obtained directly from the experimen-

tal measurements of the THz signals and are presented in Fig. 5.25. PMMA exhibits a somewhat lower $n(\nu)$ than the other plastics. In all cases, $n(\nu)$ exhibits a slightly negative dispersion $dn/d\nu$ with $n(\nu)$ for PMMA reducing from 1.63 at 0.5 THz to 1.59 at 2 THz, for PC reducing from 1.67 at 0.5 THz to 1.64 at 2 THz, and for ABS reducing from 1.68 at 0.5 THz to 1.64 at 2 THz. This trend is consistent with previous reports for similar materials in Refs. [82, 88] though as pointed out *supra*, values of the optical constants vary in the literature.

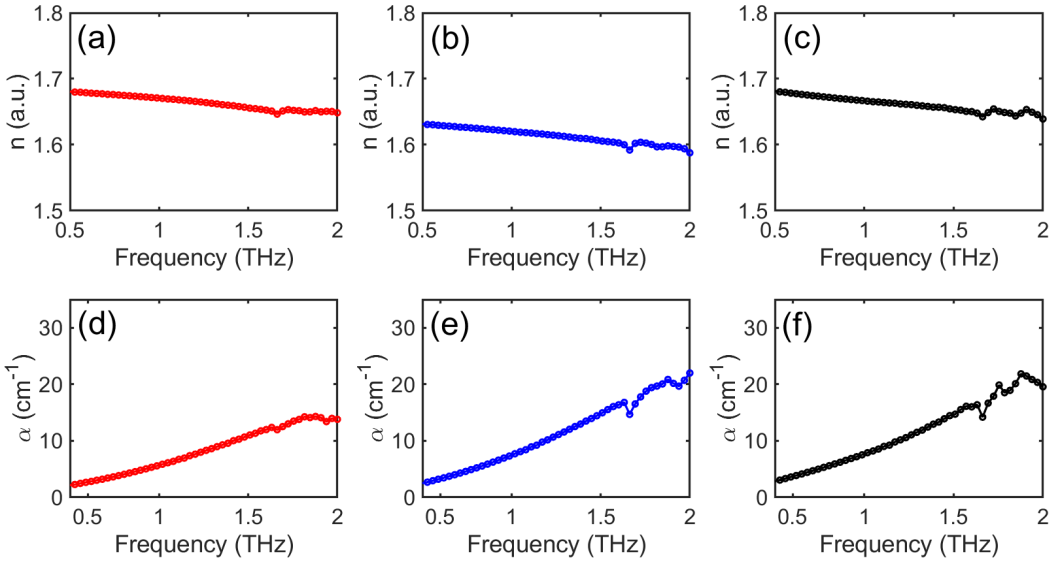

Figure 5.25: $n(\nu)$ for (a) PC, (b) PMMA, and (c) ABS, $\alpha(\nu)$ for (d) PC, (e) PMMA, and (f) ABS, from 0.5 THz to 2 THz.

Figure. 5.25 (d)-(f) show $\alpha(\nu)$, with $\alpha(0.5$ THz) for PMMA, PC, and ABS is 2.5 cm^{-1}, 2.1 cm^{-1}, and 2.9 cm^{-1}, respectively, with $\alpha(2$ THz) increasing to 22 cm^{-1}, 13.6 cm^{-1}, and 19.6 cm^{-1}. The feature at $\sim$1.66 THz is likely due to a water-vapor resonance [180]. The values of $\alpha(\nu)$, obtained in this work, are consistent with the literature [82, 88, 181]. For example, in Ref. [82], for PC $n(1$ THz$)= 1.665$ and $\alpha(1$ THz$)= 9.6$ cm^{-1}, while for PMMA $n(1$ THz$)= 1.61$ and $\alpha(1$ THz$)= 11.3$ cm^{-1}, though the losses we measure at 1 THz are somewhat lower. Note that earlier work [88, 92, 182] (also cited in Ref. [82]), while finding similar values for the refractive index for PC and PMMA, shows a large scatter in the loss measurements for PMMA.

Since the 1970s, it has been noted that, at low frequencies, $\alpha(\nu)$ for materials with the disorder varies with ν as a power-law [84, 183]. A refinement of the ideas presented followed the observation that the product $n(\nu)\alpha(\nu)$ for amorphous materials obeys a power-law relation [117, 181, 184]

$$n(\nu)\alpha(\nu) = K(h\nu)^{\beta} \tag{5.8}$$

where h is the planck's constant, and the absorption parameter K is material-dependent [184]. The exponent β is related to the characteristics of the disorder, and satisfies $\beta \leq 2$. For glasses, typically $\beta \approx 2$; however, for plastics in many cases, β is somewhat less than 2. The values of Kh^2 and β are obtained after fitting $n(\nu)\alpha(\nu)$, and are listed in Table 5.2. The values of β and Kh^2 obtained by fitting to our data are in close agreement with those quoted in Ref. [9]. We next convert $n(\nu)$ and $\alpha(\nu)$ to $\varepsilon'(\nu)$ and $\varepsilon''(\nu)$ using Eqs. (5.5)

Table 5.2: THz refractive indices $n(\nu)$, Kh^2, and β based on fit to data.

Material	n (a.u.) (average)	Dispersion $(n_{0.5\,THz} - n_{2\,THz})$	Kh^2 $(cm^{-1}s^2)$	β
PMMA	1.62	0.04	24.38	1.52
PC	1.66	0.03	23.05	1.37
ABS	1.67	0.04	27.37	1.48

and (5.6). Figure 5.26 (a-c) show $\varepsilon'(\nu)$. Compared to PC and ABS, PMMA possesses a lower $\varepsilon'(\nu)$ consistent with the lower value of $n(\nu)$ noted above. In addition, for the three plastics $\varepsilon'(\nu)$ decreases slightly with ν, again, largely reflecting the dispersion in $n(\nu)$. The results here for PMMA can be compared with those of Ref. [29]. Broadly speaking, $\varepsilon'(\nu)$ is in good agreement with their measurements, though we find somewhat higher values of $\tan\delta$ at higher frequencies. It should be noted that, for dielectric measurements, there may be a surface-scattering contribution in the measurements, both of Ref. [29], and those presented here (and in many other such published measurements). This contribution can be eliminated by comparing measurements on slabs of various thicknesses but with the same surface texture.

Loss tangent $\tan\delta(\nu)$ is determined using Eq. (5.7). As shown in Fig. 5.26, PC has

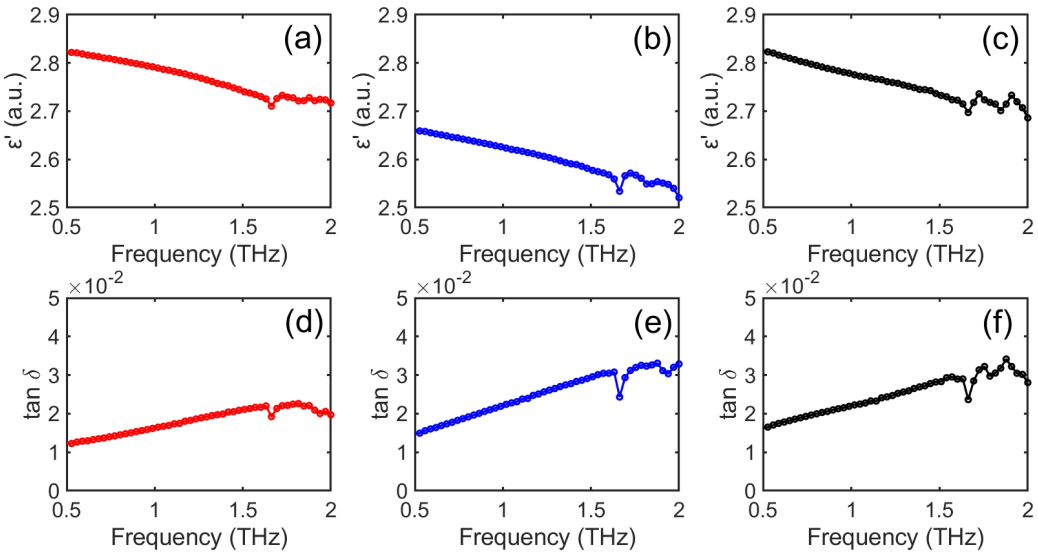

Figure 5.26: Measured permittivity $\varepsilon'(\nu)$ for (a) PC, (b) PMMA, and (c) ABS, loss tangent $\tan\delta(\nu)$ for (d) PC, (e) PMMA, and (f) ABS, from 0.5 THz to 2 THz.

the lowest tangent, consistent with its lower $\alpha(\nu)$, compared with the other plastics. Table 5.3 summarizes $\varepsilon'(\nu)$ and $\tan\delta(\nu)$ at 500 GHz, 1 THz, 1.5 THz, and 2 THz for the three plastics.

Table 5.3: Comparision of ε' and $\tan\delta$ between PMMA, PC and ABS.

Material	$\varepsilon'(\nu)$				$\tan\delta$			
	0.5 THz	1 THz	1.5 THz	2 THz	0.5 THz	1 THz	1.5 THz	2 THz
PMMA	2.66	2.63	2.58	2.52	0.015	0.022	0.029	0.033
PC	2.81	2.77	2.72	2.69	0.012	0.016	0.02	0.02
ABS	2.83	2.78	2.73	2.69	0.016	0.022	0.028	0.028

In this work, the dielectric properties of three common off-the-shelf thermoplastics were characterized using THz TDS. The refractive index $n(\nu)$, absorption coefficient $\alpha(\nu)$, permittivity $\varepsilon(\nu) = \varepsilon'(\nu) + i\varepsilon''(\nu)$, and loss tangent $\tan\delta(\nu)$ for PC, PMMA, and ABS, are presented from 500 GHz to 2 THz. We find that in the entire frequency range, $\tan\delta(\nu)$ varies from 0.012 to 0.033, while $\varepsilon'(\nu)$ is from 2.84 to 3.22. In summary, the refractive index and dielectric losses of the investigated thermoplastics are low compared with glasses. We expect some variations in the dielectric properties of each of these materials, depending on the vendor. While there is an overall agreement with past measurements, we must rec-

ognize that there is still considerable scatter in some of the data. It should also be pointed out that some of the measurements are up to two decades old, calling for re-evaluation. There is also not a great deal of data published on ABS.

In all cases, low dielectric loss, together with compatibility with some board-manufacturing processes, make these plastics promising candidates for 6G applications, as well as for packaging of modules, systems, and entire hand-held devices and as constituent materials for metasurfaces and other types of filters and reflectors. Photoconductive THz sources integrated with guiding structures and broadside antennae may enable higher optical-to-THz conversion by approaches that incorporate the antenna on a plastic substrate. These materials, while not having a long life, nor exhibiting favourable thermal properties in many cases, remain attractive for their low cost.

CHAPTER 6
CONCLUSION AND PERSPECTIVE

6.1 Conclusion

The promise of terahertz (THz) pulsed imaging (TPI) and time-domain spectroscopy (TDS) as a non-contact and non-ionizing modality for non-destructive evaluation (NDE) and material characterization in both academic and industrial fields are well demonstrated in this thesis.

In chapter 3, THz reflectometry provides a reliable contactless approach to nondestructively characterize scale film on steel with thicknesses down to $\sim 5\ \mu m$ and, by extension, other electrically non-conducting oxide films. In addition, the THz time-of-flight technique (TOFT) combined with autoregressive spectral extrapolation based on the modified covariance method (AR/MCM) algorithm succeeded at globally stratigraphically reconstructing multilayer coatings on steel in a non-destructive and non-contact fashion. The uniformity of individual layers calculated based on THz results agrees with eddy-current-based measurements, though deviations are observed when layer thicknesses are $\lesssim 10\ \mu m$. AR/MCM does not require extensive training or a specific physical model to carry our accurate reconstruction as a relatively robust analysis technique.

Some significant progress has been achieved in the stratigraphic characterization of materials with complex structures, as presented in chapter 4. A factor-of-two improvement in the maximum thickness of polycarbonate (PC) and poly-methyl methacrylate (PMMA) sheets that THz TOFT can resolve is achieved after accounting for dispersion. Sparse deconvolution (SD), based on an interior-point method in conjunction with a propagation model accounting for dispersion, is proved successful in reconstructing the stratigraphy of a complex sample incorporating both optically thick and thin layers. While the maximum

determinable thickness by SD is less than cross-correlation (CC), SD may still be the preferred option for stratigraphic reconstruction of moderately thick samples with complex structures, even in the absence of structural information investigated materials. The practical prospects of THz-based techniques in automated paper handling of legacy documents are also discussed. The page count of a paper stack is obtained through reconstructing the stratigraphy of the stack based on the reflected THz signal, and a staple binding the four central sheets in an s = 10-sheet paper stack is also detected. Owing to the strong THz reflection from the aluminum staple, the location of the staple is identified successfully in the three-dimensional rending.

Finally, chapter 5 of this thesis presents a detailed discussion on material characterization using THz TDS. THz birefringence and surface homogeneity of nanoporous Al_2O_3 films on Al are investigated using Polarization-resolved THz TDS and THz scattering imaging. As a non-contact, non-ionizing, and non-destructive approach, THz-based technology can serve as a complementary technique of atomic force microscopy (AFM), scanning electron microscopy (SEM), and x-ray diffraction (XRD) that only covers a relatively small scan size. Moreover, THz-based technology has proved to be an effective tool for quality control of injection-molded thermoplastic components, such as locating the weld line defects. This information can be used to improve manufacturing and the NDE of components on the production line and in service. Lastly, the dielectric properties and loss tangent of three frequently used, low-cost, and off-the-shelf thermoplastics were also characterized using THz TDS from 500 GHz to 2 THz. Compared with glasses, all investigated plastics' refractive index and dielectric losses are low within the entire frequency range, making them attractive candidates for selected applications for future sixth-generation (6G) systems, such as microelectronic packaging and waveguides.

6.2 Perspective

The potential practical applications of THz imaging in the industry and academia are worthy of further exploration.

In our previous work in [185], mill scale films (form on the surface of steel during the steel process and consist of mixed different iron oxides) with thickness down to 5 μm were characterized successfully in a non-destructive and non-contact fashion using THz TOFT in conjunction with advanced posted signal processing techniques. In that work, however, all investigated steel coupons were fabricated under laboratory conditions, demonstrating that all manufacturing parameters, including finishing temperature, the content of oxygen in the atmosphere, and the cooling rate, were precisely controlled. The success of characterizing laboratory-produced mill-scale films leads to the question: Is THz TOFT likewise successful in characterizing d for tertiary mill scale on *production* steel plates rather than on samples produced under controlled laboratory conditions? Therefore, more efforts should also be made to directly introduce the pulsed THz reflectometry to the shopfloor for in-line monitoring of the quality of fabricated steel products. Several serious issues, such as the influence of high temperature on the performance of commercial THz devices, the influence of the motion of investigated steel products, defocus, and non-specular scattering related to the rough surface, should be considered to avoid unexpected errors. Moreover, because of THz waves' high sensitivity to water vapors, how to overcome the influence of humidity on the waveform of THz reflected signals is also worth studying before implementation. Except for the in-line quality control of steel products, the corrosion mechanisms at earlier stages than visual inspection under paint also deserve exploration. There is no consensus within the steel industry on how blisters (one type of specific defect) are introduced during the corrosion process, even away from the scratch lines. THz-based technology might be a promising tool to study this issue due to the penetration of THz radiations.

Although recent works have demonstrated the promising potential of THz-based tech-

nology on material characterization, further developments are still necessary. For the short fiber-reinforced thermoplastics, the residual lifetime of polymer composite materials under mechanical loading conditions can be estimated approximately based on the defect types diagnosed by TPI. In general, matrix cracking and debonding at fiber tips occur at the early stage of the composite life, and fiber/matrix debonding and coalescence of damaged cavities are introduced between the 15% and 85% of the composite life. Fiber breakage happens before the material's failure. Having a physical understanding of the evolution of damages in composite during the fatigue loading and related damage mechanisms is crucial to quality control of the material itself. Furthermore, the dielectric and optical properties (*e.g.*, absorption coefficients $\alpha(\nu)$, refractive index $n(\nu)$, complex permittivity $\varepsilon(\nu)$, and loss tangent $\tan\,\delta$) of materials with potential applications in emerging 6G communication systems, ranging from microelectronics packaging to meta-surfaces for reflectors and filters, are also worth of study systematically within THz frequency regime. This valuable information can directly assess materials prior to the fabrication and packaging of millimeter-wave (mmW) antennas and integrated systems.

Investing THz-based technology in other research fields, such as cultural heritage conservation science, is also worth exploring. Compared to x-rays and infrared, THz radiations can penetrate deep and allow for safe (non-ionizing) in deep three-dimensional (3D) imaging of individual layers. Therefore, THz-based technology shows a good application prospect in this research field. To date, various types of archaeological and historical artworks, including panel paintings, wall paintings, papyruses, fabric, and mummies, have proved the advantages of THz-based technology in the detection of hidden layers and material characterization (*e.g.*, pigments) and authenticity identification. Extensive efforts should be made to correlate THz images and results from other classic NDE techniques to understand the investigated artworks better. Spectroscopic study of ancient pigments should be carried on to provide valuable color information for the restoration of cultural relics.

6.3 Publications

Peer-reviewed publications

[1]. **M. Zhai**, A. Locquet, D.S. Citrin, Terahertz dielectric characterization of low-loss thermoplastics for 6G applications, *Int. J. Wirel. Inf. Netw.*, 2022.

[2]. **M. Zhai**, A. Locquet, M. Jung, D. Woo, D.S. Citrin, Nondestructive characterization of nanoporous alumina films using terahertz scattering imaging, *Surf. Coat. Tech.*, 126792, 2021.

[3]. **M. Zhai**, E.A. Mohamed, A. Locquet, G. Schneider, R. Kalmar, M. Fendler, N.F. Declercq, D.S. Citrin, Diagnosis of injection-molded weld lines in ABS thermoplastic by polarized terahertz reflective imaging, *NDT&E Int.*, 102497, 2021.

[4]. **M. Zhai**, A. Locquet, D.S. Citrin, Terahertz imaging for paper handling of legacy documents, *Sensors*, 21(20), 6756, 2021.

[5]. **M. Zhai**, D.S. Citrin, A. Locquet, Terahertz nondestructive stratigraphic analysis of complex layered structures: reconstruction techniques, *J Infrared Millim Terahertz Waves*, 2(9):929-46, 2021.

[6]. **M. Zhai**, A. Locquet, C. Roquelet, P. Alexandre, L. Daheron, D.S. Citrin, Nondestructive measurement of mill-scale thickness on steel by terahertz time-of-flight tomography, *Surf. Coat. Tech.*, 125765, 2020.

[7]. **M. Zhai**, A. Locquet, D.S. Citrin, THz imaging for thickness characterization of plastic sheets, *NDT&E Int.*, 102338, 2020.

[8]. **M. Zhai**, A Locquet, M. Jung, D. Woo, D.S. Citrin, Characterization of nanoporous Al_2O_3 films at terahertz frequencies, *Opt. Lett.*, 45(14): 4092-5, 2020.

[9]. **M. Zhai**, A. Locquet, C. Roquelet, D.S. Citrin, Terahertz time-of-flight tomography beyond the axial- resolution limit: Autoregressive spectral estimation based on the modified covariance method, *J Infrared Millim Terahertz Waves*, 41(8): 926-39, 2020.

[10]. E.A. Mohamed, **M. Zhai**, A. Locquet, D.S. Citrin, N. F. Declercq, G. Schneider, R.

Kalmar, M. Fendler, Scanning acoustic microscopy investigation of the mechanical properties of injection-molded plastic weld lines in industrial plastic polymer, *Micron*, 102925, 2020.

[11]. **M. Zhai**, A. Locquet, C. Roqelet, L.A. Ronqueti, D.S. Citrin, Nondestructive thickness characterization of multi-layer coatings on steel by terahertz time-of-flight tomography, *NDT&E Int.*, 102358, 2020.

Conference Presentations

[1]. **M. Zhai**, E.T. Mohamed, A. Locquet, G. Schneider, R. Kalmar, M. Fendler, N.F. Declercq, D.S. Citrin. Diagnosis of injection-molded weld line in thermoplastic polymer by terahertz reflective imaging and scanning acoustic microscopy, *46th international conference on infrared, millimeter and terahertz waves*, Chengdu, China, 2021.

[2]. **M. Zhai**, A. Locquet, M. Jung, D. Woo, D.S. Citrin, Characterization of nanoporous alumina using terahertz reflectometry and scattering imaging, *46th international conference on infrared, millimeter, and terahertz waves*, Chengdu, China, 2021.

[3]. **M. Zhai**, E.T. Mohamed, A. Locquet, G. Schneider, R. Kalmar, M. Fendler, N.F. Declercq, D.S. Citrin, Diagnosis of injection-molded weld line in thermoplastic polymer by terahertz reflective imaging and scanning acoustic microscopy, *46th international conference on infrared, millimeter, and terahertz waves*, Chengdu, China, 2021.

[4]. **M. Zhai**, A. Locquet, D.S. Citrin, THz imaging of injection-mold weld lines in ABS thermoplastic, *Journées du GDR NanoTeraMIR*, Metz, France, 2021.

[5]. **M. Zhai**, A. Locquet, D.S. Citrin, Terahertz nondestructive thickness characterization of optically thin metal oxide layers on steel, *9th international workshop on terahertz technology and application*, Kaiserslautern, Germany, 2020.

[6]. **M. Zhai**, A. Locquet, D.S. Citrin, Pulsed THz tomography of plastic sheets: thickness characterization and dispersion, *9th international workshop on terahertz technology and application*, Kaiserslautern, Germany, 2020.

[7]. **M. Zhai**, A. Locquet, D.S. Citrin, The individual thickness characterization of stacked sample by terahertz imaging, *11th THz young scientists meeting*, Marburg, Germany, 2020.

[8]. **M. Zhai**, A. Locquet, C. Roquelet, D.S. Citrin, Terahertz thickness measurement of multiple-layered coatings, *45th international conference on infrared, millimeter, and terahertz waves*, Buffalo, New York, USA, 2020.

[9]. **M. Zhai**, A. Locquet, D.S. Citrin, Characterization of nanoporous alumina using terahertz time domain reflectometry, *45th international conference on infrared, millimeter, and terahertz waves*, Buffalo, New York, USA, 2020.

[10]. **M. Zhai**, A. Locquet, C.C. Monfort, K.A. Kazek, D.S. Citrin, Terahertz characterization of roman amphora sherds, *45th international conference on infrared, millimeter, and terahertz waves*, Buffalo, New York, USA, 2020.

[11]. **M. Zhai**, A. Locquet, C. Roquelet, D.S. Citrin, Structural characterization of mill-scale on production steel using terahertz pulse imaging in reflective geometry, *45th international conference on infrared, millimeter, and terahertz waves*, Buffalo, New York, USA, 2020.

[12]. **M. Zhai**, A. Locquet, D.S. Citrin, THz thickness characterization of plastic sheets including dispersion. *44th international conference on infrared, millimeter, and terahertz waves*, Paris, France, 2019.

[13]. **M. Zhai**, A. Locquet, C. Roquelet, D.S. Citrin, Terahertz non-destructive thickness characterization of optically thin scale layers on steel. *44th international conference on infrared, millimeter, and terahertz waves*, Paris, France, 2019.

[14]. **M. Zhai**, A. Locquet, C. Roquelet, D.S. Citrin, Terahertz nondestructive characterization of optically thin wüstite layers on steel. *Journées du GDR NanoTeraMIR*, Saint Raphaël, France, 2019.

[15]. **M. Zhai**, A. Locquet, D.S. Citrin, Terahertz time-domain spectroscopy for paper handling of legacy documents, *10th international workshop on Terahertz technology and application*, Kaiserslautern, Germany, 2022.

[16]. **M. Zhai**, A. Locquet, D.S. Citrin, Material characterization of low-loss thermoplastics using terahertz time-domain spectroscopy, *French-German terahertz conference*, La Grande Motte, France, 2022.

[17]. **M. Zhai**, A. Locquet, D.S. Citrin, Terahertz characterization of low-loss thermoplastics and EN-A1 Alkali-free Boroaluminasilicate glass for 6G applications, *47th international conference on infrared, millimeter, and terahertz waves*, Delft, Netherlands, 2022.

REFERENCES

[1] Y.-S. Lee, *Principles of terahertz science and technology*. Springer Science & Business Media, 2009, vol. 170.

[2] C. Kulesa, "Terahertz spectroscopy for astronomy: From comets to cosmology," *IEEE Transactions on Terahertz Science and Technology*, vol. 1, no. 1, pp. 232–240, 2011.

[3] K. Ahi, S. Shahbazmohamadi, and N. Asadizanjani, "Quality control and authentication of packaged integrated circuits using enhanced-spatial-resolution terahertz time-domain spectroscopy and imaging," *Optics and Lasers in Engineering*, vol. 104, pp. 274–284, 2018.

[4] J. B. Jackson, J. Bowen, G. Walker, J. Labaune, G. Mourou, M. Menu, and K. Fukunaga, "A survey of terahertz applications in cultural heritage conservation science," *IEEE Transactions on Terahertz Science and Technology*, vol. 1, no. 1, pp. 220–231, 2011.

[5] H.-B. Liu, H. Zhong, N. Karpowicz, Y. Chen, and X.-C. Zhang, "Terahertz spectroscopy and imaging for defense and security applications," *Proceedings of the IEEE*, vol. 95, no. 8, pp. 1514–1527, 2007.

[6] Y.-C. Shen, "Terahertz pulsed spectroscopy and imaging for pharmaceutical applications: A review," *International Journal of Pharmaceutics*, vol. 417, no. 1-2, pp. 48–60, 2011.

[7] R. F. Anastasi and E. I. Madaras, "Terahertz NDE for under paint corrosion detection and evaluation," in *AIP Conference Proceedings*, American Institute of Physics, vol. 820, 2006, pp. 515–522.

[8] Z. Chen, X. Ma, B. Zhang, Y. Zhang, Z. Niu, N. Kuang, W. Chen, L. Li, and S. Li, "A survey on terahertz communications," *China Communications*, vol. 16, no. 2, pp. 1–35, 2019.

[9] M. Naftaly and R. E. Miles, "Terahertz time-domain spectroscopy for material characterization," *Proceedings of the IEEE*, vol. 95, no. 8, pp. 1658–1665, 2007.

[10] J. Král, R. Smid, H. G. Ramos, and A. L. Ribeiro, "Thickness measurement using transient eddy current techniques," in *2011 IEEE International Instrumentation and Measurement Technology Conference*, IEEE, 2011, pp. 1–6.

[11] S. E. Fritz, S. M. Martin, C. D. Frisbie, M. D. Ward, and M. F. Toney, "Structural characterization of a pentacene monolayer on an amorphous SiO_2 substrate with grazing incidence x-ray diffraction," *Journal of the American Chemical Society*, vol. 126, no. 13, pp. 4084–4085, 2004.

[12] M. R. Jolly, A. Prabhakar, B. Sturzu, K. Hollstein, R. Singh, S. Thomas, P. Foote, and A. Shaw, "Review of non-destructive testing (NDT) techniques and their applicability to thick walled composites," *Procedia CIRP*, vol. 38, pp. 129–136, 2015.

[13] T. Sakagami, "Remote nondestructive evaluation technique using infrared thermography for fatigue cracks in steel bridges," *Fatigue & Fracture of Engineering Materials & Structures*, vol. 38, no. 7, pp. 755–779, 2015.

[14] A. J. Bahr, "Experimental techniques in microwave NDE," in *Review of Progress in Quantitative Nondestructive Evaluation*, Springer, 1995, pp. 593–600.

[15] Y. Chen, H. Liu, Y. Deng, D. B. Veksler, M. S. Shur, X.-C. Zhang, D. Schauki, M. J. Fitch, R. Osiander, C. Dodson, and J. B. Spicer, "Spectroscopic characterization of explosives in the far-infrared region," in *Terahertz for Military and Security Applications II*, International Society for Optics and Photonics, vol. 5411, 2004, pp. 1–8.

[16] A. Dutta, "Fourier transform infrared spectroscopy," *Spectroscopic methods for nanomaterials characterization*, pp. 73–93, 2017.

[17] V. Lucarini, J. J. Saarinen, K.-E. Peiponen, and E. M. Vartiainen, *Kramers-Kronig relations in optical materials research*. Springer Science & Business Media, 2005, vol. 110.

[18] M. C. Beard, G. M. Turner, and C. A. Schmuttenmaer, "Subpicosecond carrier dynamics in low-temperature grown GaAs as measured by time-resolved terahertz spectroscopy," *Journal of Applied Physics*, vol. 90, no. 12, pp. 5915–5923, 2001.

[19] J. F. De Boer, T. E. Milner, M. J. Van Gemert, and J. S. Nelson, "Two-dimensional birefringence imaging in biological tissue by polarization-sensitive optical coherence tomography," *Optics Letters*, vol. 22, no. 12, pp. 934–936, 1997.

[20] D. Stifter, P. Burgholzer, O. Höglinger, E. Götzinger, and C. K. Hitzenberger, "Polarisation-sensitive optical coherence tomography for material characterisation and strain-field mapping," *Applied Physics A*, vol. 76, no. 6, pp. 947–951, 2003.

[21] B. A. Palmer, G. R. Edwards-Gau, B. M. Kariuki, K. D. Harris, I. P. Dolbnya, and S. P. Collins, "X-ray birefringence imaging," *Science*, vol. 344, no. 6187, pp. 1013–1016, 2014.

[22] A. G. Davies, A. D. Burnett, W. Fan, E. H. Linfield, and J. E. Cunningham, "Terahertz spectroscopy of explosives and drugs," *Materials Today*, vol. 11, no. 3, pp. 18–26, 2008.

[23] T. Yasui, T. Yasuda, K.-i. Sawanaka, and T. Araki, "Terahertz paintmeter for noncontact monitoring of thickness and drying progress in paint film," *Applied Optics*, vol. 44, no. 32, pp. 6849–6856, 2005.

[24] T. Yasuda, T. Iwata, T. Araki, and T. Yasui, "Improvement of minimum paint film thickness for THz paint meters by multiple-regression analysis," *Applied Optics*, vol. 46, no. 30, pp. 7518–7526, 2007.

[25] K. Su, Y.-C. Shen, and J. A. Zeitler, "Terahertz sensor for non-contact thickness and quality measurement of automobile paints of varying complexity," *IEEE Transactions on Terahertz Science and Technology*, vol. 4, no. 4, pp. 432–439, 2014.

[26] J. Dong, A. Locquet, and D. Citrin, "Terahertz quantitative nondestructive evaluation of failure modes in polymer-coated steel," *IEEE Journal of Selected Topics in Quantum Electronics*, vol. 23, no. 4, pp. 1–7, 2016.

[27] S. Krimi, J. Klier, J. Jonuscheit, G. von Freymann, R. Urbansky, and R. Beigang, "Highly accurate thickness measurement of multi-layered automotive paints using terahertz technology," *Applied Physics Letters*, vol. 109, no. 2, p. 021 105, 2016.

[28] J. Dong, X. Wu, A. Locquet, and D. S. Citrin, "Terahertz superresolution stratigraphic characterization of multilayered structures using sparse deconvolution," *IEEE Transactions on Terahertz Science and Technology*, vol. 7, no. 3, pp. 260–267, 2017.

[29] T. Chang, Q. Guo, L. Liu, and H.-L. Cui, "Hilbert-transform-based accurate determination of ultrashort-time delays in terahertz time-domain spectroscopy," *IEEE Transactions on Terahertz Science and Technology*, vol. 7, no. 5, pp. 514–520, 2017.

[30] J. Dong, A. Locquet, and D. Citrin, "Depth resolution enhancement of terahertz deconvolution by autoregressive spectral extrapolation," *Optics letters*, vol. 42, no. 9, pp. 1828–1831, 2017.

[31] D. G. A. Ibrahim, S. K. Khalil, H. Sherif, and M. Eloker, "Multilayer film thickness measurement using ultrafast terahertz pulsed imaging," *Journal of Physics Communications*, vol. 3, no. 3, p. 035 013, 2019.

[32] Z. Xu, D. Ye, J. Chen, and H. Zhou, "Novel terahertz nondestructive method for measuring the thickness of thin oxide scale using different hybrid machine learning models," *Coatings*, vol. 10, no. 9, p. 805, 2020.

[33] T. Tanabe and Y. Oyama, "Terahertz non-destructive monitoring for infrastructure components," in *2018 Asia-Pacific Microwave Conference (APMC)*, IEEE, 2018, pp. 1471–1473.

[34] A. Jagannathan, A. J. Gatesman, and R. H. Giles, "Characterization of roughness parameters of metallic surfaces using terahertz reflection spectra," *Optics letters*, vol. 34, no. 13, pp. 1927–1929, 2009.

[35] T. Yasui, T. Yasuda, K.-i. Sawanaka, and T. Araki, "Terahertz paintmeter for non-contact monitoring of thickness and drying progress in paint film," *Applied Optics*, vol. 44, no. 32, pp. 6849–6856, 2005.

[36] J. Van Mechelen, "Predicting the dry thickness of a wet paint layer," in *2018 43rd International Conference on Infrared, Millimeter, and Terahertz Waves (IRMMW-THz)*, IEEE, 2018, pp. 1–2.

[37] J. Chen, Y. Chen, H. Zhao, G. J. Bastiaans, and X.-C. Zhang, "Absorption coefficients of selected explosives and related compounds in the range of 0.1–2.8 THz," *Optics Express*, vol. 15, no. 19, pp. 12 060–12 067, 2007.

[38] M. Naftaly, J. Molloy, G. Lanskii, K. Kokh, and Y. M. Andreev, "Terahertz time-domain spectroscopy for textile identification," *Applied Optics*, vol. 52, no. 19, pp. 4433–4437, 2013.

[39] F. Wahaia, I. Kasalynas, D. Seliuta, G. Molis, A. Urbanowicz, C. D. C. Silva, F. Carneiro, G. Valusis, and P. L. Granja, "Terahertz spectroscopy for the study of paraffin-embedded gastric cancer samples," *Journal of Molecular Structure*, vol. 1079, pp. 391–395, 2015.

[40] S. Yoon, S. Cha, S. Jun, S. Park, J.-Y. Park, S Lee, H. Kim, and Y. Ahn, "Identifying different types of microorganisms with terahertz spectroscopy," *Biomedical Optics Express*, vol. 11, no. 1, pp. 406–416, 2020.

[41] R. Pan, S. Zhao, and J. Shen, "Terahertz spectra applications in identification of illicit drugs using support vector machines," *Procedia Engineering*, vol. 7, pp. 15–21, 2010.

[42] X. Wang, K.-x. Hu, L. Zhang, X. Yu, and E.-j. Ding, "Characterization and classification of coals and rocks using terahertz time-domain spectroscopy," *Journal of Infrared, Millimeter, and Terahertz Waves*, vol. 38, no. 2, pp. 248–260, 2017.

[43] K. Li, X. Chen, R. Zhang, and E. Pickwell-MacPherson, "Classification for glucose and lactose terahertz spectrums based on SVM and DNN methods," *IEEE Transactions on Terahertz Science and Technology*, vol. 10, no. 6, pp. 617–623, 2020.

[44] R Piesiewicz, T Kleine-Ostmann, N Krumbholz, D Mittleman, M Koch, and T Kürner, "Terahertz characterisation of building materials," *Electronics Letters*, vol. 41, no. 18, pp. 1002–1004, 2005.

[45] S. Sahin, N. K. Nahar, and K. Sertel, "Dielectric properties of low-loss polymers for mmw and THz applications," *Journal of Infrared, Millimeter, and Terahertz Waves*, vol. 40, no. 5, pp. 557–573, 2019.

[46] M. Reid and R. Fedosejevs, "Terahertz birefringence and attenuation properties of wood and paper," *Applied Optics*, vol. 45, no. 12, pp. 2766–2772, 2006.

[47] Y. Kim, M. Yi, B. G. Kim, and J. Ahn, "Investigation of thz birefringence measurement and calculation in Al_2O_3 and $LiNbO_3$," *Applied Optics*, vol. 50, no. 18, pp. 2906–2910, 2011.

[48] M. Kashima, S. Tsuchikawa, and T. Inagaki, "Simultaneous detection of density, moisture content and fiber direction of wood by THz time-domain spectroscopy," *Journal of Wood Science*, vol. 66, no. 1, pp. 1–8, 2020.

[49] G.-H. Oh, J.-H. Jeong, S.-H. Park, and H.-S. Kim, "Terahertz time-domain spectroscopy of weld line defects formed during an injection moulding process," *Composites Science and Technology*, vol. 157, pp. 67–77, 2018.

[50] J. Neu and C. Schmuttenmaer, "Tutorial: An introduction to terahertz time domain spectroscopy (THz-TDS)," *Journal of Applied Physics*, vol. 124, no. 23, p. 231 101, 2018.

[51] Y. Chen, S. Huang, and E. Pickwell-MacPherson, "Frequency-wavelet domain deconvolution for terahertz reflection imaging and spectroscopy," *Optics Express*, vol. 18, no. 2, pp. 1177–1190, 2010.

[52] B. Ferguson and D. Abbott, "De-noising techniques for terahertz responses of biological samples," *Microelectronics Journal*, vol. 32, no. 12, pp. 943–953, 2001.

[53] N. Sunaguchi, Y. Sasaki, N. Maikusa, M. Kawai, T. Yuasa, and C. Otani, "Depth-resolving THz imaging with tomosynthesis," *Optics Express*, vol. 17, no. 12, pp. 9558–9570, 2009.

[54] D. M. Mittleman, R. H. Jacobsen, and M. C. Nuss, "T-ray imaging," *IEEE Journal of Selected Topics in Quantum Electronics*, vol. 2, no. 3, pp. 679–692, 1996.

[55] J. Pei, P. Ye, and W. Xie, "Optimal wavelet analysis for THz-TDS pulse signals," in *Photonics and Optoelectronics Meetings (POEM) 2008: Terahertz Science and Technology*, International Society for Optics and Photonics, vol. 7277, 2009, p. 727 708.

[56] M. Srivastava, C. L. Anderson, and J. H. Freed, "A new wavelet denoising method for selecting decomposition levels and noise thresholds," *IEEE Access*, vol. 4, pp. 3862–3877, 2016.

[57] B. Qiao, X. Zhang, J. Gao, R. Liu, and X. Chen, "Sparse deconvolution for the large-scale ill-posed inverse problem of impact force reconstruction," *Mechanical Systems and Signal Processing*, vol. 83, pp. 93–115, 2017.

[58] J. Dong, A. Locquet, M. Melis, and D. Citrin, "Global mapping of stratigraphy of an old-master painting using sparsity-based terahertz reflectometry," *Scientific Reports*, vol. 7, no. 1, pp. 1–12, 2017.

[59] H. Akaike, "A new look at the statistical identification model," *IEEE Transactions on Automatic Control*, vol. 19, p. 716, 1974.

[60] H. Akaike, "Information theory and an extension of the maximum likelihood principle," in *Selected papers of hirotugu akaike*, Springer, 1998, pp. 199–213.

[61] J. Rissanen, "Modeling by shortest data description," *Automatica*, vol. 14, no. 5, pp. 465–471, 1978.

[62] S. M. Alessio, *Digital signal processing and spectral analysis for scientists: concepts and applications*. Springer, 2015.

[63] F. Schrettle, C. Kant, P. Lunkenheimer, F. Mayr, J. Deisenhofer, and A. Loidl, "Wüstite: Electric, thermodynamic and optical properties of FeO," *The European Physical Journal B*, vol. 85, no. 5, p. 164, 2012.

[64] M. Takeda, T. Onishi, S. Nakakubo, and S. Fujimoto, "Physical properties of iron-oxide scales on Si-containing steels at high temperature," *Materials Transactions*, vol. 50, no. 9, pp. 2242–2246, 2009.

[65] T. Henning, B. Begemann, H. Mutschke, and J. Dorschner, "Optical properties of oxide dust grains.," *Astronomy and Astrophysics Supplement Series*, vol. 112, p. 143, 1995.

[66] T. Henning and H. Mutschke, "Low-temperature infrared properties of cosmic dust analogues.," *Astronomy and Astrophysics*, vol. 327, pp. 743–754, 1997.

[67] N. Hasegawa, T. Nagashima, and K. Hirano, "Thickness measurement of iron-oxide layers on steel plates using terahertz reflectometry," in *2011 International Conference on Infrared, Millimeter, and Terahertz Waves*, IEEE, 2011, pp. 1–2.

[68] S. Zhou, D. G. Valchev, A. Dinovitser, J. M. Chappell, A. Iqbal, B. W.-H. Ng, T. W. Kee, and D. Abbott, "Terahertz signal classification based on geometric algebra,"

IEEE Transactions on Terahertz Science and Technology, vol. 6, no. 6, pp. 793–802, 2016.

[69] B. Shakibi, F. Honarvar, M. Moles, J. Caldwell, and A. N. Sinclair, "Resolution enhancement of ultrasonic defect signals for crack sizing," *NDT & E International*, vol. 52, pp. 37–50, 2012.

[70] I. J. Gupta, M. J. Beals, and A. Moghaddar, "Data extrapolation for high resolution radar imaging," *IEEE Transactions on Antennas and Propagation*, vol. 42, no. 11, pp. 1540–1545, 1994.

[71] M. Kazubek, "Wavelet domain image denoising by thresholding and wiener filtering," *IEEE Signal Processing Letters*, vol. 10, no. 11, pp. 324–326, 2003.

[72] D. M. Mittleman, R. H. Jacobsen, R. Neelamani, R. G. Baraniuk, and M. C. Nuss, "Gas sensing using terahertz time-domain spectroscopy," *Applied Physics B*, vol. 67, no. 3, pp. 379–390, 1998.

[73] W. Fan, A. Burnett, P. Upadhya, J. Cunningham, E. Linfield, and A. Davies, "Far-infrared spectroscopic characterization of explosives for security applications using broadband terahertz time-domain spectroscopy," *Applied spectroscopy*, vol. 61, no. 6, pp. 638–643, 2007.

[74] P. U. Jepsen and B. M. Fischer, "Dynamic range in terahertz time-domain transmission and reflection spectroscopy," *Optics Letters*, vol. 30, no. 1, pp. 29–31, 2005.

[75] R. Bell, *Introductory Fourier transform spectroscopy*. Elsevier, 2012.

[76] A. Filler, "Apodization and interpolation in fourier-transform spectroscopy," *JOSA*, vol. 54, no. 6, pp. 762–767, 1964.

[77] R. H. Norton and R. Beer, "New apodizing functions for fourier spectrometry," *JOSA*, vol. 66, no. 3, pp. 259–264, 1976.

[78] R. H. Norton and R. Beer, "Errata: New apodizing functions for fourier spectrometry," *JOSA*, vol. 67, no. 3, pp. 419–419, 1977.

[79] F. J. Harris, "On the use of windows for harmonic analysis with the discrete fourier transform," *Proceedings of the IEEE*, vol. 66, no. 1, pp. 51–83, 1978.

[80] R. B. Blackman and J. W. Tukey, "The measurement of power spectra from the point of view of communications engineering—part I," *Bell System Technical Journal*, vol. 37, no. 1, pp. 185–282, 1958.

[81] J. Dong, A. Locquet, and D. Citrin, "Enhanced terahertz imaging of small forced delamination in woven glass fibre-reinforced composites with wavelet de-noising," *Journal of Infrared, Millimeter, and Terahertz Waves*, vol. 37, no. 3, pp. 289–301, 2016.

[82] E. Fedulova, M. M. Nazarov, A. Angeluts, M. Kitai, V. Sokolov, and A. Shkurinov, "Studying of dielectric properties of polymers in the terahertz frequency range," in *Saratov Fall Meeting 2011: Optical Technologies in Biophysics and Medicine XIII*, International Society for Optics and Photonics, vol. 8337, 2012, p. 83370I.

[83] V. Ryzhov, "Low-energy libration excitations in glassy PMMA," *Solid State Physics*, vol. 44, no. 12, pp. 2229–2233, 2002.

[84] A. K. Jonscher, "The 'universal' dielectric response," *Nature*, vol. 267, no. 5613, pp. 673–679, 1977.

[85] D. Das-Gupta and P. Scarpa, "Modeling of dielectric relaxation spectra of polymers in the condensed phase," *IEEE Electrical Insulation Magazine*, vol. 15, no. 2, pp. 23–32, 1999.

[86] P. Lunkenheimer and A. Loidl, "Response of disordered matter to electromagnetic fields," *Physical Review Letters*, vol. 91, no. 20, p. 207 601, 2003.

[87] R. Piesiewicz, C. Jansen, S Wietzke, D. Mittleman, M. Koch, and T. Kürner, "Properties of building and plastic materials in the THz range," *International Journal of Infrared and Millimeter Waves*, vol. 28, no. 5, pp. 363–371, 2007.

[88] Y.-S. Jin, G.-J. Kim, and S.-G. Jeon, "Terahertz dielectric properties of polymers," *Journal of the Korean Physical Society*, vol. 49, no. 2, pp. 513–517, 2006.

[89] W. He and Z. Guo Zhong, "Terahertz spectroscopic inspection of several kinds of plastic," *Acta Photonica Sinica*, vol. 39, no. 7, p. 1185, 2010.

[90] P. D. Cunningham, N. N. Valdes, F. A. Vallejo, L. M. Hayden, B. Polishak, X.-H. Zhou, J. Luo, A. K.-Y. Jen, J. C. Williams, and R. J. Twieg, "Broadband terahertz characterization of the refractive index and absorption of some important polymeric and organic electro-optic materials," *Journal of Applied Physics*, vol. 109, no. 4, pp. 043 505–043 505, 2011.

[91] E. Fedulova, M. M. Nazarov, A. Angeluts, M. Kitai, V. Sokolov, and A. Shkurinov, "Studying of dielectric properties of polymers in the terahertz frequency range," in *Saratov Fall Meeting 2011: Optical Technologies in Biophysics and Medicine XIII*, International Society for Optics and Photonics, vol. 8337, 2012, p. 83370I.

[92] V. Ryzhov, "Low-energy libration excitations in glassy PMMA," *Solid State Physics*, vol. 44, no. 12, pp. 2229–2233, 2002.

[93] Y.-S. Jin, G.-J. Kim, and S.-G. Jeon, "Terahertz dielectric properties of polymers," *Journal of the Korean Physical Society*, vol. 49, no. 2, pp. 513–517, 2006.

[94] S. Busch, M Weidenbach, M Fey, F Schäfer, T Probst, and M Koch, "Optical properties of 3D printable plastics in the THz regime and their application for 3D printed THz optics," *Journal of Infrared, Millimeter, and Terahertz Waves*, vol. 35, no. 12, pp. 993–997, 2014.

[95] H. Wang and G.-z. Zhao, "Terahertz spectroscopic inspection of several kinds of plastic," *Acta Photonica Sinica*, vol. 7, 2010.

[96] W. R. Folks, S. K. Pandey, and G. Boreman, "Refractive index at THz frequencies of various plastics," in *Optical Terahertz Science and Technology*, Optical Society of America, 2007, p. MD10.

[97] S. Zhou, D. G. Valchev, A. Dinovitser, J. M. Chappell, A. Iqbal, B. W.-H. Ng, T. W. Kee, and D. Abbott, "Terahertz signal classification based on geometric algebra," *IEEE Transactions on Terahertz Science and Technology*, vol. 6, no. 6, pp. 793–802, 2016.

[98] S. Wang and G. Chen, "Cauchy problem of the generalized double dispersion equation," *Nonlinear Analysis: Theory, Methods & Applications*, vol. 64, no. 1, pp. 159–173, 2006.

[99] G. P. John, G. M. Dimitris, and G Manolakis, "Digital signal processing: Principles, algorithms, and applications," *Pentice Hall*, 1996.

[100] S. Adrián-Martínez, M. Bou-Cabo, I. Felis, C. D. Llorens, J. A. Martínez-Mora, M. Saldaña, and M. Ardid, "Acoustic signal detection through the cross-correlation method in experiments with different signal to noise ratio and reverberation conditions," in *International conference on Ad-Hoc Networks and wireless*, Springer, 2014, pp. 66–79.

[101] L. Fillinger, A. Sutin, and A. Sedunov, "Acoustic ship signature measurements by cross-correlation method," *The Journal of the Acoustical Society of America*, vol. 129, no. 2, pp. 774–778, 2010.

[102] T. Olofsson and T. Stepinski, "Minimum entropy deconvolution of pulse-echo signals acquired from attenuative layered media," *The Journal of the Acoustical Society of America*, vol. 109, no. 6, pp. 2831–2839, 2001.

[103] M. Zhai, A. Locquet, and D. S. Citrin, "Pulsed THz imaging for thickness characterization of plastic sheets," *NDT & E International*, vol. 116, p. 102 338, 2020.

[104] A. Beck and M. Teboulle, "A fast iterative shrinkage-thresholding algorithm for linear inverse problems," *SIAM Journal on Imaging Sciences*, vol. 2, no. 1, pp. 183–202, 2009.

[105] I. Daubechies, M. Defrise, and C. De Mol, "An iterative thresholding algorithm for linear inverse problems with a sparsity constraint," *Communications on Pure and Applied Mathematics: A Journal Issued by the Courant Institute of Mathematical Sciences*, vol. 57, no. 11, pp. 1413–1457, 2004.

[106] J. M. Bioucas-Dias and M. A. Figueiredo, "Two-step algorithms for linear inverse problems with non-quadratic regularization," in *2007 IEEE International Conference on Image Processing*, IEEE, vol. 1, 2007, pp. I–105.

[107] X. Huang, K. He, S. Yoo, O. Cossairt, A. Katsaggelos, N. Ferrier, and M. Hereld, "An interior point method for nonnegative sparse signal reconstruction," in *2018 25th IEEE International Conference on Image Processing (ICIP)*, IEEE, 2018, pp. 1193–1197.

[108] K. Koh, S.-J. Kim, and S. Boyd, "An interior-point method for large-scale l_1-regularized logistic regression," *Journal of Machine Learning Research*, vol. 8, no. Jul, pp. 1519–1555, 2007.

[109] M. S. Islam, C. M. Cordeiro, M. J. Nine, J. Sultana, A. L. Cruz, A. Dinovitser, B. W.-H. Ng, H. Ebendorff-Heidepriem, D. Losic, and D. Abbott, "Experimental study on glass and polymers: Determining the optimal material for potential use in terahertz technology," *IEEE Access*, vol. 8, pp. 97 204–97 214, 2020.

[110] Y. Chang, Y. Zi, J. Zhao, Z. Yang, W. He, and H. Sun, "An adaptive sparse deconvolution method for distinguishing the overlapping echoes of ultrasonic guided waves for pipeline crack inspection," *Measurement Science and Technology*, vol. 28, no. 3, p. 035 002, 2017.

[111] N. Palka, M. Szala, and E. Czerwinska, "Characterization of prospective explosive materials using terahertz time-domain spectroscopy," *Applied Optics*, vol. 55, no. 17, pp. 4575–4583, 2016.

[112] R. E. Popil, *Physical testing of paper*. Smithers Pira, 2017.

[113] P. Mousavi, F. Haran, D. Jez, F. Santosa, and J. S. Dodge, "Simultaneous composition and thickness measurement of paper using terahertz time-domain spectroscopy," *Applied Optics*, vol. 48, no. 33, pp. 6541–6546, 2009.

[114] B. Scherger, M. Scheller, N. Vieweg, S. Cundiff, and M. Koch, "Paper terahertz wave plates," *Optics Express*, vol. 19, no. 25, pp. 24 884–24 889, 2011.

[115] T. Hattori, H. Kumon, and H. Tamazumi, "Terahertz spectroscopic characterization of paper," in *35th International Conference on Infrared, Millimeter, and Terahertz Waves*, IEEE, 2010, pp. 1–2.

[116] U. Strom, J. Hendrickson, R. Wagner, and P. Taylor, "Disorder-induced far infrared absorption in amorphous materials," *Solid State Communications*, vol. 15, no. 11-12, pp. 1871–1875, 1974.

[117] U. Strom and P. Taylor, "Temperature and frequency dependences of the far-infrared and microwave optical absorption in amorphous materials," *Physical Review B*, vol. 16, no. 12, p. 5512, 1977.

[118] J. Calvo-de la Rosa, A. Locquet, D. Bouscaud, S. Berveiller, and D. Citrin, "Optical constants of CuO and ZnO particles in the terahertz frequency range," *Ceramics International*, vol. 46, no. 15, pp. 24 110–24 119, 1920.

[119] J. Calvo-de la Rosa, A. Locquet, D. Bouscaud, S. Berveiller, and D. Citrin, "Terahertz permittivity of pressed ZnO and CuO powder in polyethylene pellets: Effect of porosity," *IEEE Transactions on Terahertz Science and Technology*, 2021.

[120] M. Jung, S.-i. Mho, and H. L. Park, "Long-range-ordered CdTe/GaAs nanodot arrays grown as replicas of nanoporous alumina masks," *Applied Physics Letters*, vol. 88, no. 13, p. 133 121, 2006.

[121] M. Zhai, A Locquet, M. Jung, D. Woo, and D. Citrin, "Characterization of nanoporous Al_2O_3 films at terahertz frequencies," *Optics Letters*, vol. 45, no. 14, pp. 4092–4095, 2020.

[122] M. S. Ilango, A. Mutalikdesai, and S. K. Ramasesha, "Anodization of aluminium using a fast two-step process," *Journal of Chemical Sciences*, vol. 128, no. 1, pp. 153–158, 2016.

[123] Y. Y. Zhu, G. Q. Ding, J. N. Ding, and N. Y. Yuan, "AFM, SEM and TEM studies on porous anodic alumina," *Nanoscale Research Letters*, vol. 5, no. 4, pp. 725–734, 2010.

[124] Y. Kondo, M. Numada, H. Koshimizu, K. Kamiya, and I. Yoshida, "Low-pass filter without the end effect for estimating transmission characteristics—simultaneous attaining of the end effect problem and guarantee of the transmission characteristics," *Precision Engineering*, vol. 48, pp. 243–253, 2017.

[125] ISO, "Geometrical product specifications (GPS)-filtration part 22: Linear profile filters: Spline filter," 2006.

[126] J. M. Runge, "The metallurgy of anodizing aluminum," *Cham: Springer International Publishing*, 2018.

[127] M. Bara, M. Niedźwiedź, and W. Skoneczny, "Influence of anodizing parameters on surface morphology and surface-free energy of Al_2O_3 layers produced on EN AW-5251 alloy," *Materials*, vol. 12, no. 5, p. 695, 2019.

[128] S.-Z. Chu, K. Wada, S. Inoue, M. Isogai, and A. Yasumori, "Fabrication of ideally ordered nanoporous alumina films and integrated alumina nanotubule arrays by high-field anodization," *Advanced Materials*, vol. 17, no. 17, pp. 2115–2119, 2005.

[129] N. Laman and D Grischkowsky, "Terahertz conductivity of thin metal films," *Applied Physics Letters*, vol. 93, no. 5, p. 051 105, 2008.

[130] H. Masuda and K. Fukuda, "Ordered metal nanohole arrays made by a two-step replication of honeycomb structures of anodic alumina," *Science*, vol. 268, no. 5216, pp. 1466–1468, 1995.

[131] D. P. Edward and I. Palik, *Handbook of optical constants of solids*, 1985.

[132] K. Z. Rajab, M. Naftaly, E. H. Linfield, J. C. Nino, D. Arenas, D. Tanner, R. Mittra, and M. Lanagan, "Broadband dielectric characterization of aluminum oxide (Al_2O_3)," *Journal of Microelectronics and Electronic Packaging*, vol. 5, no. 1, pp. 2–7, 2008.

[133] A. Hierro-Rodriguez, P Rocha-Rodrigues, F. Valdés-Bango, J. Alameda, P. Jorge, J. L. Santos, J. Araujo, J. Teixeira, and A. Guerreiro, "On the anodic aluminium oxide refractive index of nanoporous templates," *Journal of Physics D: Applied Physics*, vol. 48, no. 45, p. 455 105, 2015.

[134] S. Fellahi, A. Meddad, B. Fisa, and B. Favis, "Weldlines in injection-molded parts: A review," *Advances in Polymer Technology: Journal of the Polymer Processing Institute*, vol. 14, no. 3, pp. 169–195, 1995.

[135] S.-G. Kim and N. P. Suh, "Performance prediction of weldline structure in amorphous polymers," *Polymer Engineering & Science*, vol. 26, no. 17, pp. 1200–1207, 1986.

[136] H. Zhou and D. Li, "Modelling and prediction of weld line location and properties based on injection moulding simulation," *International Journal of Materials and Product Technology*, vol. 21, no. 6, pp. 526–538, 2004.

[137] K. Tomari, S. Tonogai, T. Harada, H. Hamada, K. Lee, T. Morii, and Z. Maekawa, "The V-notch at weld lines in polystyrene injection moldings," *Polymer Engineering & Science*, vol. 30, no. 15, pp. 931–936, 1990.

[138] C.-S. Chen, T.-J. Chen, R.-D. Chien, and S.-C. Chen, "Investigation on the weldline strength of thin-wall injection molded ABS parts," *International Communications in Heat and Mass Transfer*, vol. 34, no. 4, pp. 448–455, 2007.

[139] V. Ciubotariu and G. Brabie, "Weld line behaviour during uniaxial tensile testing of tailor welded blanks," *Archives of Civil and Mechanical Engineering*, vol. 11, no. 4, pp. 811–824, 2011.

[140] Y. C. Kagitci and N. Tarakcioglu, "The effect of weld line on tensile strength in a polymer composite part," *The International Journal of Advanced Manufacturing Technology*, vol. 85, no. 5, pp. 1125–1135, 2016.

[141] C.-H. Wu and W.-J. Liang, "Effects of geometry and injection-molding parameters on weld-line strength," *Polymer Engineering & Science*, vol. 45, no. 7, pp. 1021–1030, 2005.

[142] Y. Wang, Y. Sun, P. Lv, and H. Wang, "Detection of line weld defects based on multiple thresholds and support vector machine," *NDT & E International*, vol. 41, no. 7, pp. 517–524, 2008.

[143] M. B. Baradi, C. Cruz, T. Riedel, and G. Régnier, "Mechanical and microstructural characterization of flowing weld lines in injection-molded short fiber-reinforced PBT," *Polymer Testing*, vol. 74, pp. 152–162, 2019.

[144] G. Tosello, A. Gava, H. N. Hansen, G. Lucchetta, and F. Marinello, "Characterization and analysis of weld lines on micro-injection moulded parts using atomic force microscopy (AFM)," *Wear*, vol. 266, no. 5-6, pp. 534–538, 2009.

[145] R. Selden, "Effect of processing on weld line strength in five thermoplastics," *Polymer Engineering & Science*, vol. 37, no. 1, pp. 205–218, 1997.

[146] D. A. Grewell, A. Benatar, and J. B. Park, "Plastics and composites welding handbook," *München*, vol. 10, 2003.

[147] Z. Tadmor, "Molecular orientation in injection molding," *Journal of Applied Polymer Science*, vol. 18, no. 6, pp. 1753–1772, 1974.

[148] H. Mavridis, A. Hrymak, and J. Vlachopoulos, "Transient free-surface flows in injection mold filling," *AIChE Journal*, vol. 34, no. 3, pp. 403–410, 1988.

[149] T. Nguyen-Chung, C. Plichta, and G. Mennig, "Flow disturbance in polymer melt behind an obstacle," *Rheologica Acta*, vol. 37, no. 3, pp. 299–305, 1998.

[150] A. Isayev, G. Shyu, and C. Li, "Residual stresses and birefringence in injection molding of amorphous polymers: Simulation and comparison with experiment," *Journal of Polymer Science Part B: Polymer Physics*, vol. 44, no. 3, pp. 622–639, 2006.

[151] S. C. Chen, Y. C. Chen, N. Cheng, and M.-S. Huang, "Simulation of injection-compression mold-filling process," *International Communications in Heat and Mass Transfer*, vol. 25, no. 7, pp. 907–917, 1998.

[152] J. Han, C. Shen, C. Liu, S. Wang, and J. Chen, "Flow induced birefringence of weldline region in polystyrene injection molding," *Journal of Chemical Industry and Engineering(China)*, vol. 59, no. 5, p. 1305, 2008.

[153] Y. Wang, Q. Miao, Y. Guo, and C. Niu, "Research on flow behavior of flat products weld line area amorphous polymer," *New Technology & New Process*, 2012.

[154] S. Piccarolo and M. Siau, "Knit-line structure in the injection molding of polystyrene," *Plastics and Rubber Processing and Applications*, vol. 10, no. 1, pp. 11–16, 1988.

[155] S. C. Malguarnera, "Weld lines in polymer processing," *Polymer-Plastics Technology and Engineering*, vol. 18, no. 1, pp. 1–45, 1982.

[156] T. Nguyen-Chung, "Flow analysis of the weld line formation during injection mold filling of thermoplastics," *Rheologica Acta*, vol. 43, no. 3, pp. 240–245, 2004.

[157] R. Wimberger-Friedl, "The assessment of orientation, stress and density distributions in injection-molded amorphous polymers by optical techniques," *Progress in Polymer Science*, vol. 20, no. 3, pp. 369–401, 1995.

[158] M. Mitsuhashi, K. Nishimura, T. Yamamoto, N. Mori, and K. Nakamura, "Welding flow of low density polyethylene melt," *Journal of Textile Engineering*, vol. 49, no. 1, pp. 14–22, 2003.

[159] E. T. A. Mohamed, M. Zhai, G. Schneider, R. Kalmar, M. Fendler, A. Locquet, D. Citrin, and N. Declercq, "Scanning acoustic microscopy investigation of weld lines in injection-molded parts manufactured from industrial thermoplastic polymer," *Micron*, vol. 138, p. 102 925, 2020.

[160] Y. C. Chen, C.-H. Chen, and S. C. Chen, "Effects of processing conditions on birefringence development in injection molded parts. II. experimental measurement," *Polymer International*, vol. 40, no. 4, pp. 251–259, 1996.

[161] Z. Yu and S. Boseck, "Scanning acoustic microscopy and its applications to material characterization," *Reviews of Modern Physics*, vol. 67, no. 4, p. 863, 1995.

[162] R. J. da Fonseca, L. Ferdj-Allah, G. Despaux, A. Boudour, L. Robert, and J. Attal, "Scanning acoustic microscopy—recent applications in materials science," *Advanced Materials*, vol. 5, no. 7-8, pp. 508–519, 1993.

[163] G.-M. Zhang, D. M. Harvey, and D. R. Braden, "Microelectronic package characterisation using scanning acoustic microscopy," *NDT & E International*, vol. 40, no. 8, pp. 609–617, 2007.

[164] L. P. Bauermann, L. Mesquita, C Bischoff, M Drews, O Fitz, A Heuer, and D Biro, "Scanning acoustic microscopy as a non-destructive imaging tool to localize defects inside battery cells," *Journal of Power Sources Advances*, vol. 6, p. 100 035, 2020.

[165] R. Lemons and C. Quate, "Acoustic microscope—scanning version," *Applied Physics Letters*, vol. 24, no. 4, pp. 163–165, 1974.

[166] M. G. Somekh, G. Briggss, and C. Ilett, "The effect of elastic anisotropy on contrast in the scanning acoustic microscope," *Philosophical Magazine A*, vol. 49, no. 2, pp. 179–204, 1984.

[167] M. Ma, Y. Wang, M. Navarro-Cia, F. Liu, F. Zhang, Z. Liu, Y. Li, S. M. Hanham, and Z. Hao, "The dielectric properties of some ceramic substrate materials at terahertz frequencies," *Journal of the European Ceramic Society*, vol. 39, no. 14, pp. 4424–4428, 2019.

[168] F. Sanjuan and J. Tocho, "Optical properties of silicon, sapphire, silica and glass in the terahertz range," in *Latin America Optics and Photonics Conference, OSA Technical Digest (Optical Society of America, 2012), paper LT4C.1*, 2012.

[169] S. Chen, K. N. Nguyen, and M. N. Afsar, "Complex dielectric permittivity measurements of glasses at millimeter waves and terahertz frequencies," in *2006 European Microwave Conference*, IEEE, 2006, pp. 384–387.

[170] R. Gharpurey and R. G. Meyer, "Modeling and analysis of substrate coupling in integrated circuits," *IEEE Journal of Solid-State Circuits*, vol. 31, no. 3, pp. 344–353, 1996.

[171] G. Pastorelli, T. Trafela, P. Taday, A. Portieri, L. D., K. Fukunaga, and M. Strlic, "Characterisation of historic plastics using terahertz time-domain spectroscopy and pulsed imaging," *Analytical and Bioanalytical Chemistry*, vol. 403, pp. 1405–1414, 2012.

[172] F. D'Angelo, Z. Mics, M. Bonn, and D. Turchinovich, "Ultra-broadband THz time-domain spectroscopy of common polymers using THz air photonics," *Optics Express*, vol. 22, no. 10, pp. 12 475–12 485, 2014.

[173] A. Podzorov and G. Gallot, "Low-loss polymers for terahertz applications," *Applied Optics*, vol. 47, no. 18, pp. 3254–3257, 2008.

[174] M. Naftaly, R. Miles, and P. Greenslade, "THz transmission in polymer materials–a data library," in *2007 Joint 32nd International Conference on Infrared and Millimeter Waves and the 15th International Conference on Terahertz Electronics*, IEEE, 2007, pp. 819–820.

[175] J. Tong, Y. Sato, S. Takahashi, N. Imajyo, A. F. Peterson, V. Sundaram, and R. Tummala, "High-frequency characterization of through package vias formed by focused electrical-discharge in thin glass interposers," in *2014 IEEE 64th Electronic Components and Technology Conference (ECTC)*, IEEE, 2014, pp. 2271–2276.

[176] W. T. Khan, J. Tong, S. Sitaraman, V. Sundaram, R. Tummala, and J. Papapolymerou, "Characterization of electrical properties of glass and transmission lines on thin glass up to 50 GHz," in *2015 IEEE 65th Electronic Components and Technology Conference (ECTC)*, IEEE, 2015, pp. 2138–2143.

[177] M. ur Rehman, S. Ravichandran, A. O. Watanabe, S. Erdogan, and M. Swaminathan, "Characterization of ABF/Glass/ABF substrates for mmWave applications," *IEEE Transactions on Components, Packaging and Manufacturing Technology*, vol. 11, no. 3, pp. 384–394, 2021.

[178] M. Naftaly, N. Ridler, J. Molloy, N. Shoaib, and D. Stokes, "A comparison method for THz measurements using VNA and TDS," in *2015 40th International Conference on Infrared, Millimeter, and Terahertz waves (IRMMW-THz)*, IEEE, 2015, pp. 1–2.

[179] M. Zhai, E. T. A. Mohamed, A. Locquet, G. Schneider, R. Kalmar, M Fendler, N. F. Declercq, and D. S. Citrin, "Diagnosis of injection-molded weld lines in ABS thermoplastic by polarized terahertz reflective imaging," *NDT & E International*, vol. 122, p. 102 497, 2021.

[180] X. Xin, H. Altan, A. Saint, D. Matten, and R. Alfano, "Terahertz absorption spectrum of para and ortho water vapors at different humidities at room temperature," *Journal of Applied Physics*, vol. 100, no. 9, p. 094 905, 2006.

[181] M. Naftaly and R. Miles, "Terahertz time-domain spectroscopy of silicate glasses and the relationship to material properties," *Journal of Applied Physics*, vol. 102, no. 4, p. 043 517, 2007.

[182] V. Bershtein and V. Ryzhov, "Far infrared spectroscopy of polymers," *Polymer Analysis and Characterization*, pp. 43–121, 1994.

[183] A. Jonscher, "The universal dielectric response and its physical significance," *IEEE Transactions on Electrical Insulation*, vol. 27, no. 3, pp. 407–423, 1992.

[184] S. Taraskin, S. Simdyankin, S. Elliott, J. Neilson, and T. Lo, "Universal features of terahertz absorption in disordered materials," *Physical Review Letters*, vol. 97, no. 5, p. 055 504, 2006.

[185] M. Zhai, A. Locquet, C. Roquelet, P. Alexandre, L. Daheron, and D. Citrin, "Non-destructive measurement of mill-scale thickness on steel by terahertz time-of-flight tomography," *Surface and Coatings Technology*, vol. 393, p. 125 765, 2020.